UNIVERSITA' DEGLI STUDI DI PARMA

DOTTORATO DI RICERCA IN

Scienza e Tecnologia dei Materiali

CICLO XXXVIII

Valorisation of ceramic materials from circular economy sources for high-value applications

Coordinatore:

Chiar.mo Prof. Davide Orsi, Ph.D.

Tutore:

Dott. Alessio Adamiano, Ph.D.

Dottoranda:

Sara Gandolfi

A.A.: 2022 – 2024

AIM OF THE WORK

Given the increasingly urgent need to implement the principles of the circular economy in industrial processes, this thesis aims to reuse by-products from the fishing industry as a source of natural raw materials. Notably, fish bones represent a by-product rich in valuable materials such as hydroxyapatite (HA) and collagen (Col), substances that are widely used in fields such as cosmetics, medicine, agri-food and many others. Usually synthesised in laboratories or derived from non-renewable raw materials, HA and Col can be obtained in a more environmentally and economically sustainable way. However, current extraction methods do not allow these two materials to be obtained simultaneously, as the extraction processes of one completely destroys the other.

The aim of this work was therefore to develop extraction methods that would allow for the simultaneous extraction of HA and Col from salmon bones, and to test HA uses in oral care, sun care and wastewater treatment.

In particular, HA has been studied as a remineralising agent for dental enamel, as a preventive agent for tooth sensitivity, and as a sun protection factor booster in sunscreen formulations. For wastewater treatment, HA has been studied as an adsorbent phase for dyes used in the textile industry.

Table of content

CHAPTER I: INTRODUCTION

1.1. Circular Economy

The circular economy (CE) is an economic model that contrasts with the linear economy. Specifically, it is a model of production and consumption that involves sharing, lending, reusing, repairing, reconditioning and recycling existing materials and products for as long as possible, to extend the life cycle of products, helping to minimise waste. Once a product is no longer usable, its materials are recycled and used to generate products with high added value. This model leads to many advantages, both environmentally and economically, as it reduces the use of natural resources, preserves territories and habitats, and helps limit biodiversity loss. Not to mention that it would reduce CO_2 emissions into the atmosphere, which are in part caused by the extraction and use of natural raw materials [1], [2], [3].

According to Eurostat, the EU imports approximately half of the raw materials it consumes. This led to a trade deficit of €35.5 billion in 2021. Recycling raw materials helps mitigate risks related to supply, availability, and import dependency. As the global population grows, the availability of essential raw materials and resources for the economy is becoming increasingly limited, leading to greater dependency on other countries [4].

The European Commission's programme [COM(2015)614] proposes that the extension of value chains for products and services can facilitate the creation of a sustainable economic system. This system would be beneficial not only to industries, but also and above all, to the environment and citizens. The various and multiple strategies proposed for the transition from a linear to a circular economy are mainly supported by industrial activities. These strategies are based on the waste hierarchy of the three Rs (“reduce-reuse-recycle”, as opposed to the linear economy based on the "take-make-dispose" sequence) [5], [6], such as the application of sustainable and ecological design, energy and material efficiency measures and innovative economic models [7].

1.2. Fish industry

The consumption of fish has increased dramatically over the years, leading to an increasing need for industries to implement waste control measures to reduce their environmental impact [7]. In least developed countries, fish is a crucial source of protein and micronutrients, playing a fundamental role in children's healthy development and contributing positively to the healthcare systems of these nations [8], [9]. Among many others, fishing industry represents a key economic source for several countries around the world. It is estimated that one billion people depend on the production, processing, and trade of fish as a source of income [10].

In 2022, global fisheries and aquaculture production reached an all-time record of 223.2 Mt. Over the decades, the apparent global consumption of food derived from aquatic animals has increased significantly, with an annual growth rate exceeding that of the world population. It grew by an average of 1.4% per year, from 9.1 kg in 1961 to 20.6 kg in 2021.

Trade in aquatic animal products in 2022 increased by 19% compared to 2019, accounting for more than 9.1% of total agricultural trade (excluding forest products) [11]. Figure 1 shows the average global fishing data between 2020 and 2022, reported in terms of tons of pelagic fish captured or farmed by each country.

Fish processing involves a large number of operations, including the removal of the head, descaling, washing, gutting, cutting the fins and separating the meat from the bones and fillets [12]. Each of these steps generates waste, and by generating such large amounts of products each year, the Fish Processing Industry (FPI) is also responsible for producing a huge amount of waste [10], [13], [14]. Notably, on average, only 40% of caught fish is used for human consumption, while the remaining 60% is discarded [15].

It is estimated that between 7 and 10 Mt of commercial fish are discarded globally each year, with variations from region to region [7], [16].

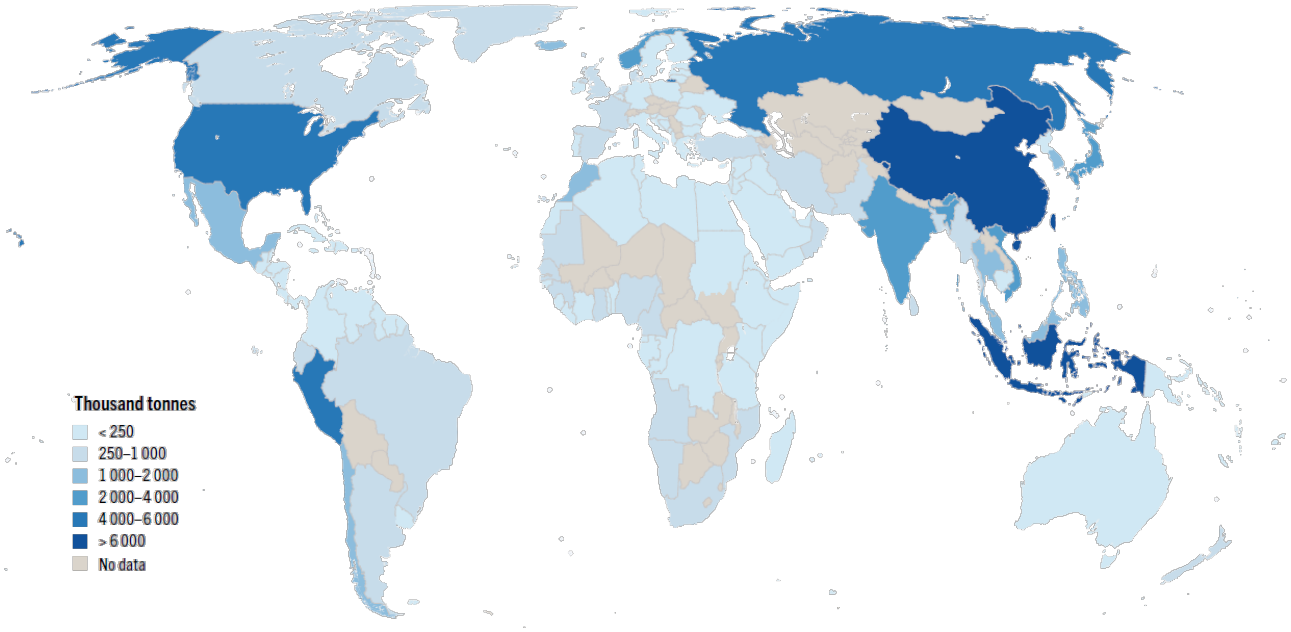

Figure 1. World fisheries production in marine areas in countries and territories, average 2020-2022 [11]

These large quantities of fish waste create significant economic problems for the industries that have to process/dispose of them, and environmental problems because vessels - especially pelagic fishing fleets operating far from shore - often process fish onboard and illegally discharge fish waste directly into the ocean, leading to localized pollution and disturbing nutrient cycles of marine ecosystems. From an economic and environmental standpoint, the disposal of this waste is regrettable, as it contains valuable substances, including proteins (such as collagen) and minerals, which could be utilized in many alternative ways [17].

The main inorganic component of these bones is hydroxyapatite, for which there are no ad-hoc extraction/valorisation processes, even though this material is successfully used for many high-end value applications, e.g. as material for the production of medical scaffolds and as remineralizing agent in toothpastes [18], [19]. On the contrary, this is typically considered an obstacle to the conventional valorisation of fish waste into products such as animal feed, plant fertilisers, fish oil and fishmeal [20]. However, the profitability of these products is relatively low.

High-quality products can also be obtained by processing the raw materials obtained from the waste into entirely new products with high added value. The extraction of these compounds appears to be economically promising due to their recognised positive impact on human health, with applications in biotech, food, pharmaceuticals, medicine, and cosmetics [13], [21].

Among the many fish species, salmon is the most consumed and therefore the most processed fish in the world. For this reason, this work was focused on developing green and innovative methods for the simultaneous extraction of collagen (Col) and hydroxyapatite (HA) from the bones of this species (chapter II), and to investigate their possible applications in cosmetics and wastewater treatment (chapters III, IV, V).

Finally, fish-derived materials don't have any religious or ethical implications that prevent their use by certain populations [16], therefore representing a viable alternative to HA and Col obtained from mammals (which are already used in a wide number of products) that a larger number of people can consume.

1.2.1. Fishbones

Fish bones represent a significant portion of FPI by-products. Traditionally used for animal meal production, they have been investigated in recent years as a source of high-quality protein and biogenic minerals, i.e., calcium phosphates (CaPs). CaPs are a very large family of minerals with different physical-chemical properties. Of these, HA is the most stable form under environmental conditions and is the main component of the mineral matrix of human and animal bones. Depending on the animal species, its age and the habitat in which it lived, the structure and composition of HA can change. In addition, several trace elements may be present, such as Al, Cl, Cu, F, Fe, Mg, K, Na, Si, Sr and Zn, which can strongly influence its properties [22]. Depending on the method and its parameters (e.g., calcination temperature), several minerals belonging to the CaPs family can be extracted from bones, including HA($Ca_{10}(PO_4)_6(OH)_2$, Ca/P=1.67), octacalcium phosphate (OCP, $Ca_8H_2(PO_4)\cdot 6.5H_2O$, Ca/P=1.33), β-tricalcium phosphate (β-TCP, β-$Ca_3(PO_4)_2$, Ca/P= 1.50), dicalcium phosphate dihydrous, brushite ($CaHPO_4\cdot 2H_2O$, Ca/P= 1.00, DCPD), α-tricalcium phosphate (α-TCP, α-$Ca_3(PO_4)_2$), Ca/P= 1.50), tetracalcium phosphate (TTCP, CaO·Cay $(PO_4)_2$, Ca/P= 2.0), amorphous calcium phosphate (ACP, Ca/P= 1.25–1.55), ecc [23], [24]. Figure 2 shows the main parameters influencing the properties of CaPs and the most common crystalline phases derived from them.

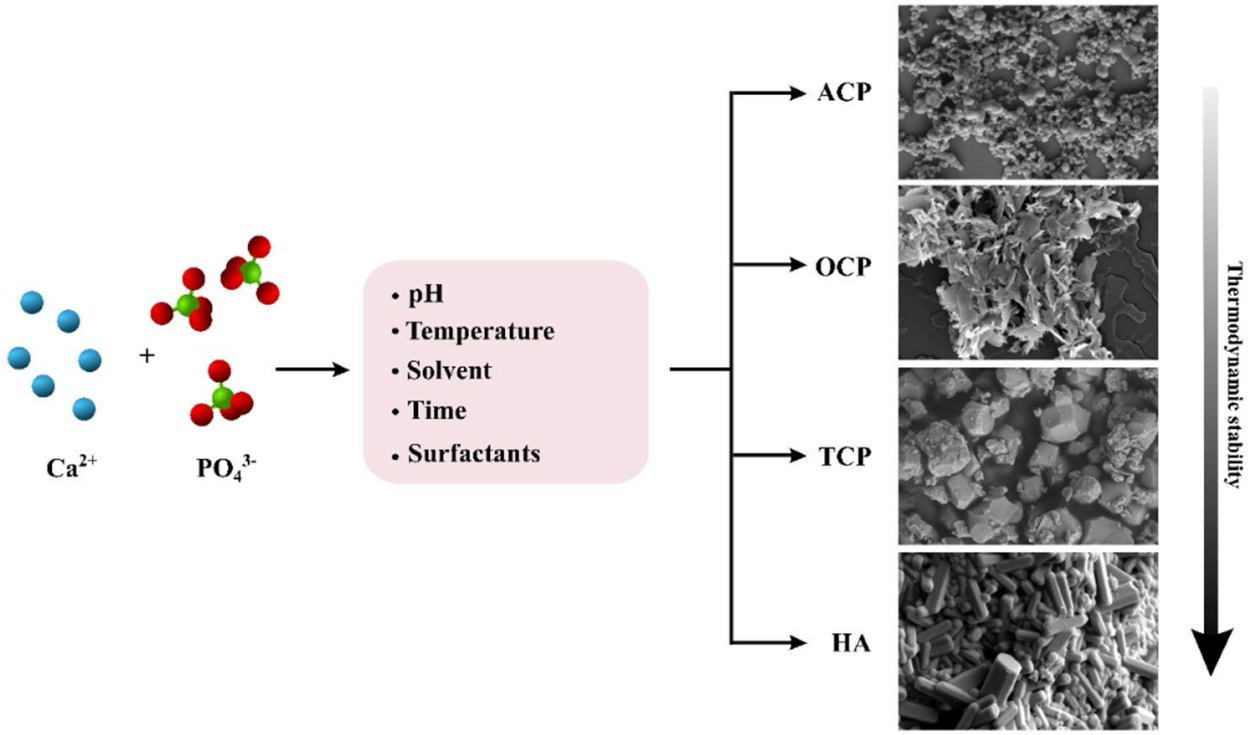

Figure 2. Principal synthesis parameters that influence the calcium phosphates characteristics and the formation of different crystalline phases [24]

While Col is present in greater quantities in other fish areas, such as the skin, it remains a significant component of the bones, varying between 20-70% [25] of the total protein content [10], [26]. Small amounts of non-collagenous proteins, which play a role in mineralisation and bone repair, can also be found, but they typically represent a small fraction of the total bone matrix, usually less than 10% of the protein content.

1.2.1.1. Collagen

"Collagen" is a generic term used to describe a family of 28 genetically distinct proteins. It accounts for approximately 30% of all proteins in mammals and is the major protein component of connective tissues in the extracellular matrix, which is essential for the structural and mechanical stability of tissues [7], [27]. It's not present in the tissues of the other major groups of the plant and fungal kingdoms, but proteins with a similar molecular structure have been identified in some bacteria [27].

It consists of three polypeptide chains, wound together to form the Col molecule in a triple helix, giving the typical "three-chain, triple-helix structure" as depicted in Figure 3.

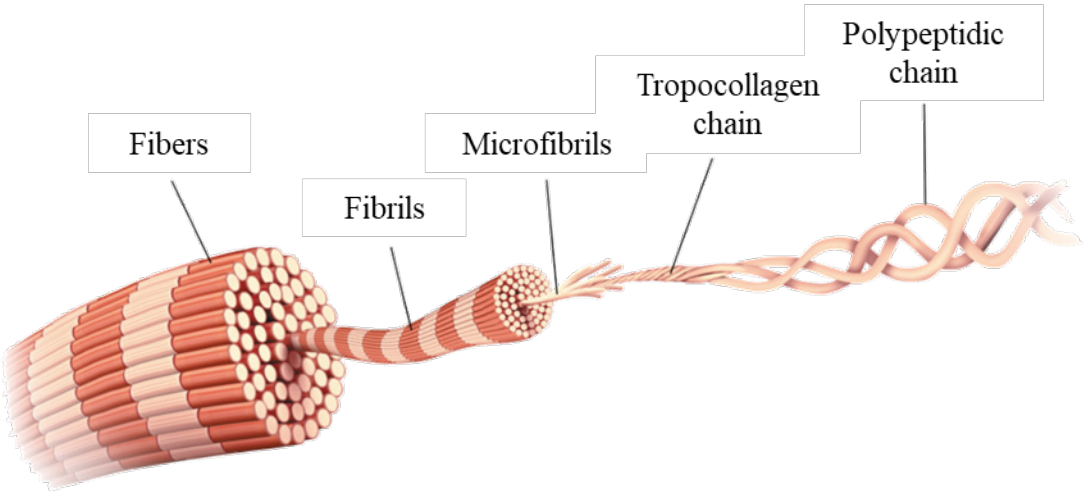

Figure 3. Collagen hierarchical structure

Glycine (Gly) is the only amino acid small enough to fit into the centre of the structure, giving it the characteristic (Gly-X-Y)n sequence. The X and Y positions can be occupied by several amino acids, but in most cases proline (Pro) is found [7], [28]. The amino acids occupying the Y positions generally undergo a secondary modification reaction catalysed by the enzyme prolyl-4-hydroxylase, which generates 4-hydroxyproline (Hyp) residues [26]. Hydroxyproline (Hyp) is the amino acid that stabilises the triple-helical structure of Col. As it is exclusively present in Col, its quantity is directly proportional to the amount of Col. Its formation is linked to the

environmental temperature in which a species lives: in marine species, which typically live at ambient temperatures below 37°C, the Hyp content is lower than in warm-blooded animals [7], [30].

The extension of the triple helix and the presence of non-triple helix regions allow Col to be subdivided into different types. The types and their contribution to the extracellular matrix that constitutes the vertebrate body are shown in Figure 4 [31].

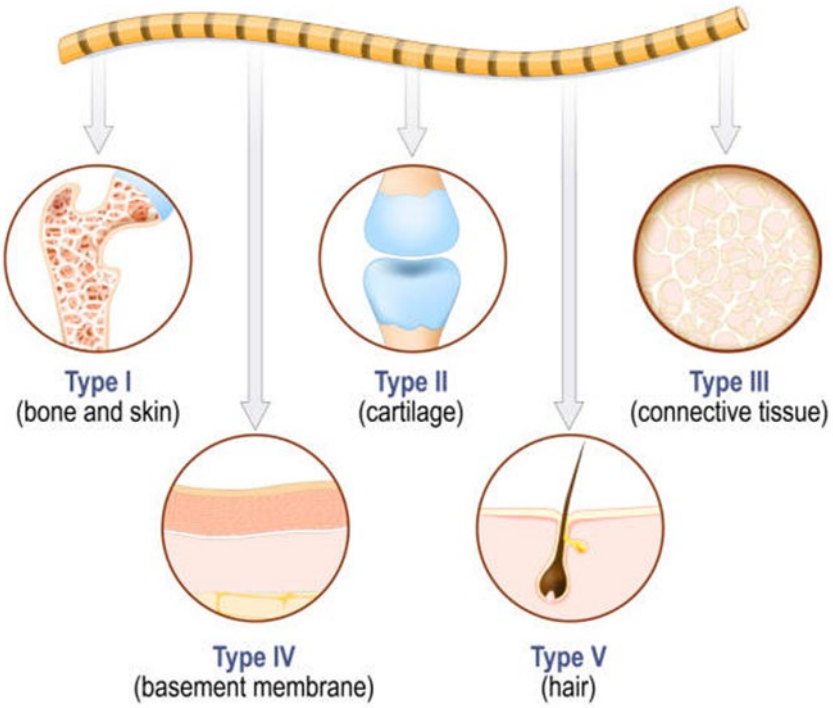

Figure 4. Col types and their presence in the human body

Type I Col is the most abundant form of collagen in mammals, accounting for between 80 and 90% of total Col. It's the main component of tissues, skin, tendons, ligaments, and bones. In native tissues it is present in fibrils, in which the molecules are arranged in a staggered and overlapping three-dimensional structure [32], a functional component of fibrils and thus of tissues. In bones, the type I Col fibrils also function as a site for mineralization, either directly or through association with mineralisation nucleation proteins [33], [34]. It's therefore essential for vital physiological processes, including haemostasis, angiogenesis and biomineralisation [34], [35]. This is why type

I Col derived from animal sources is the most widely used biomaterial to produce scaffolds for bone regeneration, haemostatics, bandages and tendon repair patches [31]. Purified type I Col, in solution, is also capable of self-assembling into fibrils, which can be used to form hydrogels, useful in clinical field for tissue augmentation and have more recently become popular in tissue engineering and regenerative medicine strategies for patterning and cell delivery [36], [37].

Col is considered one of the most valuable biomaterials, as it plays an active role in numerous industrial processes [38]. Its ability to absorb water, form gels and stabilise emulsions make it a very useful material in the food industry. It has antimicrobial, antioxidant and antihypertensive properties, which is why it is used in the biomedical and pharmaceutical fields as a vehicle for drugs, proteins and genes, as well as a substitute for blood vessels, ligaments and skin [39], [40]. The demand for Col products continues to grow, but the availability of raw material remains limited. The reuse of collagen-containing waste is therefore an interesting alternative to meet the demand [7]. Recovered Col can be used to create new products, such as bioplastics for packaging [41], or it can be fragmented to obtain Col peptides [42], which are widely used for food, cosmetic and pharmaceutical applications [43], [44], [45]. It is highly likely that marine-derived Col will significantly contribute to a market typically dominated by materials of mammalian origin [39], [46].

1.2.1.2. Hydroxyapatite

HA belongs to the large family of CaPs. These minerals constitute the inorganic component of vertebrate hard tissues (e.g. bones and teeth) but are also found in fish scales or in milk and blood as the primary source of calcium [47], [48]. Of all the other CaPs phases, HA is the most used because it is the most thermodynamically stable under physiological conditions.

In its stoichiometric form [$Ca_{10}(PO_4)_6(OH)_2$], HA has a crystallographic symmetry of the group $P6_3/m$ and is constituted by a compact set of phosphate tetrahedra (PO_4^{3-}) held together by Ca^{2+} ions intercalated between them. The structure thus presents alternating equilateral triangles staggered along the c-axis (Figure 5), whose large size allows the OH^- anion to move along it [49], [50]. Overall, the structure presents itself as a hexagonal crystal system with two planes: *a* plane, composed mainly of positively charged Ca^{2+} ions, and the *c* plane, composed mainly of negatively charged PO_4^{3-} ions. This dual polarity gives the HA surfaces anisotropic properties [51].

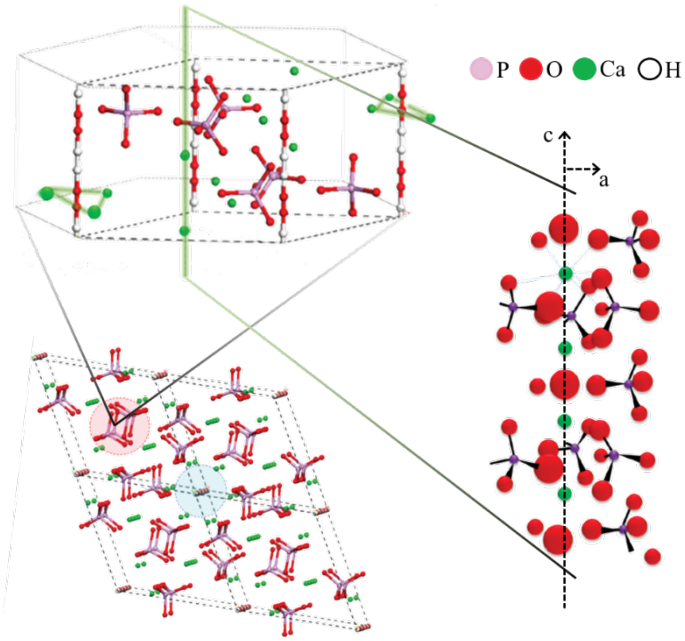

Figure 5. HA hexagonal cell structure

The Ca^{2+}, PO_4^{3-} or OH^- ions can be replaced by other ions without introducing changes in the crystal structure of the HA [52], [53], [54], [55]. Conversely, the material properties vary, allowing the production of doped HA with the same crystallinity, chemical composition, ion doping, size and morphology as biogenic minerals, but with different characteristics depending on the intended use (e.g., HA-F in dental field, to reduce and prevent enamel demineralization and caries, HA-Sr and HA-Mg in the medical field, as promoters of bone formation) [56], [57]. In such instances, the term "stoichiometric hydroxyapatite" is no longer applicable, and the material in question is instead referred to as "biomimetic hydroxyapatite" (Ca/P ratio different from 1.67) [47], [55], [58].

Usually, HA is chemically synthesised from raw materials obtained from non-renewable mineral deposit, e.g., H_3PO_4 from phosphate rocks. This poses environmental and economic/political problems as most phosphorite deposits are concentrated in few countries like Morocco and China having the 85% and the 6% of global reserves, respectively. HA for cosmetic and medical applications is chemically synthesised to be similar to natural HA found in bones, i.e. to be biomimetic. However, it has been reported that HA extracted from animal bones by various methods can replace synthetic HA, e.g. for the preparation of medical scaffolds, without any drawbacks [59], [60]. Both biomimetic and natural HAs contain significant amounts of foreign ions (such as Mg, F, CO_3, Na and K) and are deficient in Ca^{2+} and OH^-. These differences are responsible for their relatively high solubility and specific biological activity compared to stoichiometric HA [52], [61]. Furthermore, the presence of foreign ions destabilises the crystal lattice of HA by accelerating its degradation and facilitating the release of these ions, which can then perform specific functions [62]. For instance, magnesium plays a significant role in bone metabolism, influencing bone growth and preventing potential risk factors for osteoporosis in humans [63], while fluoride reduce and prevent enamel demineralization and caries [57], [64].

1.2.2. Standard extraction methods of Col and HA from fishbones

Typical extraction methods for fishbones aim to recover either Col or HA, with each process focusing on one component while the other is discarded. In methods designed for Col recovery, the fishbone is first subjected to demineralization using acid solutions, which removes the HA and leaves behind the organic matrix. Col is then extracted through hydrolysis, which breaks down the proteins, allowing for its isolation.

The *extraction of Col* from bones is a complicated process that can be done by chemical or enzymatic hydrolysis. Col is present in cross-linked form in the connective tissue of animals, so acidic or basic pretreatment is required to remove non-collagenous substances. Subsequently, the raw material is subjected to partial hydrolysis by diluted acids and alkali, which enables the skin to expand to a volume that is two to three times its original size. This process facilitates the hydrolysis of cross-links while preserving the integrity of Col chains [65].

With the *chemical hydrolysis* it's possible to obtain a portion of Col, depending on the substances that are used. Salt Soluble Col (SSC) is obtained by using neutral saline solutions such as sodium chloride (NaCl), Tris-HCl [Tris (hydroxymethyl) aminomethane hydrochloride], phosphates or citrates.

To obtain Acid Soluble Col (ASC), the raw material is treated with acid, as citric acid, lactic acid or hydrochloric acid at low temperature (~ 4°C), to minimise the degradation of Col [65]. After separation from the pellet, Col contained in the supernatant is obtained by precipitation with NaCl and subsequent dialysis [66].

Enzymatic hydrolysis permits to obtain the second portion of Col, the Enzyme Soluble Col (ESC). The raw material, which may be the residue of chemical hydrolysis, is added to an acetic acid solution containing enzymes such as pepsin, papain or trypsin. At the end of each process, Col is obtained by precipitation with NaCl and subsequent dialysis [66].

Chemical hydrolysis is more widely used in industry, but enzymatic extraction, although more expensive, offers many advantages. In fact, the process can be conducted using mild extraction conditions, it's highly specific, the degree of hydrolysis can be precisely controlled, can reduce processing time and produces fewer by-products. The structure, composition and resulting properties of Col are dependent upon the extraction conditions and, potentially, the specificity of the enzyme employed [39].

On the other hand, when the goal is to *recover HA*, the fishbone is treated to preserve the mineral phase, while Col is degraded and removed often through calcination. Before the extraction, the bones are pre-cleaned, including boiling and chemical washing (with acetone, alcohol, chloroform, hydrogen peroxide, salt or alkaline solution) to degrease, remove proteins and soften the bones [67], [68]. Alternatively, bones may be chemically treated with acidic, alkaline or acid-alkaline solutions (usually with NaOH, KOH) [69]. Subsequent extraction of HA can be carried out by several processes, including alkaline hydrolysis, enzymatic hydrolysis, heat treatment, calcination, hydrothermal treatment or the use of subcritical water or ionic liquids [16], [70]. Of the various possible routes, calcination at high temperatures (usually between 600-950°C) is the one that produces a material with higher crystallinity, while subcritical hydrolysis and alkaline hydrothermal techniques, for example, yield products with lower crystallinity and a different morphology, such as nanoflakes and nanorods [16]. Furthermore, high temperatures facilitate the destruction of any pathogen that may be present, a risk associated with the biogenic nature of the raw material [49].

1.3. Cosmetic applications

In recent years, there has been a growing trend towards the use of natural materials in cosmetics as an alternative to synthetic substances that can pose a risk to human health [24]. As defined by the US Food and Drug Administration (FDA), cosmetics are substances that cleanse, beautify and promote the attractiveness of the body, without altering its appearance and without interfering with the physiology or functions of the body [71]. This definition specifically applies to any substance that is placed in contact with an external part of the body, or with the teeth and mucous membranes of the oral cavity, for the purpose of protecting, perfuming, cleaning or modifying its appearance [72], [73].

It is important to specify the difference between "make-up", which is purely related to the beautification of the skin, and "skin care", which includes all those treatments aimed at improving the skin from a health point of view.

Among the many substances found in cosmetics, some are potentially hazardous, even in small quantities, such as heavy metals. Their presence has been linked to the occurrence of various health problems, including allergic reactions, cardiovascular diseases, fertility problems and even cancer [74]. European Regulation No. 1223/2009/EC does not establish definitive limits on the amount of metals tolerated in a cosmetic product, allowing for their presence in trace amounts when technically unavoidable. Furthermore, cosmetic products are required to meet exceptionally high standards of purity and microbiological stability. To achieve this, preservatives such as parabens, which are biodegradable substances that do not change the texture or colour of products, are commonly employed. However, prolonged use of products containing parabens can be harmful to the human body, although these substances are considered safe by the FDA and the European Chemicals Agency (ECHA) [73], [75], [76].

It’s therefore necessary to find alternatives in cosmetic applications that are highly biocompatible, biodegradable and non-toxic. HA and Col from bones meet all these requirements, representing a viable alternative to polluting and hazardous substances.

1.3.1. Sun care

Sunlight can have several effects on human skin. It can cause redness, irritation, premature wrinkling and, in the long term, the development of skin cancer [77]. Fortunately, sunscreens provide adequate protection from ultraviolet (UV) radiation [78], as they contain UV filters that shield solar radiation in different ways. Paradoxically, some of these chemicals can be very harmful to both the environment and human health [79]. Once in the marine environment, these compounds can damage fragile and valuable ecosystems such as coral reefs, leading to a loss of biodiversity, and can bioaccumulate thought the trophic chain up to fish species largely consumed as foods, endangering human health [80]. In addition, once applied to the skin, UV filters can penetrate the human body through the bloodstream and cause photo-allergies, skin irritations and phototoxic reactions that can generate reactive oxygen species (ROS) [81].

To match the need to replace or at least reduce the concentration of these UV filters in sunscreens, various materials, including those of natural origin, have been tested. Waxes, for example, are commonly used in sunscreens to facilitate their application. By creating an even film on the skin, they provide increased protection, which is reflected in an increase in the sun protection factor (SPF) [82]. Ingredients of marine origin, such as alkenes [80], are also becoming popular in cosmetics as they are rich in vitamins, minerals, proteins and essential fatty acids [84], [85], [86].

The objective of this study was to investigate the potential of natural HA derived from salmon bones as an SPF booster for sunscreens containing both organic and inorganic filters, to obtain formulations that provide the same level of protection but contain a reduced amount of UV-filters.

1.3.2. Oral care

The consumption of specific substances, including sugars, acidic foods and beverages, as well as the presence of certain diseases such as gastro-oesophageal reflux and the fermentative activity of dental biofilms, can lead to the development of various disorders, such as the formation of caries [87], [88]. This is due to the fact that HA, the main component of dental enamel, is soluble in acidic conditions, having a critical pH of 5.5. When the oral microenvironment reaches pH values below the critical pH, the demineralisation process is initiated, due to the progressive loss of ions from the hard tissue, resulting in the dissolution of the tissue itself [89], [90], [91].

Under physiological conditions, the basic ions present in saliva neutralise demineralisation, maintaining a delicate balance between demineralisation and remineralisation [92]. When the action of saliva is insufficient, an external supply of calcium and phosphate ions is required to restore the pH balance of the oral cavity [93]. These ions precipitate and coat tooth surfaces with an amorphous mineral layer, stimulating the spontaneous remineralisation of damaged enamel HA prisms and leading to the restoration of mineral structure [94], [95]. Several studies have shown that synthetic HA and other calcium phosphate materials, such as amorphous calcium phosphate (ACP), especially in the form of nanoparticles, can promote remineralisation processes [19], [96]. The biphasic material composed of HA and β-TCP, such as that obtained from salmon bones extractions, is also widely used as a material for bone grafts and as a coating for dental implants due to its close chemical and crystallographic similarity to the inorganic constituents of bone and teeth [97], [98], [99].

1.3.3. Wastewater treatment

Water is an indispensable element for life on Earth. However, it is also extensively used in numerous industrial processes. The textile industry is one of the most water-intensive human activities, with significant environmental impacts. It uses an enormous amount of potable water in various stages of its production chain, so much so that the discharge of untreated water accounts for 80% of the total emissions of this type of industry. The wastewaters produced during various production stages, including washing, bleaching, dyeing and other processes, contains high concentration of non-biodegradable organic compounds, as dyes, that are very difficult to remove [100], [101].

Dyes are organic compounds containing chromophore groups with high solubility in water, which is why it's very difficult to remove them from wastewater by conventional methods [102], [103]. These chemicals are gaining a lot of attention because of the risk they represent to the environment and human health, because of their highly genotoxic and carcinogenic nature [104], [105]. Contact with the skin, inhalation or ingestion, can cause diseases such as dermatitis, kidney disorders, or even cancer, in long-term exposure cases [106], [107], [108]. From an environmental point of view, they are very persistent pollutants that can enter the food chain and cause recalcitrance and bioaccumulation [109], [110]. Furthermore, the colour associated with dyes prevents light from reaching the water, causing not only aesthetic damage but also a reduction of photosynthesis rate and dissolved oxygen levels, affecting the entire aquatic biota [101], [111], [112].

Traditional methods such as coagulation, filtration, precipitation, ion exchange, reverse osmosis and oxidative processes are not always adequate to completely remove dyes from wastewater. This is why other approaches, such as bioremediation and adsorption, have been investigated [113]. In particular, adsorption has proved to be a promising technique because of its high removal capacity of dyes at low concentrations in wastewaters, and because is an advantageous process over the others, offering an easily

designed and low-cost method that is effective against a wide range of contaminants [114]; moreover, it allows the adsorbent material to be reused [115], [116].

Numerous studies have been devoted to the preparation and development of adsorbent materials (raw or processed) for wastewater treatment [117], [118]. Advanced engineered materials, including activated carbon, graphene, carbon nanotubes and hydrogels, but also natural materials such as agricultural and industrial wastes (rice husks, orange juice residues, walnut shells, coconut shell, etc.) have been widely employed in this field [119], [120]. The stability, porosity, high adsorption capacity and modifiable surface groups of HA allow strong interactions between HA and pollutant molecules. In particular, the presence of Ca^{2+} cations and PO_4^{3-} anions facilitates the removal of dyes through electrostatic interactions [104].

References

[1] M. Mongo, V. Laforest, F. Belaid, and A. Tanguy, “Assessment of the Impact of the Circular Economy on CO_2 Emissions in Europe”, 2022, doi: 10.3917/jie.039.0015.

[2] H. T. Pao and C. C. Chen, “The dynamic interaction between circular economy and the environment: Evidence on EU countries”, *Waste Management and Research*, vol. 40, no. 7, pp. 969–979, Jul. 2022, doi: 10.1177/0734242X211057015.

[3] Danish, M. A. Baloch, N. Mahmood, and J. W. Zhang, “Effect of natural resources, renewable energy and economic development on CO_2 emissions in BRICS countries,” *Science of the Total Environment*, vol. 678, pp. 632–638, Aug. 2019, doi: 10.1016/j.scitotenv.2019.05.028.

[4] “https://www.europarl.europa.eu/topics/it/article/20151201STO05603.”

[5] B. Corona, L. Shen, D. Reike, J. Rosales Carreón, and E. Worrell, “Towards sustainable development through the circular economy - A review and critical assessment on current circularity metrics,” *Elsevier B.V.*, Dec. 01, 2019, doi: 10.1016/j.resconrec.2019.104498.

[6] S. Geisendorf and F. Pietrulla, “The circular economy and circular economic concepts—a literature analysis and redefinition,” *Thunderbird International Business Review*, vol. 60, no. 5, pp. 771–782, Sep. 2018, doi: 10.1002/tie.21924.

[7] N. V. Salim, B. Madhan, V. Glattauer, and J. A. M. Ramshaw, “Comprehensive review on collagen extraction from food by-products and waste as a value-added material,” *Elsevier B.V.*, Oct. 01, 2024, doi: 10.1016/j.ijbiomac.2024.134374.

[8] FAO, *Small fish for food security and nutrition*, 2023.

[9] FAO, “Fish in home-grown school feeding - Angola, Hounduras and Perù,” 2021.

[10] M. Chalamaiah, B. Dinesh Kumar, R. Hemalatha, and T. Jyothirmayi, “Fish protein hydrolysates: Proximate composition, amino acid composition, antioxidant activities and applications: A review,” Dec. 15, 2012. doi: 10.1016/j.foodchem.2012.06.100.

[11] FAO, *The State of World Fisheries and Aquaculture 2024*, 2024. doi: 10.4060/cd0683en.

[12] M. Ahmed, A. K. Verma, and R. Patel, “Collagen extraction and recent biological activities of collagen peptides derived from sea-food waste: A review,” *Elsevier B.V.*, Dec. 01, 2020, doi: 10.1016/j.scp.2020.100315.

[13] G. Caruso, “Fishery Wastes and By-products: A Resource to Be Valorised,” 2015, www.fisheriessciences.com

[14] A. E. Ghaly, V. V. Ramakrishnan, M. S. Brooks, S. M. Budge, and D. Dave, “Fish processing wastes as a potential source of proteins, amino acids and oils: A critical review,” *J Microb Biochem Technol*, vol. 5, no. 4, pp. 107-129, 2013, doi: 10.4172/1948-5948.1000110.

[15] E. Dekkers, S. Raghavan, H. G. Kristinsson, and M. R. Marshall, “Oxidative stability of mahi mahi red muscle dipped in tilapia protein hydrolysates,” *Food Chem*, vol. 124, no. 2, pp. 640-645, Jan. 2011, doi: 10.1016/j.foodchem.2010.06.088.

[16] S. L. Bee and Z. A. A. Hamid, “Hydroxyapatite derived from food industry bio-wastes: Syntheses, properties and its potential multifunctional applications,” *Elsevier Ltd.*, Aug. 01, 2020, doi: 10.1016/j.ceramint.2020.04.103.

[17] A. Adamiano *et al.*, “Simultaneous extraction of calcium phosphates and proteins from fish bones. Innovative valorisation of food by-products,” *J Clean Prod*, vol. 385, Jan. 2023, doi: 10.1016/j.jclepro.2022.135656.

[18] P. Kazimierczak, J. Wessely-Szponder, K. Palka, A. Barylyak, V. Zinchenko, and A. Przekora, “Hydroxyapatite or Fluorapatite - Which Bioceramic Is Better as a

Base for the Production of Bone Scaffold? - A Comprehensive Comparative Study," *Int J Mol Sci*, vol. 24, no. 6, Mar. 2023, doi: 10.3390/ijms24065576.

[19] L. D. Esposti, A. C. Ionescu, E. Brambilla, A. Tampieri, and M. Iafisco, "Characterization of a toothpaste containing bioactive hydroxyapatites and in vitro evaluation of its efficacy to remineralize enamel and to occlude dentinal tubules," *Materials*, vol. 13, no. 13, pp. 1-13, Jul. 2020, doi: 10.3390/ma13132928.

[20] S. Hsu, "The relationship between teacher's technology integration ability and usage," *Journal of Educational Computing Research*, vol. 43, no. 3, pp. 309-325, Jan. 2010, doi: 10.2190/EC.43.3.c.

[21] P. Ideia, J. Pinto, R. Ferreira, L. Figueiredo, V. Spínola, and P. C. Castilho, "Fish Processing Industry Residues: A Review of Valuable Products Extraction and Characterization Methods," *Springer*, Jul. 01, 2020, doi: 10.1007/s12649-019-00739-1.

[22] K. S. Vecchio, X. Zhang, J. B. Massie, M. Wang, and C. W. Kim, "Conversion of bulk seashells to biocompatible hydroxyapatite for bone implants," *Acta Biomater*, vol. 3, no. 6, pp. 910-918, 2007, doi: 10.1016/j.actbio.2007.06.003.

[23] P. Terzioğlu, H. Öğüt, and A. Kalemtaş, "Natural calcium phosphates from fish bones and their potential biomedical applications," *Elsevier Ltd.*, Oct. 01, 2018, doi: 10.1016/j.msec.2018.06.010.

[24] F. Carella, L. Degli Esposti, A. Adamiano, and M. Iafisco, "The use of calcium phosphates in cosmetics, state of the art and future perspectives," *Materials*, vol. 14, no. 21, Nov. 2021, doi: 10.3390/ma14216398.

[25] F. Subhan, Z. Hussain, I. Tauseef, A. Shehzad, and F. Wahid, "A review on recent advances and applications of fish collagen," *Bellwether Publishing, Ltd.*, 2021, doi: 10.1080/10408398.2020.1751585.

[26] J. Y. Je, Z. J. Qian, H. G. Byun, and S. K. Kim, “Purification and characterization of an antioxidant peptide obtained from tuna backbone protein by enzymatic hydrolysis,” *Process Biochemistry*, vol. 42, no. 5, pp. 840-846, May 2007, doi: 10.1016/j.procbio.2007.02.006.

[27] M. Rasmussen, M. Jacobsson, and L. Björck, “Genome-based identification and analysis of collagen-related structural motifs in bacterial and viral proteins,” *Journal of Biological Chemistry*, vol. 278, no. 34, pp. 32313-32316, Aug. 2003, doi: 10.1074/jbc.M304709200.

[28] L. Yuan *et al.*, “Topological Structure-Modulated Collagen Carbon as Two-in-One Energy Storage Configuration toward Ultrahigh Power and Energy Density,” *Energy and Environmental Materials*, vol. 7, no. 2, Mar. 2024, doi: 10.1002/eem2.12536.

[29] J. Myllyharju, “Mini-review Prolyl 4-hydroxylases, the key enzymes of collagen biosynthesis,” *Matrix Biology*, vol. 22, pp. 15-24, 2003.

[30] P. Kittiphattanabawon, S. Benjakul, W. Visessanguan, T. Nagai, and M. Tanaka, “Characterisation of acid-soluble collagen from skin and bone of bigeye snapper (Priacanthus tayenus),” *Food Chem*, vol. 89, no. 3, pp. 363-372, Feb. 2005, doi: 10.1016/j.foodchem.2004.02.042.

[31] J. D. S. Antonio, O. Jacenko, A. Fertala, and J. P. R. O. Orgel, “Collagen structure-function mapping informs applications for regenerative medicine,” *MDPI AG.*, Jan. 01, 2021, doi: 10.3390/bioengineering8010003.

[32] S. Ricard-Blum, “The Collagen Family,” *Cold Spring Harb Perspect Biol*, vol. 3, no. 1, pp. 1-19, Jan. 2011, doi: 10.1101/cshperspect.a004978.

[33] J. Chen, C. Burger, C. V. Krishnan, B. Chu, B. S. Hsiao, and M. J. Glimcher, “In vitro mineralization of collagen in demineralized fish bone,” *Macromol Chem Phys*, vol. 206, no. 1, pp. 43-51, Jan. 2005, doi: 10.1002/macp.200400066.

[34] Y. Li and C. Aparicio, “Discerning the Subfibrillar Structure of Mineralized Collagen Fibrils: A Model for the Ultrastructure of Bone,” *PLoS One*, vol. 8, no. 9, Sep. 2013, doi: 10.1371/journal.pone.0076782.

[35] M. Rodrigues, N. Kosaric, C. A. Bonham, and G. C. Gurtner, “Wound Healing: A Cellular Perspective,” *Physiol Rev*, vol. 99, pp. 665-706, 2019, doi: 10.1152/physrev.00067.2017.-Wound.

[36] V. Kolliopoulos and B. A. Harley, “Mineralized collagen scaffolds for regenerative engineering applications,” *Elsevier Ltd*., Apr. 01, 2024, doi: 10.1016/j.copbio.2024.103080.

[37] O. V Frank-Kamenetskaya, Dmitry Yu Vlasov, Elena G Panova, Sofia N Lessovaia, “Lecture Notes in Earth System Sciences Processes and Phenomena on the Boundary Between Biogenic and Abiogenic Nature”, *Springer*, 2020, http://www.springer.com/series/10529

[38] T. Lafarga and M. Hayes, “Bioactive peptides from meat muscle and by-products: Generation, functionality and application as functional ingredients,” *Elsevier Ltd*., 2014, doi: 10.1016/j.meatsci.2014.05.036.

[39] M. M. Schmidt *et al.*, “Collagen extraction process,” 2016.

[40] Z. Barzideh, A. A. Latiff, C. Y. Gan, S. Benjakul, and A. A. Karim, “Isolation and characterisation of collagen from the ribbon jellyfish (Chrysaora sp.),” *Int J Food Sci Technol*, vol. 49, no. 6, pp. 1490-1499, 2014, doi: 10.1111/ijfs.12464.

[41] V. Muralidharan, M. S. Arokianathan, M. Balaraman, and S. Palanivel, “Tannery trimming waste based biodegradable bioplastic: Facile synthesis and characterization of properties,” *Polym Test*, vol. 81, Jan. 2020, doi: 10.1016/j.polymertesting.2019.106250.

[42] B. Ocak, “Development of novel collagen hydrolysate bio-nanocomposite films extracted from hide trimming wastes reinforced with chitosan nanoparticles,” *NIH*, Mar. 2021, doi: 10.1007/s11356-021-13306-w/Published.

[43] C. Cao, Z. Xiao, C. Ge, and Y. Wu, “Animal by-products collagen and derived peptide, as important components of innovative sustainable food systems - a comprehensive review,” *Taylor and Francis Ltd.*, 2022, doi: 10.1080/10408398.2021.1931807.

[44] O. B. Oprea, S. Sannan, I. Tolstorebrov, I. C. Claussen, and L. Gaceu, “Effects of Fish Protein Hydrolysate on the Nutritional, Rheological, Sensorial, and Textural Characteristics of Bread,” *Foods*, vol. 13, no. 5, Mar. 2024, doi: 10.3390/foods13050698.

[45] B. Jadach, Z. Mielcarek, and T. Osmałek, “Use of Collagen in Cosmetic Products,” *Multidisciplinary Digital Publishing Institute (MDPI)*, Mar. 01, 2024, doi: 10.3390/cimb46030132.

[46] DataM Intelligence, “Marine collagen market size, 2024–2031 - https://www.datamintelligence.com/research-report/marine-collagen-market.”

[47] F. Carella, “Synthesis and Characterization of Nanostructured Calcium Phosphate Matrices for Biomedical and Environmental Applications,” Università degli studi di Parma, 2022.

[48] G. Ary *et al.*, “Pathophysiology of premature skin aging induced by ultraviolet light,” *N Engl J Med*, vol. 37, pp. 1419-1428, 1997.

[49] M. Boutinguiza, J. Pou, R. Comesaña, F. Lusquiños, A. De Carlos, and B. León, “Biological hydroxyapatite obtained from fish bones,” *Materials Science and Engineering C*, vol. 32, no. 3, pp. 478–486, Apr. 2012, doi: 10.1016/j.msec.2011.11.021.

[50] A. Fihri, C. Len, R. S. Varma, and A. Solhy, “Hydroxyapatite: A review of syntheses, structure and applications in heterogeneous catalysis,” *Elsevier B.V.*, Sep. 15, 2017, doi: 10.1016/j.ccr.2017.06.009.

[51] M. Okada and T. Matsumoto, “Synthesis and modification of apatite nanoparticles for use in dental and medical applications,” *Elsevier Ltd.*, Nov. 01, 2015, doi: 10.1016/j.jdsr.2015.03.004.

[52] M. Iafisco, A. Ruffini, A. Adamiano, S. Sprio, and A. Tampieri, “Biomimetic magnesium-carbonate-apatite nanocrystals endowed with strontium ions as anti-osteoporotic trigger,” *Materials Science and Engineering C*, vol. 35, no. 1, pp. 212–219, Feb. 2014, doi: 10.1016/j.msec.2013.11.009.

[53] V. Uskoković, “Ion-doped hydroxyapatite: An impasse or the road to follow?” *Elsevier Ltd.*, Jun. 01, 2020, doi: 10.1016/j.ceramint.2020.02.001.

[54] E. Boanini, M. Gazzano, and A. Bigi, “Ionic substitutions in calcium phosphates synthesized at low temperature,” *Elsevier BV.*, 2010, doi: 10.1016/j.actbio.2009.12.041.

[55] N. Eliaz and N. Metoki, “Calcium phosphate bioceramics: A review of their history, structure, properties, coating technologies and biomedical applications,” *Materials*, vol. 10, no. 4, Mar. 2017, doi: 10.3390/ma10040334.

[56] Tavoni Marta, “Development of bioactive bioceramics as delivery systems for regenerative medicine,” Università degli studi di Parma, 2023.

[57] M. Iafisco *et al.*, “Fluoride-doped amorphous calcium phosphate nanoparticles as a promising biomimetic material for dental remineralization,” *Sci Rep*, vol. 8, no. 1, Dec. 2018, doi: 10.1038/s41598-018-35258-x.

[58] S. V. Dorozhkin, “Calcium orthophosphates,” *J Mater Sci*, vol. 42, no. 4, pp. 1061-1095, Feb. 2007, doi: 10.1007/s10853-006-1467-8.

[59] N. Roveri, B. Palazzo, and M. Iafisco, “The role of biomimetism in developing nanostructured inorganic matrices for drug delivery,” Aug. 2008. doi: 10.1517/17425247.5.8.861.

[60] M. J. Olszta *et al.*, “Bone structure and formation: A new perspective,” Nov. 28, 2007, doi: 10.1016/j.mser.2007.05.001.

[61] S. V. Dorozhkin, “Nanosized and nanocrystalline calcium orthophosphates,” *Elsevier Ltd.*, 2010, doi: 10.1016/j.actbio.2009.10.031.

[62] S. Sprio *et al.*, “Physico-chemical properties and solubility behaviour of multi-substituted hydroxyapatite powders containing silicon,” *Materials Science and Engineering C*, vol. 28, no. 1, pp. 179-187, Jan. 2008, doi: 10.1016/j.msec.2006.11.009.

[63] J. Chou *et al.*, “Strontium- and magnesium-enriched biomimetic β-TCP macrospheres with potential for bone tissue morphogenesis,” *J Tissue Eng Regen Med*, vol. 8, no. 10, pp. 771-778, Oct. 2014, doi: 10.1002/term.1576.

[64] D. T. Zero, “Dentifrices, mouthwashes, and remineralization/caries arrestment strategies,” *BMC Oral Health*, *BioMed Central Ltd.*, Jan. 2006, doi: 10.1186/1472-6831-6-S1-S9.

[65] A. M. E. Matinong, Y. Chisti, K. L. Pickering, and R. G. Haverkamp, “Collagen Extraction from Animal Skin,” *MDPI*, Jun. 01, 2022, doi: 10.3390/biology11060905.

[66] E. Skierka and M. Sadowska, “The influence of different acids and pepsin on the extractability of collagen from the skin of Baltic cod (Gadus morhua),” *Food Chem*, vol. 105, no. 3, pp. 1302-1306, 2007, doi: 10.1016/j.foodchem.2007.04.030.

[67] C. F. Ramirez-Gutierrez, A. F. Palechor-Ocampo, S. M. Londoño-Restrepo, B. M. Millán-Malo, and M. E. Rodriguez-García, “Cooling rate effects on thermal, structural, and microstructural properties of bio-hydroxyapatite obtained from bovine bone,” *J Biomed Mater Res B Appl Biomater*, vol. 104, no. 2, pp. 339-344, Feb. 2016, doi: 10.1002/jbm.b.33401.

[68] M. Figueiredo, A. Fernando, G. Martins, J. Freitas, F. Judas, and H. Figueiredo, "Effect of the calcination temperature on the composition and microstructure of hydroxyapatite derived from human and animal bone," *Ceram Int*, vol. 36, no. 8, pp. 2383-2393, Dec. 2010, doi: 10.1016/j.ceramint.2010.07.016.

[69] W. Pon-On, P. Suntornsaratoon, N. Charoenphandhu, J. Thongbunchoo, N. Krishnamra, and I. M. Tang, "Hydroxyapatite from fish scale for potential use as bone scaffold or regenerative material," *Materials Science and Engineering C*, vol. 62, pp. 183-189, May 2016, doi: 10.1016/j.msec.2016.01.051.

[70] N. Muhammad *et al.*, "Extraction of biocompatible hydroxyapatite from fish scales using novel approach of ionic liquid pretreatment," *Sep Purif Technol*, vol. 161, pp. 129-135, Mar. 2016, doi: 10.1016/j.seppur.2016.01.047.

[71] Disqover Agency, "https://www.fda.gov/industry/regulated-products/cosmetics-overview.LpLqzmdIM5bnpv4sb_QrsK_-s-xLFBwZ3KTRoCjgYQAvD_BwE."

[72] M. F. Mesko, D. L. R. Novo, V. C. Costa, A. S. Henn, and E. M. M. Flores, "Toxic and potentially toxic elements determination in cosmetics used for make-up: A critical review," *Elsevier B.V.*, Feb. 15, 2020, doi: 10.1016/j.aca.2019.11.046.

[73] N. Matwiejczuk, A. Galicka, and M. M. Brzóska, "Review of the safety of application of cosmetic products containing parabens," *John Wiley and Sons Ltd.*, Jan. 01, 2020, doi: 10.1002/jat.3917.

[74] M. Bilal and H. M. N. Iqbal, "An insight into toxicity and human-health-related adverse consequences of cosmeceuticals - A review," *Elsevier B.V.*, Jun. 20, 2019, doi: 10.1016/j.scitotenv.2019.03.261.

[75] R. Feizi, N. Jaafarzadeh, H. Akbari, and S. Jorfi, "Evaluation of lead and cadmium concentrations in lipstick and eye pencil cosmetics," *Environmental Health Engineering and Management*, vol. 6, no. 4, pp. 277-282, Sep. 2019, doi: 10.15171/EHEM.2019.31.

[76] M. Bilal, S. Mehmood, and H. M. N. Iqbal, “The beast of beauty: Environmental and health concerns of toxic components in cosmetics,” *MDPI AG.*, Mar. 01, 2020, doi: 10.3390/cosmetics7010013.

[77] Madhu A. and Pathak M.B., “Sunscreens: Topical and systemic approaches for protection of human skin against harmful effects of solar radiation,” *J Am Acad Dermatol*, vol. 7, no. 3, pp. 285-312, Sep. 1982.

[78] Green Adèle *et al.*, “Daily sunscreen application and betacarotene supplementation in prevention of basal-cell and squamous-cell carcinomas of the skin: a randomised controlled trial,” *The Lancet*, vol. 354, pp. 723-729, Aug. 1999.

[79] Y. Huang, J. C. F. Law, T. K. Lam, and K. S. Y. Leung, “Risks of organic UV filters: a review of environmental and human health concern studies,” *Elsevier B.V.*, Feb. 10, 2021, doi: 10.1016/j.scitotenv.2020.142486.

[80] J. Labille *et al.*, “Assessing Sunscreen Lifecycle to Minimize Environmental Risk Posed by Nanoparticulate UV-Filters - A Review for Safer-by-Design Products,” *Frontiers Media S.A.*, Jul. 10, 2020, doi: 10.3389/fenvs.2020.00101.

[81] S. Narla and H. W. Lim, “Sunscreen: FDA regulation, and environmental and health impact,” *Photochemical and Photobiological Sciences*, vol. 19, no. 1, pp. 66-70, 2020, doi: 10.1039/c9pp00366e.

[82] A. Hunter and M. Trevino, “Film-Formers Enhance Water Resistance and SPF in Sun Care Products,” 2004, www.TheCosmeticSite.com.

[83] J. K. Volkman, G. Eglinton, E. D. S. Cornert, and T. E. V Forseergt, “Long-chain alkenes and alkanones in the marine coccolithophorid emiliana huxleyz,” 1980.

[84] S. Singh, B. N. Kate, and U. C. Banecjee, “Bioactive compounds from cyanobacteria and microalgae: An overview,” 2005. doi: 10.1080/07388550500248498.

[85] G. W. O'Neil, J. R. Williams, A. M. Craig, R. K. Nelson, K. M. Gosselin, and C. M. Reddy, "Accessing Monomers, Surfactants, and the Queen Bee Substance by Acrylate Cross-Metathesis of Long-Chain Alkenones," *JAOCS, Journal of the American Oil Chemists' Society*, vol. 94, no. 6, pp. 831-840, Jun. 2017, doi: 10.1007/s11746-017-2997-8.

[86] M. R. Brown, M. Mular, I. Miller, C. Farmer, and & C. Trenerry, "The vitamin content of microalgae used in aquaculture," 1999.

[87] J. R. Lechien *et al.*, "Reflux and Dental Disorders in The Pediatric Population: A Systematic Review. Institutions: 1. Laryngopharyngeal Reflux Study Group of Young-Otolaryngologists of the International Federations of Oto-rhino-laryngological Societies (YO-IFOS)," 2020.

[88] A. C. Ionescu, L. Degli Esposti, M. Iafisco, and E. Brambilla, "Dental tissue remineralization by bioactive calcium phosphate nanoparticles formulations," *Sci Rep*, vol. 12, no. 1, Dec. 2022, doi: 10.1038/s41598-022-09787-5.

[89] P. D. Marsh, "Dental plaque as a biofilm: The significance of pH in health and caries," *Compend. Contin. Educ. Dent*, vol. 30, no. 2, pp. 76-78, 2009.

[90] W. I. D. caries Caries, "Etiology, clinical characteristics, risk assessment, and management," *Elsevier - Sturdevant's Art & Science of Operative Dentistry-E-Book*, Amsterdam, 2017.

[91] O. Fejerskov, B. Nyvad, and E. Kidd, "Dental Caries: The Disease and Its Clinical Management," *John Wiley & Sons*, 2015.

[92] I. Farooq and A. Bugshan, "The role of salivary contents and modern technologies in the remineralization of dental enamel: A review," *F1000Res*, vol. 9, 2020, doi: 10.12688/f1000research.22499.1.

[93] M. Iafisco *et al.*, "Fluoride-doped amorphous calcium phosphate nanoparticles as a promising biomimetic material for dental remineralization," *Sci Rep*, vol. 8, no. 1, Dec. 2018, doi: 10.1038/s41598-018-35258-x.

[94] R. S. Lacruz, S. Habelitz, J. T. Wright, and M. L. Paine, “Dental enamel formation and implications for oral health and disease,” *Physiol Rev*, vol. 97, pp. 939-993, 2017, doi: 10.1152/physrev.00030.2016.-Dental.

[95] L. C. Palmer, C. J. Newcomb, S. R. Kaltz, E. D. Spoerke, and S. I. Stupp, “Biomimetic systems for hydroxyapatite mineralization inspired by bone and enamel,” *Chem Rev*, vol. 108, no. 11, pp. 4754-4783, Nov. 2008, doi: 10.1021/cr8004422.

[96] N. Roveri *et al.*, “Surface enamel remineralization: Biomimetic apatite nanocrystals and fluoride ions different effects,” *J Nanomater*, vol. 2009, 2009, doi: 10.1155/2009/746383.

[97] M. N. Hassan, M. M. Mahmoud, A. A. El-Fattah, and S. Kandil, “Microwave-assisted preparation of Nano-hydroxyapatite for bone substitutes,” *Elsevier Ltd.*, Feb. 15, 2016, doi: 10.1016/j.ceramint.2015.11.044.

[98] M. Vallet-Regí and D. Arcos, “Bioceramics for drug delivery,” *Acta Mater*, vol. 61, no. 3, pp. 890-911, Feb. 2013, doi: 10.1016/j.actamat.2012.10.039.

[99] S. V. Dorozhkin, “BIOMATERIALS FOR MEDICINE BIOCERAMICS BASED ON CALCIUM ORTHOPHOSPHATES (REVIEW),” 2007.

[100] S. C. Bhatia, *“Pollution control in textile industry”, Woodhead Publishing India*, 2017.

[101] B. Lellis, C. Z. Fávaro-Polonio, J. A. Pamphile, and J. C. Polonio, “Effects of textile dyes on health and the environment and bioremediation potential of living organisms,” *Biotechnology Research and Innovation*, vol. 3, no. 2, pp. 275-290, Jul. 2019, doi: 10.1016/j.biori.2019.09.001.

[102] M. M. Hassan and C. M. Carr, “A critical review on recent advancements of the removal of reactive dyes from dyehouse effluent by ion-exchange adsorbents,” *Elsevier Ltd.*, Oct. 01, 2018, doi: 10.1016/j.chemosphere.2018.06.043.

[103] R. Shamey and X. Zhao, “Modelling, simulation and controlof the dyeing process”, *The Textile Institute - Woodhead publishing*, 2014.

[104] S. Pai, & M. S. Kini, and R. Selvaraj, “A review on adsorptive removal of dyes from wastewater by hydroxyapatite nanocomposites,” *Environmental and energy management,* vol. 28, pp. 11835-11849, Dec. 2019, doi: 10.1007/s11356-019-07319-9/Published.

[105] K. Fernandes, D. Chicco, J. S. Cardoso, and J. Fernandes, “Supervised deep learning embeddings for the prediction of cervical cancer diagnosis,” *PeerJ Comput Sci*, vol. 2018, no. 5, May 2018, doi: 10.7717/peerj-cs.154.

[106] F. Akarslan and H. Demiralay, “Effects of textile materials harmful to human health,” *Acta Physica Polonica A*, Polska Akademia Nauk, Aug. 2015, pp. 407-408. doi: 10.12693/APhysPolA.128.B-407.

[107] Jayraj Khatri, P.V. Nidheesh, T.S. Anantha Singh, and M. Suresh Kumar, “Advanced oxidation processes based on zero-valent aluminium for treating textile wastewater,” *Chemical Engineering Journal*, vol. 348, pp. 67-73, Sep. 2018.

[108] José M. Aquino, Romeu C. Rocha-Filho, Luís A.M. Ruotolo, Nerilso Bocchi, and Sonia R. Biaggio, “Electrochemical degradation of a real textile wastewater using β-PbO_2 and DSA® anodes,” *Chemical Engineering Journal*, vol. 251, pp. 138-145, Sep. 2014.

[109] M. C. Newman, “The Science of Pollution FOURTH EDITION,” 2015.

[110] S. Sandhya, “Biodegradation of Azo Dyes Under Anaerobic Condition: Role of Azoreductase,” 2010, pp. 39–57. doi: 10.1007/698_2009_43.

[111] T. Setiadi, Y. Andriani, and M. Erlania, “Treatment of Textile Wastewater by a Combination of Anaerobic and Aerobic Processes: A Denim Processing Plant Case,” 2003.

[112] M. Imran, D. E. Crowley, A. Khalid, S. Hussain, M. W. Mumtaz, and M. Arshad, "Microbial biotechnology for decolorization of textile wastewaters," *Kluwer Academic Publishers,* Mar. 01, 2015, doi: 10.1007/s11157-014-9344-4.

[113] A. G. B. Pereira, F. H. A. Rodrigues, A. T. Paulino, A. F. Martins, and A. R. Fajardo, "Recent advances on composite hydrogels designed for the remediation of dye-contaminated water and wastewater: A review," *Elsevier Ltd*., Feb. 15, 2021, doi: 10.1016/j.jclepro.2020.124703.

[114] M. T. Amin, A. A. Alazba, and U. Manzoor, "A review of removal of pollutants from water/wastewater using different types of nanomaterials," *Hindawi Publishing Corporation*, 2014, doi: 10.1155/2014/825910.

[115] E. F. Lessa, M. S. Gularte, E. S. Garcia, and A. R. Fajardo, "Orange waste: A valuable carbohydrate source for the development of beads with enhanced adsorption properties for cationic dyes," *Carbohydr Polym*, vol. 157, pp. 660-668, Feb. 2017, doi: 10.1016/j.carbpol.2016.10.019.

[116] J. Wang, T. Tsuzuki, B. Tang, X. Hou, L. Sun, and X. Wang, "Reduced graphene oxide/ZnO composite: Reusable adsorbent for pollutant management," *ACS Appl Mater Interfaces*, vol. 4, no. 6, pp. 3084-3090, Jun. 2012, doi: 10.1021/am300445f.

[117] N. Maqbool, Z. Khan, and A. Asghar, "Reuse of alum sludge for phosphorus removal from municipal wastewater," *Desalination Water Treat*, vol. 57, no. 28, pp. 13246-13254, Jun. 2016, doi: 10.1080/19443994.2015.1055806.

[118] H. Tajizadegan, O. Torabi, A. Heidary, M. H. Golabgir, and A. Jamshidi, "Study of methyl orange adsorption properties on ZnO-Al_2O_3 nanocomposite adsorbent particles," *Desalination Water Treat*, vol. 57, no. 26, pp. 12324-12334, Jun. 2016, doi: 10.1080/19443994.2015.1049558.

[119] Q. Ma, Y. Yu, M. Sindoro, A. G. Fane, R. Wang, and H. Zhang, “Carbon-Based Functional Materials Derived from Waste for Water Remediation and Energy Storage,” Apr. 04, 2017, *Wiley-VCH Verlag*. doi: 10.1002/adma.201605361.

[120] M. B. Shakoor *et al.*, “Remediation of arsenic-contaminated water using agricultural wastes as biosorbents,” *Crit Rev Environ Sci Technol*, vol. 46, no. 5, pp. 467-499, Mar. 2016, doi: 10.1080/10643389.2015.1109910.

CHAPTER II: SIMULTANEOUS EXTRACTIONS OF HA & COL FROM FISH BONES

2.1. Introduction

The realisation of sustainable development is becoming increasingly important for our society. To achieve this, several measures designed to reduce the amount of waste generated by production processes need to be implemented. For instance, chemical preparation and synthesis processes should favour non-toxic solvents and avoid highly acidic media [1], [2], [3], [4]. Furthermore, the extensive use of limited resources should be minimised, as it can lead to long-term problems, such as limited future availability of essential materials.

Fishbones are one of the most abundant food by-products globally. For this reason, they have been extensively studied for valorisation, as they contain a number of promising compounds, both organic and inorganic. As already mentioned above, the organic fraction mainly consists of fats and proteins, particularly Col, while the inorganic part is mainly composed of CaPs, typically in the form of HA [5], [6]. Typical extraction processes for Col from fish bones often involve acid solvents, which can pose significant environmental drawbacks. These include the generation of acidic wastewater that requires extensive neutralisation before disposal, potentially releasing harmful by-products into aquatic ecosystems if improperly managed. The processes also consume considerable amounts of water and energy, adding to their environmental footprint. Additionally, reliance on chemical reagents can contribute to resource depletion and environmental contamination, making these methods less sustainable compared to emerging greener alternatives [7], [8], [9].

In this work, three different extraction methods for the simultaneous isolation of HA and Col from salmon bones were investigated:

- extraction with an ionic liquid and a deep eutectic solvent.
- alkaline hydrolysis.
- enzymatic extractions.

These methods have been investigated as they represent a greener alternative to the conventional acidic dissolution and enable the extraction of the mineral fraction of the fish bones without dissolving the organic phase which can subsequently be recovered - a feature not achievable with conventional extraction methods [10], [11], [12].

2.1.1. Ionic Liquids & Deep Eutectic Solvents

Ionic liquids (ILs) are salts that exist in a liquid state at room temperature. They are well-known and used because they can be tuned to specific applications and are considered to be a more environmentally friendly alternative to traditional solvents, as they can be recovered after the process [13]. Besides, they have many interesting properties such as negligible vapour pressures, selectivity and higher extraction yields [13], [14], [15]. Due to these distinctive characteristics and to their strong ability to break hydrogen bonds, they have been employed as solvents for many natural polymers, such as cellulose, chitosan, chitin, collagen, silk, etc [16], [17].

The ionic liquid employed in this study is 1-butyl-3-methylimidazole hexafluorophosphate (BMIM). BMIM has been selected as it's one of the most used ionic liquids in the literature due to its solvation capacity, thermal stability and zero vapour pressure. As an example, C. Samorì et al. used ionic liquids as solvent for several organic synthesis processes, such as the allylation of 2-octanone, and have demonstrated that these molecules can represent a safer and more environmental friendly alternative to chlorinated solvent [18], [19].

Deep Eutectic Solvents (DESs) are mixtures composed of a hydrogen bond donor and a hydrogen acceptor with specific molar ratios. They are widely used for the extraction of biologically active natural compounds due to their biodegradability and low toxicity [20]. Among the many DESs, those formed from combinations of different amounts of choline chloride and glycerol are the most common [21] due to the degradability of glycerol and their structural characteristics, which facilitate the dissolution of hydrogen bonds in biological macromolecules. Like ILs, DESs have a low vapour pressure, an adaptable chemical composition and can be recovered at the end of the extraction processes [17].

The DES employed in this study was constituted by choline chloride and glycerol in a 1:2 molar ratio. This DES is also common in the literature and is often used for the extraction of HA from animal bones [22] or from food waste [23], [24]. In particular,

Yanhong Liu et al. have successfully extracted HA from bighead carp (*Aristichthys nobilis*) bones using this eutectic solvent [25].

2.1.2. Alkaline hydrolysis

Following the work of Piccirillo et al. on alkaline hydrolysis, this work investigated the effect of different process parameters on organic and inorganic extraction yields and estimated Col content. The use of a saline solution consisting of $(NH_4)_2HPO_4$ and $(NH_4)HCO_3$, thanks to the basic pH, ensures the preservation of the mineral fraction of the bones during the process, so similar protocols were used to simultaneously extract both organic and inorganic components from salmon bones (*Salmo salar*). The choice of salmon was driven by the fact that it is one of the most widely consumed fish species in the world, with the United States ranking its consumption second only to shrimp [26], [27].

2.1.3. Enzymatic extractions

Enzymatic extraction has many advantages over other extraction methods in terms of speed and reaction conditions, energy consumption and environmental pollution [28], [29]. The use of enzymes has also been demonstrated to increase the yields of Col extraction, especially when used in combination with ultrasound [30].

Three different enzymes were used in this study: trypsin, papain and pepsin. Each extraction was conducted under the optimal conditions of enzymatic activity of the individual enzyme, in terms of extraction time, temperature and pH [31].

2.2. Materials & methods

Salmon bones were provided by a local enterprise. The following reagents were from Sigma Aldrich: *ammonium bicarbonate* (purity > 99%), *Chloramine-T* (95% hydrate solution), *sodium acetate anhydrous* (high purity), *citric acid monohydrate* (ACS reagent, purity ≥ 99.0%), *sodium hydroxide anhydrous* (NaOH, BioXtra, purity ≥ 98%), *p-dimethylaminobenzaldehyde* (ACS reagent, 99% pure), *hydrocloridric acid* (HCl 37%, ACS reagent), c*hloroform* ($CHCl_3$, Emprove® Essential), *glycerol* (ACS reagent, purity ≥ 99.5%), *citric acid, sodium chloride* (anhydrous, Redi-Dri™, free-flowing, ACS reagent, purity ≥ 99%), *ethanol absolute, 2-propanol*, *choline chloride* (purity ≥ 98%), *Trypsin* (Proteomics Grade, BioReagent, dimethylated), *Papain* (from papaya latex, lyophilized powder) and *Pepsin* (lyophilized, salt-free). *Glacial acetic acid* was supplied by Carlo Erba, while *acetone* by Novachimica and *1-butyl-3-methylimidazole hexafluorophosphate* by Alfa-aesar.

2.2.1. Extractions with ionic liquid & deep eutectic solvent

Extractions protocol are represented in Figure 6. Degreased and dried bones were placed in contact with BMIM/DES (1:10 g/g compared to non-degreased bones) and extraction was carried out under magnetic stirring for 2.5/5/24h at 100°C. The extraction solution was centrifuged at 10000 rpm for 5' and the supernatant and the *extraction residue* were separated. The residue was washed 3 times with acetone and bi-distilled water, completely dried at 40°C in a laboratory stove and calcined at 850°C for 2h with a ramp of 120°C/h, to obtain the *mineral phase*. The supernatant, containing the extracted Col, was degreased by placing it in contact with ~ 2 mL of CH_3Cl for ~ 30', then dialyzed against 2.5 L of bi-distilled water for 48h using a Spectra/Por membrane (MWCO = 50 kDa). The solution was then obtained by precipitation with absolute ethanol. After 30' the solution was centrifuged at 14000 rpm for 5' and the pellet was lyophilised to obtain the *organic phase*.

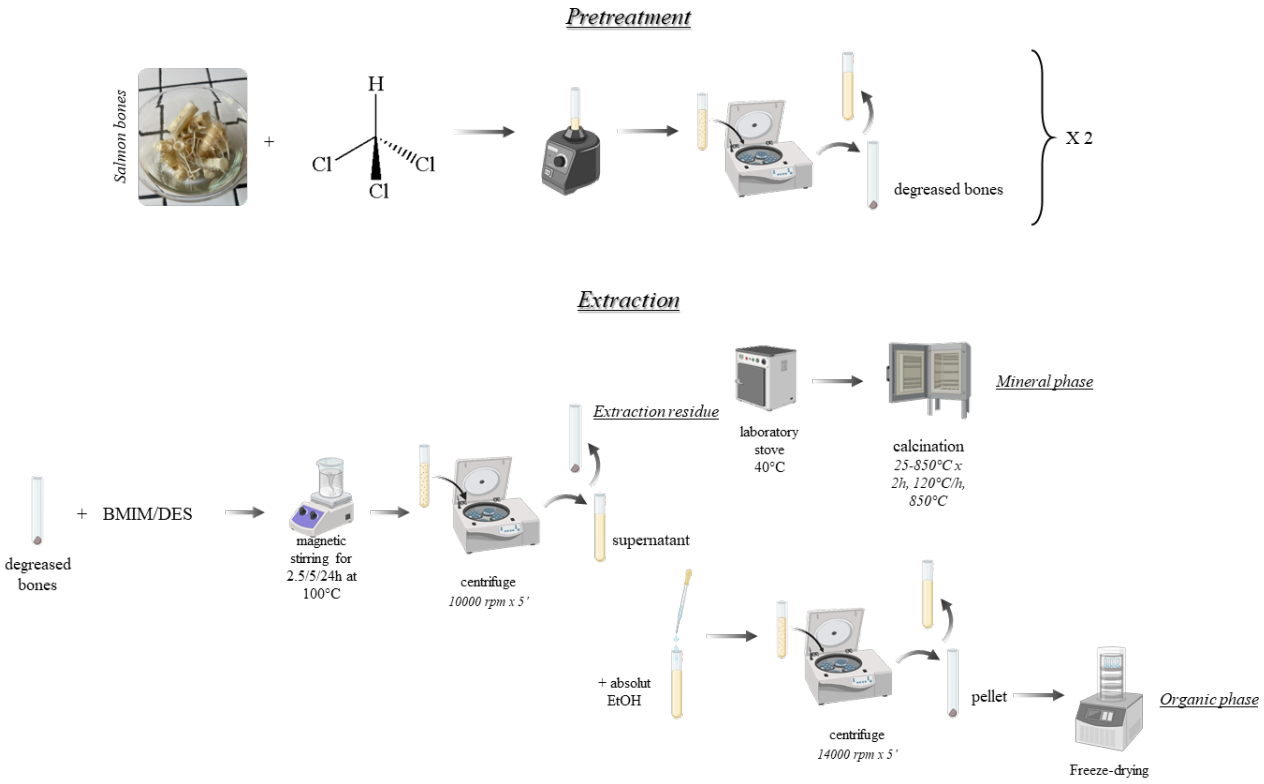

Figure 6. Extraction protocol of HA & Col with BMIM/DES

2.2.2. Alkaline hydrolysis

Salmon bones were freeze-dried and stored at - 20°C. Figure 7 illustrates the steps of the extraction protocol. Approximately 2 g of grinded salmon bones were treated with 20 mL of ammonium bicarbonate (0.2M, pH = 8) under magnetic stirring for different times (4 and 24h) at different temperatures (30 and 60°C). As ultrasounds have been reported to accelerate hydrolysis and enhance Col extraction, in a set of experiments bone samples were subjected to a 1h pre-treatment using a tip sonicator to investigate the effect of ultrasounds on the extraction efficacy [32], [33]. The extraction solutions were centrifuged at 10000 rpm for 5' and the supernatant and the *extraction residue* were separated. The residue was washed 3 times with bi-distilled water, dried at 40°C in a laboratory stove and calcined at 850°C for 2h with a heating ramp of 120°C/h, to obtain the *mineral phase*. The supernatant, containing the extracted Col, was degreased by placing it in contact with ~2 mL of CH_3Cl for ~30', then dialyzed against 2.5 L of bi-distilled water for 48h using a Spectra/Por membrane (MWCO = 8 kDa). The dialyzed solution was subsequently freeze-dried to isolate the *organic phase.*

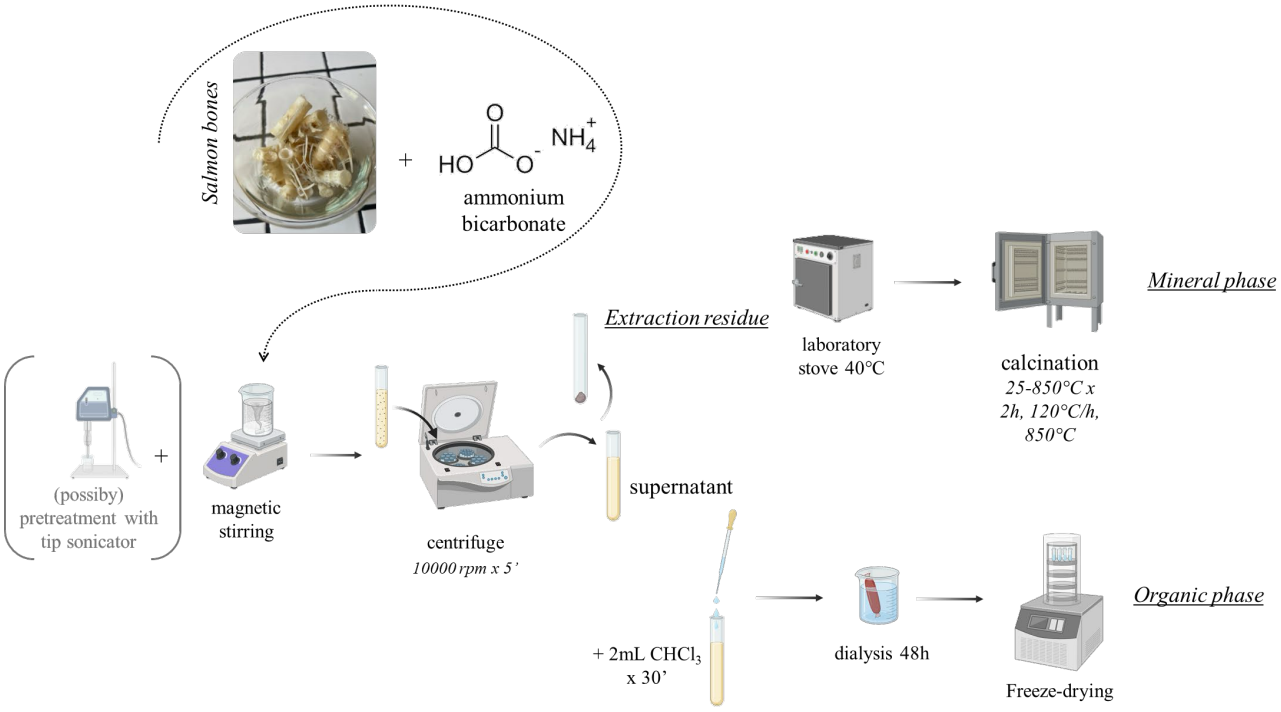

Figure 7. Alkaline hydrolysis protocol for HA & Col simultaneous extraction

As a control, unextracted salmon bones were calcined in the same way as the extracted ones. The samples obtained were named as shown in Table 1:

Table 1. Samples names and extraction conditions

	Pretreatment	**Extraction time (h)**	**Temperature (°C)**
Pre_4h 30°C	Yes	4	30
Pre_24h 30°C	Yes	24	30
4h 30°C	No	4	30
24h 30°C	No	24	30
Pre_4h 60°C	Yes	4	60
Pre_24h 60°C	Yes	24	60
4h 60°C	No	4	60
24h 60°C	No	24	60

Design of Experiment

A Design of Experiment (DoE) approach was adopted to study the simultaneous extraction of HA and Col from salmon bones by alkaline hydrolysis, using the Minitab software supplied by GMSL S.r.l., to identify the significant process variables (factors) and maximise the mineral yield, organic yield and estimated Col amount, defined as observables, or responses.

The approach chosen for the complete two-level factorial design allows for the simultaneous study of the effect of several factors varying between two specific levels on the process and the measurement of all combinations between the levels of the different experimental factors. These combinations represent the experimental conditions under which the observables are measured. Each experimental condition is called a "run" and the design represents the set of runs.

Three factors were selected, varying between 2 levels each (DoE 3x2) and 3 replicates per run, for a total of 24 randomised runs.

The factors used were:

- extraction time (4/24h).
- extraction temperature (30/60°C).
- pretreatment with tip sonicator (Yes/No).

The observations were then evaluated using Pareto diagrams, analysis of variance, main effects and interaction diagrams, and residue analysis.

The experiments were conducted by varying each level of each factor at a time to predict future possible results with non-tested experiment setting and thus to optimize the extraction yields.

2.2.3. Enzymatic extractions

The conditions of the three enzyme extractions studied are reported in Table 2, while the individual processes are described in the following sub-chapters.

Table 2. Enzymatic extractions conditions

	Trypsin	*Papain*	*Pepsin*
Extraction solution	Ammonium bicarbonate 0.2M	Ammonium bicarbonate 0.2M	Citrate buffer 0.5M
Pre-treatment time (h)	1	1	/
Extraction time (h)	4	4	24
Extraction T (°C)	45	45	4
pH	8.2	7.0	5.6
Enzyme amount (%)	1.0	1.0	1.5

For each enzyme extraction, a control sample (CTRL) was extracted under identical conditions, but without the enzyme. Samples extracted were named like the used enzyme, so Trypsin, Papain and Pepsin.

Trypsin/Papain extraction protocols

Salmon bones were freeze-dried and stored at - 20°C. Figure 8 shows the various steps of the extraction protocol followed for papain and trypsin extractions. After pretreating 2 g of bones with 20 mL of ammonium bicarbonate 0.2 M and tip sonicator (as already described for alkaline hydrolysis), a 1% by weight (relative to the initial weight of the bones) of the enzyme was added and the extraction was conducted under magnetic stirring for 4h at 45°C. As for the alkaline hydrolysis, the extraction solution was centrifuged at 10000 rpm for 5' and the supernatant and the *extraction residue* were separated. The residue was washed 3 times with bi-distilled water, dried at 40°C in a laboratory stove and calcined at 850°C for 2h with a heating ramp of 120°C/h, to obtain the *mineral phase*. The supernatant, containing the extracted Col, was degreased by placing it in contact with ~ 2 mL of CH_3Cl for ~ 30', then dialyzed against 2.5 L of bi-distilled water for 48h using a Spectra/Por membrane (MWCO = 50 kDa). The dialyzed solution was subsequently freeze-dried to isolate the *organic phase.*

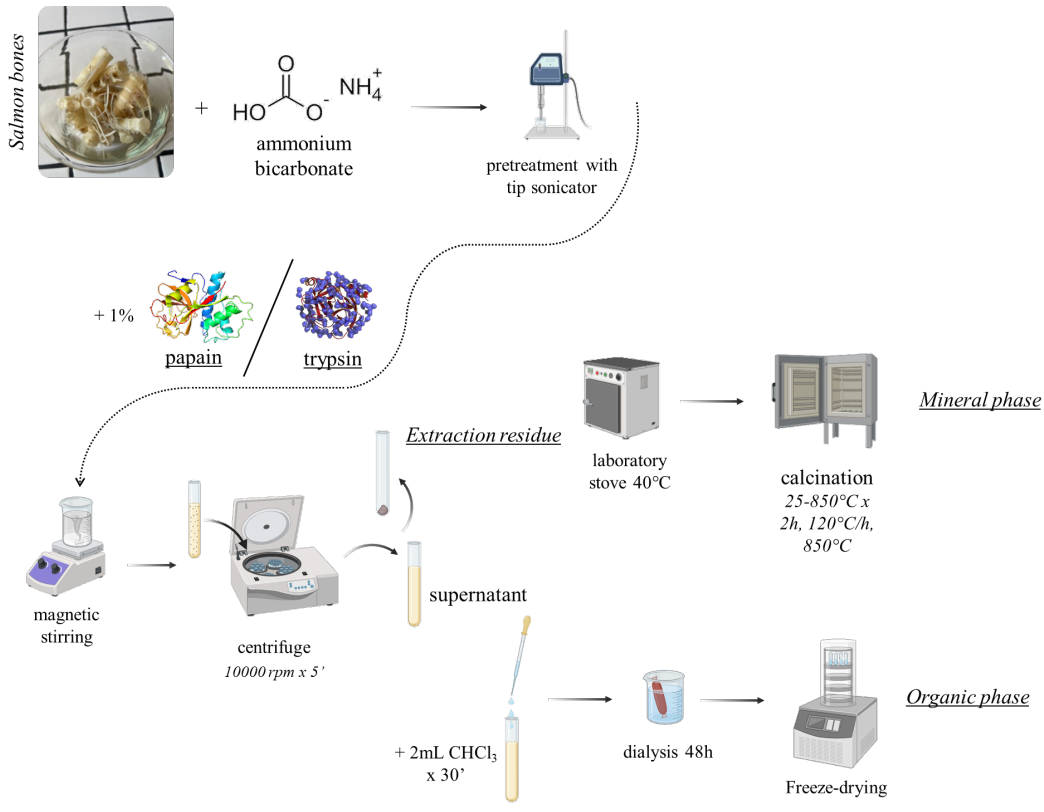

Figure 8. Extraction protocol of HA & Col with papain/trypsin

Pepsin extraction protocol

Figure 9 shows the various steps of the pepsin extraction protocol. Approximately 2 g of salmon bones were placed in contact with 20 mL of citrate buffer 0.5 M, 1.5% by weight (relative to the initial weight of the bones) of the pepsin was added and extraction was conducted under magnetic stirring for 24h at 4°C. As before, the extraction solution was centrifuged at 10000 rpm for 5' and the supernatant and *extraction residue* were separated. The residue was washed 3 times with bi-distilled water, dried at 40°C in a laboratory stove and calcined at 850°C for 2h with a heating ramp of 120°C/h, to obtain the *mineral phase*. The supernatant, containing the extracted Col, was degreased by placing it in contact with ~ 2 mL of CH_3Cl for ~ 30', then dialyzed against 2.5 L of bi-distilled water for 48h using a Spectra/Por membrane (MWCO = 50 kDa). The *organic phase* was then obtained by salting with a 25% NaCl solution to a concentration of 0.7 M; after 30' the solution was centrifuged at 14550 rpm for 20' at 4°C and the pellet was lyophilised.

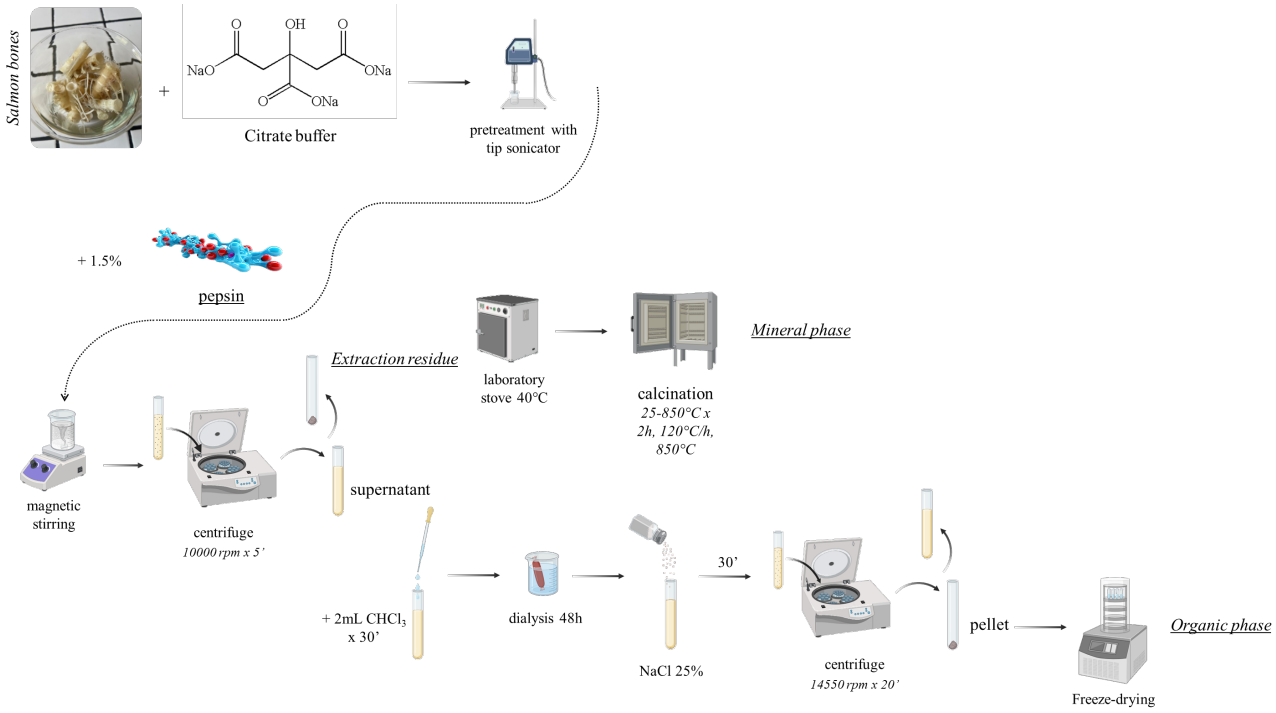

Figure 9. Extraction protocol of HA & Col with pepsin

2.3. Characterisations

Organic phases

Fourier transform infrared spectroscopy analyses in attenuated total reflection mode (*FTIR-ATR*) were carried out using a Nicolet iS5 spectrometer (Thermo Fisher Scientific Inc., Waltham, MA, USA) with a resolution of 1 cm^{-1} by accumulation of 16 scans covering the 4000 to 400 cm^{-1} range, using a diamond ATR accessory model iD7. The integrity of the collagen triple helix was evaluated by considering the ratio of the peaks at ν = 1235 cm^{-1} and ν = 1450 cm^{-1}, corresponding to the maximum absorbance of amide III and the pyrrolidine rings of the proline and hydroxyproline residues, respectively. The triple helix structure is considered intact when the ratio is close to 1.0, whereas it's denatured when the ratio values are around 0.5 [34].

The Col content within the organic phase was indirectly estimated by *hydroxyproline assay* following the extraction mechanism illustrated in Figure 10 [35]. Three aliquots of each lyophilised organic phase were placed in Eppendorf tubes with a loose stopper and dissolved in 100 µL of NaOH 4 M. After one autoclave cycle (121°C, 15 psi), the solutions were neutralised with 100 µL of HCl 4 M. After cooling to RT, 625 µL of a 0.05 M solution of Chloramine-T was added. It is composed of a solution formed by 26% 2-propanol and 74% citrate buffer as composed: 0.629 M NaOH. 0.140 M citric acid monohydrate, 0.453 M anhydrous sodium acetate and glacial acetic acid, to give a pH of 4.5. The liquids were kept in contact for 20', followed by the addition of 625 µL of fresh Ehrlich's reagent (15 g p-dimethylaminobenzaldehyde dissolved in 100 mL of 2-propanol/HCl, 70:30 v/v), which allows the formation of chromophore [36]. The solutions were heated at 65°C for 20' and then quenched in cold water.

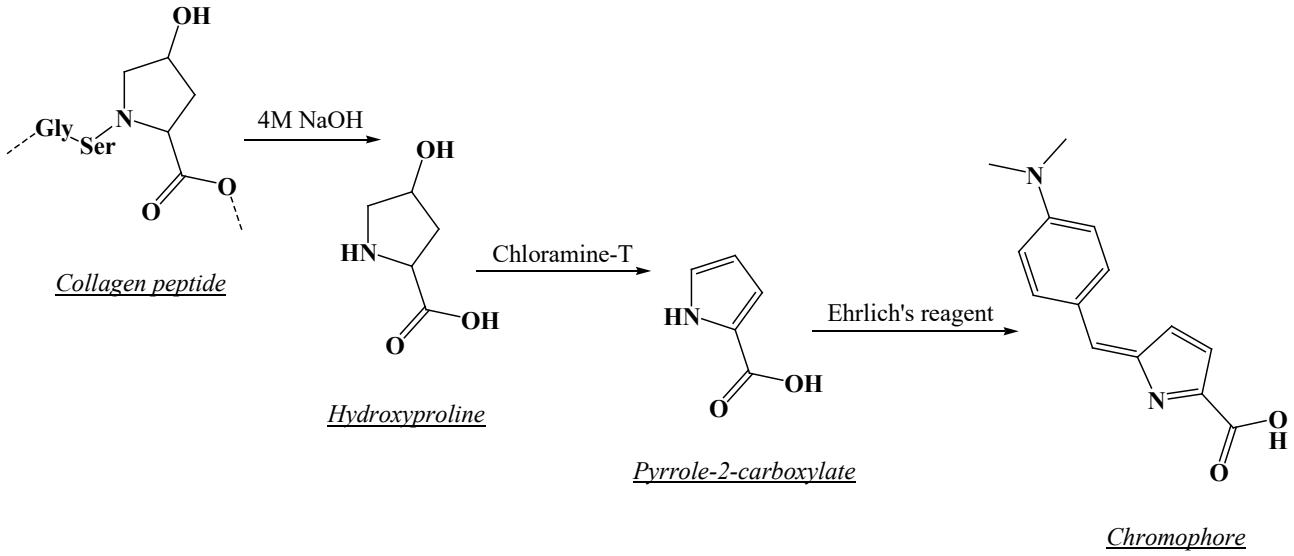

Figure 10. Chemical reactions of the hydroxyproline assay: hydrolysation of Col peptide. oxidation of the hydroxylated amino ring of hydroxyproline. chromophore production

A calibration curve ranging from 0 to 500 μg/mL was prepared to determine the hydroxyproline content. The absorbance of the solutions was measured at 570 nm using a NanoDrop spectrophotometer (NanoDrop OneC, Thermo Fisher Scientific). The Col amount was estimated from the hydroxyproline content using the widely accepted Hyp/Col conversion factor of 7.7 [37].

Inorganic phases

The elemental composition of the extraction residues was determined using inductively coupled plasma optical emission spectrometry (*ICP-OES*) on a Liberty 200 spectrometer (Agilent Technologies 5100 ICP-OES, Santa Clara, CA, USA Varian, Palo Alto, USA). Samples preparation was achieved putting 10 mg of each powdered sample in 50 mL of 2.0 wt.% HNO_3 solution. Atomic emission of the main elements composing the samples was measured at the following wavelengths: 422.673 nm for Ca, 213.618 nm for P and 279.553 nm for Mg.

Thermal Gravimetric Analysis (*TGA*) were performed to quantify volatile and/or decomposable substances contained in the sample with a STA 449 Jupiter (Netzsch GmbH. Selb. Germany) instrument. 10.0 mg of powdered samples were heated from RT to 1100°C under air flow with a heating rate of 10°C/min in an alumina crucible.

The *FTIR-ATR* analysis was performed under the same operating conditions used for organic phases characterisation, as described in the previous chapter.

Sample morphology was evaluated with a scanning electron microscopy with a field-emission microscope (*FEG-SEM*, mod. ΣIGMA, ZEISS NTS Gmbh, Oberkochen, Germany). The preparation of powdered samples consisted of their deposition on a carbon tape mounted on an aluminium SEM stub and sputter coated (Polaron E5100, Polaron Equipment, Watford, Hertfordshire, UK) with 10 nm of gold to improve the electrical conductance. Accelerating voltage in the range between 3.0 and 5.0 keV was used to observe samples in the secondary electron imaging mode.

Finally, X-Ray Diffraction (*XRD*) analysis was performed using a DS Advance Diffractometer (Bruker), equipped with a Lynx-eye position sensitive detector, with a CuKα radiation (λ = 1.54178 Å), at 40.0 kV and 40.0 mA. XRD patterns were acquired in the 10-60° 2θ range at step size of 0.02°, and a scanning speed of 0.5 s. Phase identification was performed through Rietveld refinement using the software TOPAS5. The weight composition of the phases was refined considering a multiphase system,

using tabulated atomic coordinates of hydroxyapatite (ASTM Card file No. 00-009-0432), and β-TCP (ASTM Card file No. 00-009- 0169).

2.4. Results

Extractions with ionic liquid & deep eutectic solvent

Yields reported in Table 3 show that, although the values of organic yields and estimated Col amount are very similar among all the samples, it's interesting to note that the lower organic phase yields correspond to the higher Col content.
The inorganic phase yields, on the other hand, are very different between the samples. No trend related to increasing extraction times can be seen, but in any case, the highest yields were obtained with the extractions carried out for 5h, both with BMIM and DES.

Table 3. BMIM/DES extractions yields

	Organic yields *(Average ± SD wt.%)*	**Estimated Col amount** *(Average ± SD wt.%)*	**Inorganic yields** *(Average ± SD wt.%)*
BMIM 2.5h	0.6 ± 0.1	97 ± 10	24 ± 1
BMIM 5h	1.4 ± 0.1	86 ± 9	51 ± 5
BMIM 24h	1.8 ± 0.2	84 ± 8	39 ± 4
DES 2.5h	2.0 ± 0.3	80 ± 7	23 ± 3
DES 5h	0.7 ± 0.1	81 ± 8	72 ± 6
DES 24h	1.0 ± 0.2	82 ± 7	58 ± 5

The high viscosity of BMIM/DES made their removal after extraction very difficult, and yields may have been affected.

The FTIR-ATR spectra of both extraction residues and organic phases, reported in Figures 11 and 12, show no significant disparities between the extraction processes employing BMIM and DES. Overall, they show very poorly resolved peaks, in which the simultaneous presence of the phosphate and carbonate groups of HA and the

primary and tertiary amines of Col can be seen. These results indicate that these types of extractions are not selective, as they do not allow an optimal separation of the organic and inorganic phases.

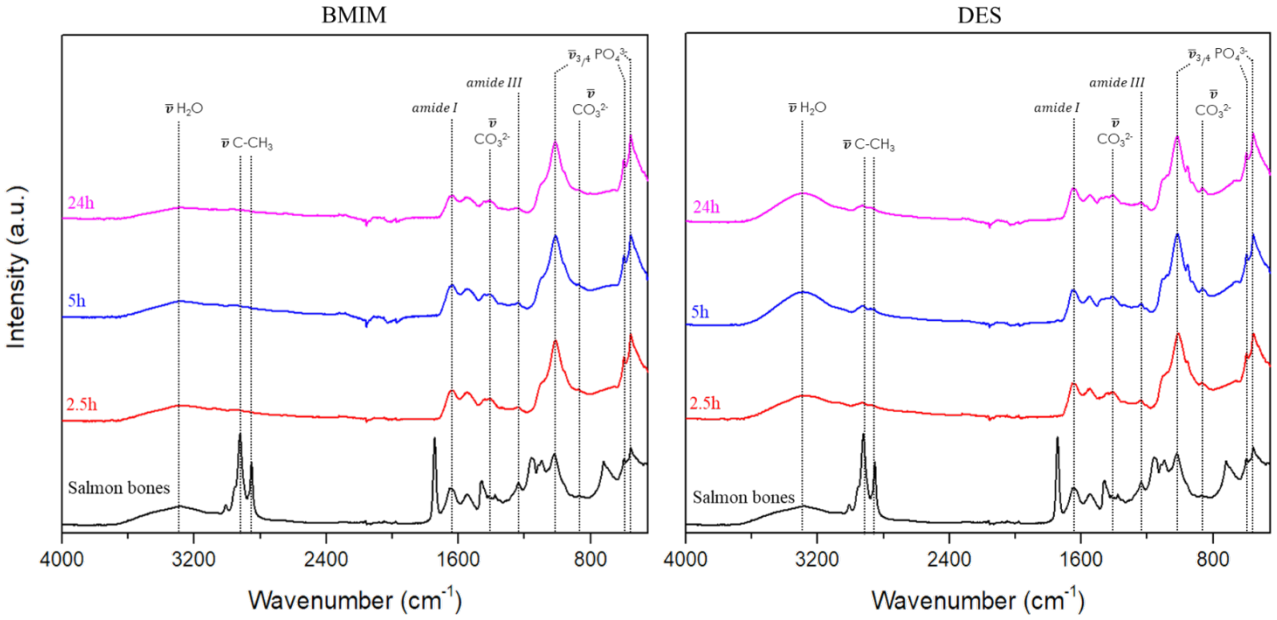

Figure 11. FTIR-ATR spectra of extraction residues obtained with BMIM (on the left) and DES (on the right) extractions at different times. Spectra

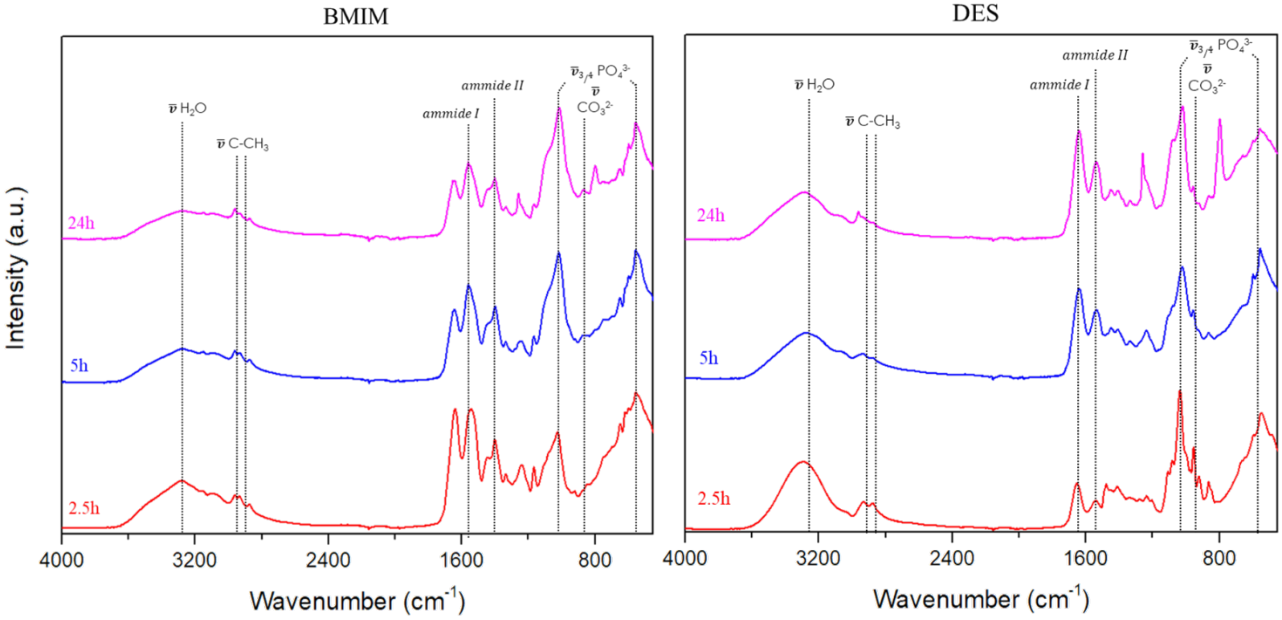

Figure 12. FTIR-ATR spectra of the organic phases obtained with BMIM (on the left) and DES (on the right) extractions at different times

The potential denaturation of the collagen triple helix was evaluated by considering the ratio between the amide III absorption peak (1235 cm^{-1}) and the 1450 cm^{-1} band corresponding to the pyrrolidine rings of the proline and hydroxyproline residues. Col is considered native when this ratio is close to 1.0, and denatured when it is around 0.5 [38], [39].

Peaks ratio results are reported in Table 4.

Table 4. 1235/1450 cm^{-1} peaks ratio of samples extracted with BMIM & DES at different times

	1235/1450 cm^{-1} peaks ratio
BMIM_2.5h	0.90
BMIM_5h	0.74
BMIM_24h	0.72
DES_2.5h	0.86
DES_5h	0.96
DES_24h	1.14

Native Col was the main form of Col in all cases, as the peaks ratio are always closer to 1.0 than to 0.5, with the exception of BMIM 5h and 24h, for which Col was probably present in both forms. For extractions with DES in particular, the peaks ratio value increases with increasing extraction time, which is the opposite trend of the extractions with BMIM.

In general, extractions with BMIM and DES proved to be complex due to the nature of the two substances, which made it difficult to separate the products and impossible to recycle the BMIM/DES. Not to mention that this makes them very difficult to use on an industrial scale. In addition, they did not give satisfactory results in terms of organic phase yields, as they were much lower than those obtained with the other extraction methods reported below in this work.

Alkaline hydrolysis

Below in the next two sections of the chapter, the physico-chemical characterisation of both organic and inorganic phases of only two samples, namely Pre_4h 60°C and 4h 60°C, are reported, as all the extracted samples showed similar results, regardless of pre-treatment, extraction time or extraction temperature.

Organic phases

The extraction yields of the organic component of salmon bones and the respective estimated Col amount are presented in Table 5.

Table 5. Alkaline hydrolysis organic yields

	Organic yields *(Average ± SD wt.%)*		**Estimated Col amount** *(Average ± SD wt.%)*	
	30°C	*60°C*	*30°C*	*60°C*
Pre_4h	5.5 ± 0.7	9.6 ± 0.3	106.3 ± 8.2	64.2 ± 32.0
Pre_24h	4.7 ± 0.9	3.4 ± 0.7	113.2 ± 5.1	113.2 ± 8.7
4h	4.3 ± 0.3	5.4 ± 0.7	112.4 ± 15.3	52.3 ± 1.2
24h	4.3 ± 0.2	4.7 ± 0.3	58.3 ± 16.1	57.2 ± 13.3

The ultrasonic pretreatment seems to slightly increase the organic yields, with values ranging from a minimum for the Pre_24h sample at 60°C to a maximum for the Pre_4h sample at 60°C. However, as with the BMIM/DES extractions, a higher yield does not necessarily correspond to a higher Col amount. The estimated Col values are generally lower for the non-pretreated samples, with the only exception being the 4h samples at 30°C, which show higher values than the corresponding pretreated ones.

Shorter extraction times were found to be a little more efficient from the point of view of the organic yield, especially for samples extracted at 60°C. In particular, the best results were obtained from the 4h extraction at 60°C with pretreatment, although the estimated amount of Col was the lowest among the pretreated samples.

With the exception of the Pre_4h 60°C sample, for which the highest yield values were obtained, temperature does not seem to have an influence on the extraction of the organic phases, returning similar values between the pretreated and non-pretreated samples. However, higher temperatures appear to have a significant impact on the estimated Col amount, with extractions at 60°C yielding the lowest values, especially for the not-pretreated samples. Notably, the 24h extractions appear to be less susceptible to temperature influence, exhibiting comparable results at both 30°C and 60°C.

It was therefore not possible to identify a specific relationship between the yields values obtained and the extraction parameters (pretreatment, temperature and extraction time). For this reason, the DoE approach was used, the results of which are given at the end of this subchapter.

The FTIR-ATR spectra in Figure 13 are indicative of the extraction of the organic phase, with peaks related to the stretching of the C=O group of amide I visible at approximately 1644 cm^{-1}, and peaks of the stretching and bending of the C-N and N-H groups of amide III visible at around 1237 cm^{-1}. However, as for the extractions with BMIM/DES, the presence of peaks attributable to the phosphate and carbonate groups of HA is also evident, indicating the occurrence of this phase in the extract.

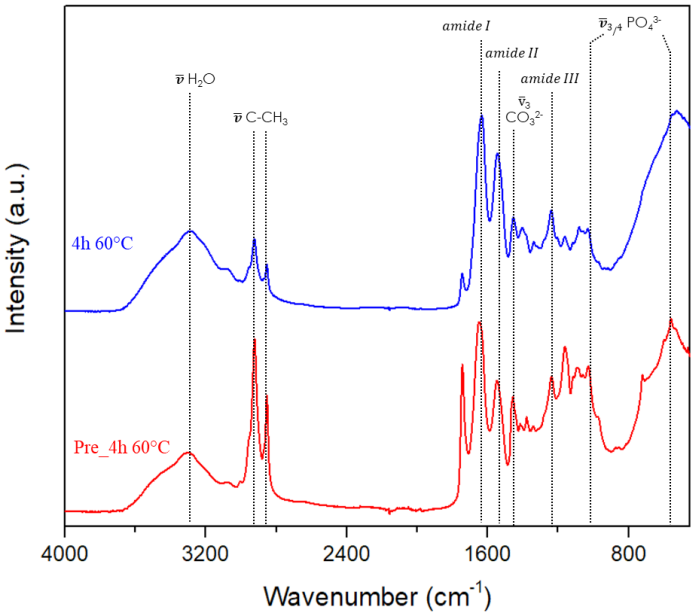

Figure 13. FTIR-ATR spectra of organic phases extracted by alkaline hydrolysis

Peaks ratio results are reported in Table 6.

Table 6. 1235/1450 cm^{-1} peaks ratio of samples extracted with alkaline hydrolysis

	1235/1450 cm^{-1} peaks ratio	
	30°C	*60°C*
Pre_4h	1.17	1.22
Pre_24h	1.05	1.11
4h	1.11	1.07
24h	1.04	0.98

In all samples, the extracted Col was found to be in the native form. In this case, the extraction parameters had no significant impact on the eventual degradation of the extracted collagen, even more so than on the extraction yields.

Inorganic phases

Table 7 shows the inorganic phase yields, obtained after calcination of the extraction residues.

Table 7. Alkaline hydrolysis inorganic yields

	Inorganic yields *(Average ± SD wt.%)*	
	30°C	*60°C*
Unextracted bones	34.0 ± 2.1	
Pre_4h	27.3 ± 0.4	25.4 ± 0.9
Pre_24h	26.2 ± 0.8	24.1 ± 0.1
4h	27.8 ± 0.7	26.1 ± 1.0
24h	27.1 ± 0.7	24.3 ± 0.5

Values obtained for the extracted samples were found to be slightly lower than those obtained for the unextracted bones, yet they are extremely similar to each other, varying only between 24.1 ± 0.1 wt.% and 27.8 ± 0.7 wt.%. In this case therefore, even more than for organic yields, the extraction parameters do not seem to have an influence on the yields obtained.

In particular, pretreatment has even less relevance, while extractions conducted over 24h returned slightly lower inorganic yield values than shorter extractions, probably as a consequence of the higher dissolution of pristine HA with longer extraction times. Furthermore, higher temperatures have been observed to decrease the yield values, in comparison to extractions conducted at 30°C.

As showed in Figure 14, the FTIR-ATR spectra of the extraction residues are not significantly different from those obtained for the organic phases.

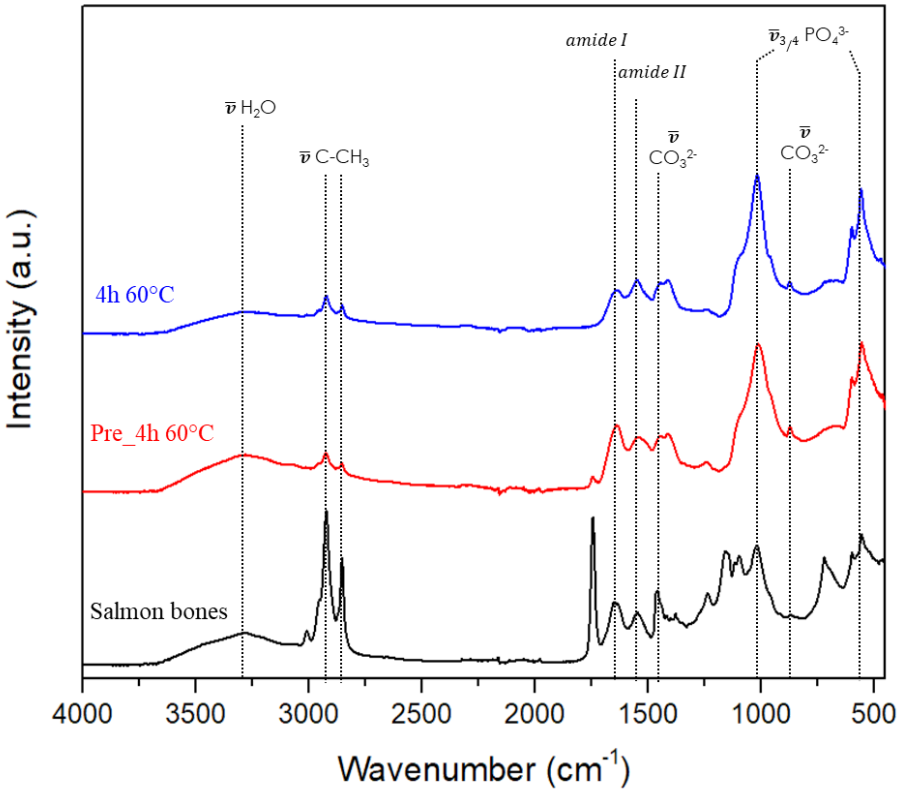

Figure 14. FTIR-ATR spectra of extraction residues obtained by alkaline hydrolysis

The most abundant peaks are those corresponding to the stretching and bending of the carbonate (around 1452 and 854 cm^{-1}) and phosphate (1016 and 558 cm^{-1}) groups of the HA. In particular, these peaks appear more resolved than those of the unextracted bones, which obviously still contain abundant amounts of organic phase. However, even in the extracted samples, peaks for the vibrational modes of Col amines I and III are respectively present at around 1631 and 1237 cm^{-1}, again indicating the incomplete selectivity of these extractions.

Thermogravimetric analysis graph reported in Figure 15 has shown that unextracted salmon bones (the pristine material) consist of:

- 6.15% highly volatile compounds, which decompose between 0-200°C.
- 52.43% organic material, broken down into 30.98% fat, which decomposes between 200-400°C, and 21.45% protein, which decomposes between 400-600°C.
- 41.42% inorganic residue.

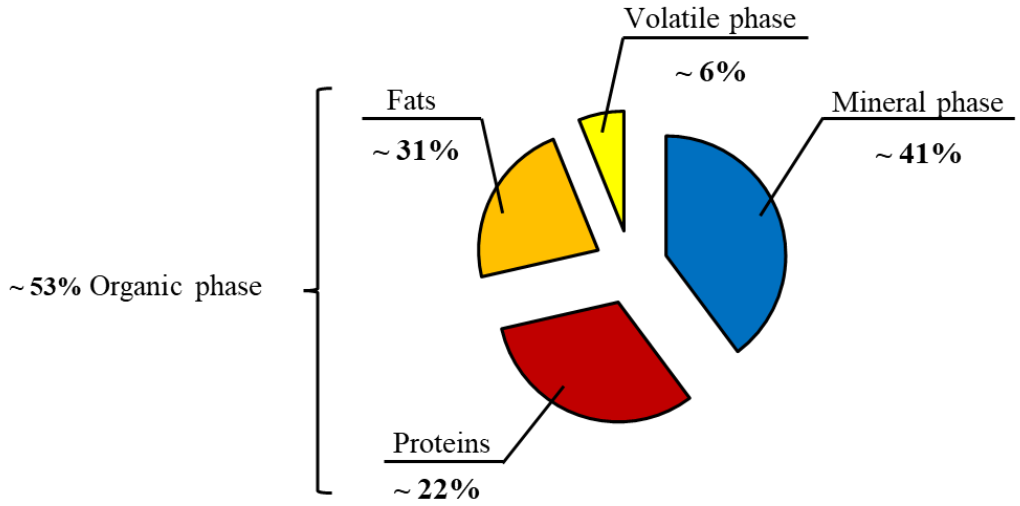

Figure 6. TGA analysis results of unextracted salmon bones

The results obtained for unextracted bones and samples are summarised in Table 8. Extraction residues show less organic material but more inorganic phase, compared to the pristine bones. This is to be expected as a sensible portion of the organic fraction of salmon bones was removed during the extraction process.

Table 8. Wt.% lost from alkaline hydrolysis extraction residues during TGA analysis

	0-200°C	**200-400°C**	**400-600°C**	**Residual part**
Unextracted bones	6.15%	52.43%	21.45%	41.42%
Pre_4h 60°C	6.33%	25.16%		68.51%
4h 60°C	4.65%	23.85%		71.50%

The elemental composition of the inorganic phase obtained by calcination from the extracted samples and unextracted salmon bones is presented in Table 9.

Table 9. Elemental composition of salmon unextracted bones and extracted samples

	Unextracted bones	*Pre_4h 60°C*	*4h 60°C*
Ca *(Average ± SD wt.%)*	34.94 ± 0.61	34.14 ± 1.74	37.30 ± 0.83
P *(Average ± SD wt.%)*	18.08 ± 0.31	17.87 ± 0.81	18.18 ± 0.85
Al *(Average ± SD wt.%)*	0.03 ± 0.01	0.01 ± 0.01	0.03 ± 0.00
Mg *(Average ± SD wt.%)*	0.56 ± 0.03	0.55 ± 0.03	0.55 ± 0.01
Mn *(Average ± SD wt.%)*	0.02 ± 0.00	0.01 ± 0.00	0.02 ± 0.00
Sr *(Average ± SD wt.%)*	0.14 ± 0.00	0.15 ± 0.03	0.15 ± 0.01
Zn *(Average ± SD wt.%)*	0.06 ± 0.00	0.02 ± 0.01	0.06 ± 0.00
Ca/P *(mol/mol ± SD)*	1.47 ± 0.00	1.48 ± 0.01	1.56 ± 0.01
Cations/P *(mol/mol ± SD)*	1.52 ± 0.00	1.52 ± 0.02	1.61 ± 0.08

Calcined powders are mainly composed of Ca and P, as might be expected. However, other trace elements are also present, mainly Al, Mg, Mn, Sr and Zn. It's interesting to note that these elements are present in similar quantities in both the samples and the unextracted bones. The main difference is the Ca content, which is much higher in the non-pretreated sample. This results in a higher Ca/P ratio, which is closer to the

stoichiometric ratio of 1.67. The same results were obtained for all the other samples extracted by alkaline hydrolysis at different times.

The patterns illustrating the mineral composition of the inorganic phase obtained by XRD analysis are shown in Figure 16:

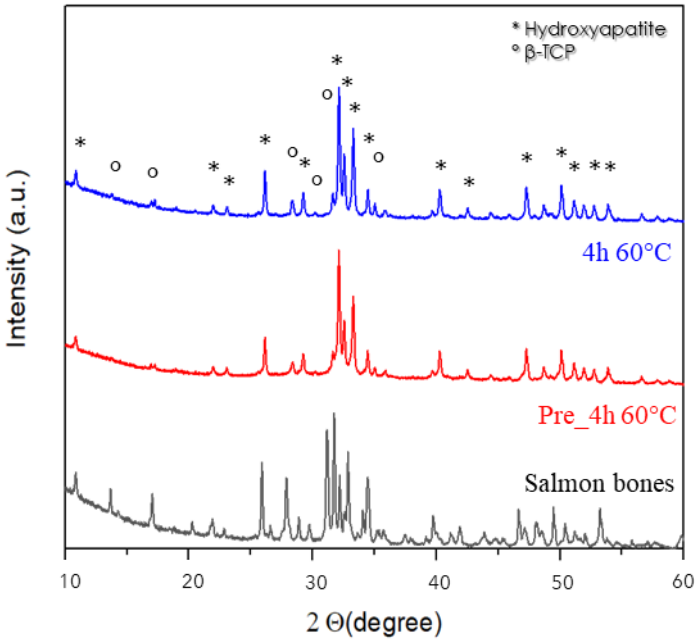

Figure 7. XRD patterns of mineral phases obtained by alkaline hydrolysis

XRD patterns of both the extracted samples and the unextracted salmon bones after calcination show a biphasic composition. In addition to HA, another calcium phosphate, beta-tricalcium phosphate (β-TCP), is also present, as a consequence of calcination. In fact, these patterns are typically obtained from the calcination of bones, which, being of biogenic origin contain foreign elements that deviates bones' Ca/P ratio from that of HA stoichiometric value, leading to the phase separation of part of the HA (ASTM Card file No. 00-009-0432) into β-TCP (ASTM Card file No. 00-009- 0169).

The percentage composition of the two phases, shown in Table 10, has been calculated using Rietveld refinement and indicates that the unextracted bones are mainly composed of HA, whereas after extraction, the samples exhibit an increase in HA content and a decrease in β-TCP content. In particular, the non-pretreated sample appears to have a slightly lower β-TCP content than the pretreated one, probably due

to a difference in chemical composition, especially based on the Ca/P ratio of the material prior to calcination.

Table 10. Rietveld analysis of mineral phases obtained by alkaline hydrolysis

	HA *(Average ± SD wt.%)*	**β-TCP** *(Average ± SD wt.%)*
Unextracted bones	43.7 ± 0.3	56.3 ± 0.3
Pre_4h 60°C	92.8 ± 0.4	7.2 ± 0.4
4h 60°C	88.6 ± 0.3	11.4 ± 0.3

The electron microscopy collected by SEM of unextracted calcined salmon bones, shown in Figure 17, show that the sample contains particles with mixed morphology, consisting of small round-shaped particles and larger hexagonal rods.

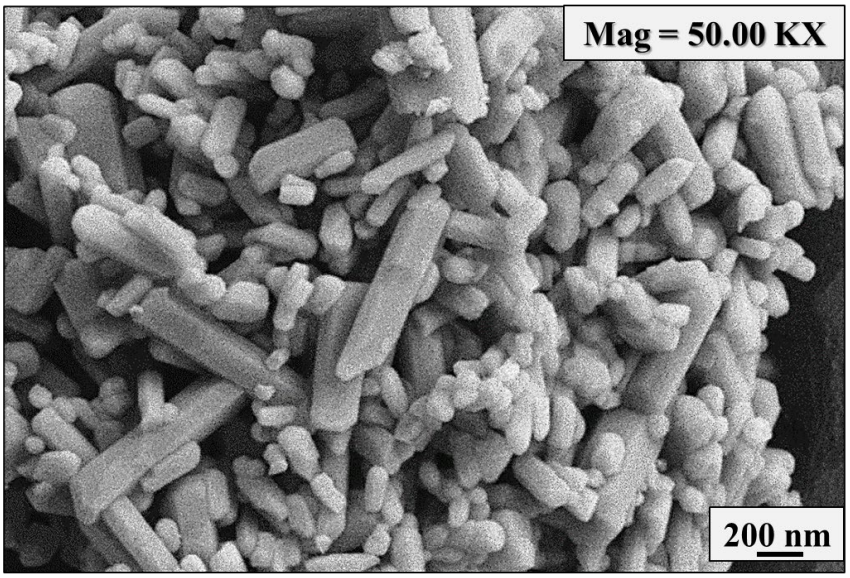

Figure 8. SEM-FEG image of calcined (unextracted) salmon bones

After the extraction process, the morphology of the samples changes significantly, as can be seen in Figure 18.

The two different particles morphology are no longer distinguishable, with the powder exhibiting only spherical, nanometric particles. In the sample extracted without pretreatment, the same morphologies of the particles can be observed.

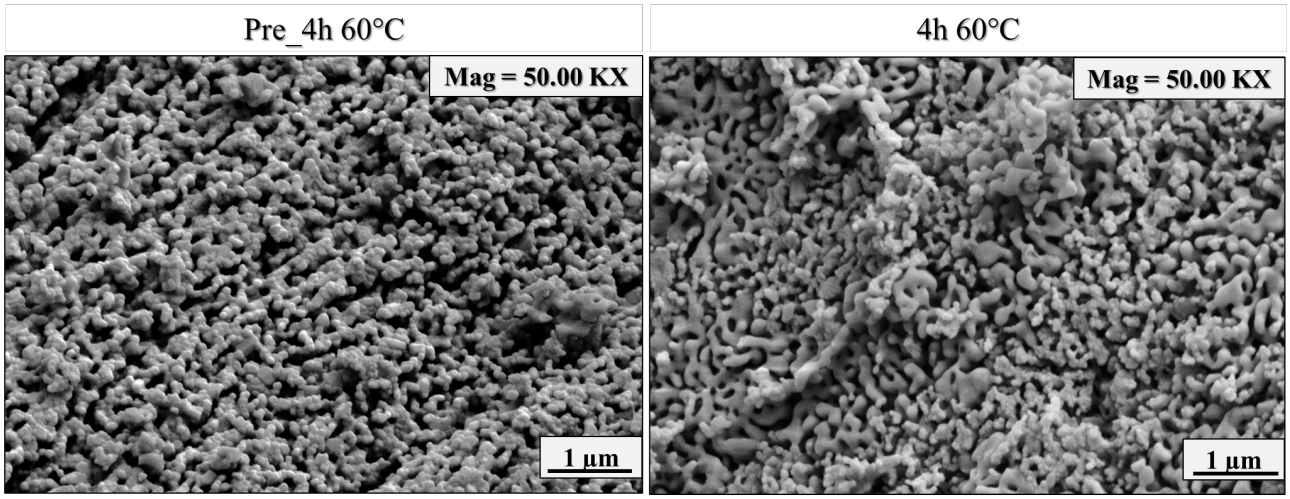

Figure 9. SEM-FEG images of extracted samples at 60°C for 4h with (on the left) and without (on the right) pretreatment

DoE 3x2

The DoE 3x2 approach made it possible to determine the optimal conditions for obtaining the best results, so as to maximise the inorganic yields, the organic yields and the estimated Col amount at the same time. The results presented in Table 11 show that the pretreatment influences both the organic yield and the estimated amount of Col. The optimal temperature for conducting the experiment was found to be 45°C, which is intermediate between the two extraction temperatures employed. Finally, the 4h extraction time is the best compromise compared to the extraction performed over a longer period of time.

Table 11. optimal extraction conditions obtained by DoE 3x2

Pretreatment	Extraction time	Extraction temperature
Yes	4h	45°C

Enzymatic extractions

Organic and inorganic yields obtained for the three enzymatic extractions are reported in Table 12.

Table 12. Organic & inorganic enzymatic extractions yields

	Organic yields *(Average ± SD wt.%)*	**Estimated Col amount** *(Average ± SD wt.%)*	**Inorganic yields** *(Average ± SD wt.%)*
CTRL	6.4 ± 0.6	96.7 ± 2.8	26 ± 3
Trypsin	17.5 ± 1.6	90.9 ± 10.2	23 ± 2
CTRL	3.4 ± 0.3	56.8 ± 2.9	25 ± 2
Papain	4.1 ± 0.5	51.5 ± 0.6	22 ± 2
CTRL	1.7 ± 0.2	11.0 ± 0.9	20 ± 3
Pepsin	1.5 ± 0.3	15.5 ± 0.5	20 ± 3

The yield values obtained, especially the inorganic ones, and the estimated Col amount for the samples extracted with the enzymes are comparable with those obtained for the respective controls. The only exception is the sample extracted with trypsin, for which the organic yield values are almost three times as high as for the control. The inorganic yields are slightly lower than those obtained for the samples extracted with pepsin, but comparable to those obtained for the sample extracted with papain, which shares the extraction protocol.

Overall, trypsin extraction was found to be the most efficient extraction method for both organic yields and Col content, which was significantly higher than that obtained with the other enzymes.

The inorganic and organic FTIR-ATR spectra of the enzyme extracts shown in Figures 19 and 20 highlight that there are no differences in extraction capacity between the enzyme-extracted samples and their respective controls.

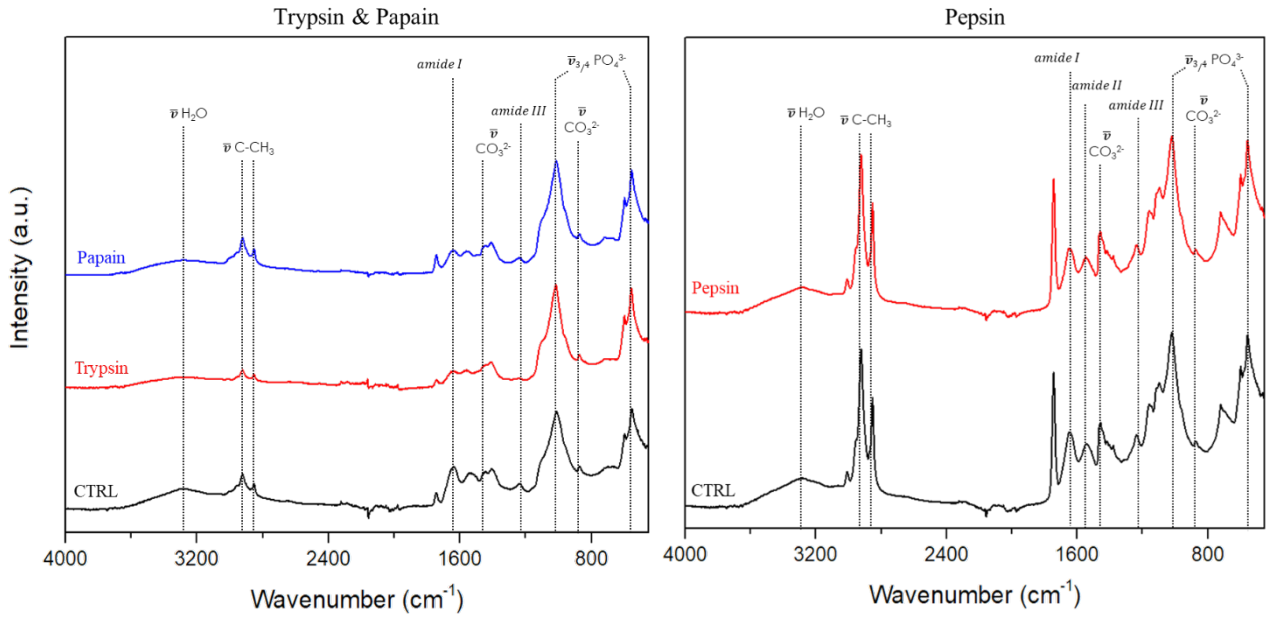

Figure 10. FTIR-ATR spectra of extraction residues of enzymatic extractions. Trypsin and papain, on the left, and pepsin on the right

The extraction residues, in addition to the typical peaks of the phosphate and carbonate groups, exhibit peaks corresponding to the amides I, II and III of Col, although they are slightly less pronounced in the samples extracted with trypsin and papain than in the control and in the pepsin extraction.

Spectra of the organic phases obtained from the trypsin and papain extractions show, once again, no particular differences between them or with the control.

In addition to the characteristic peaks of Col, the simultaneous presence of phosphate and carbonate groups of CaP is evident. However, pepsin extraction is the only one that shows a difference between the sample and the control, having the peak of the phosphate group stretching at 1078 cm^{-1} less intense and the peaks of amines I, II and

III more intense.

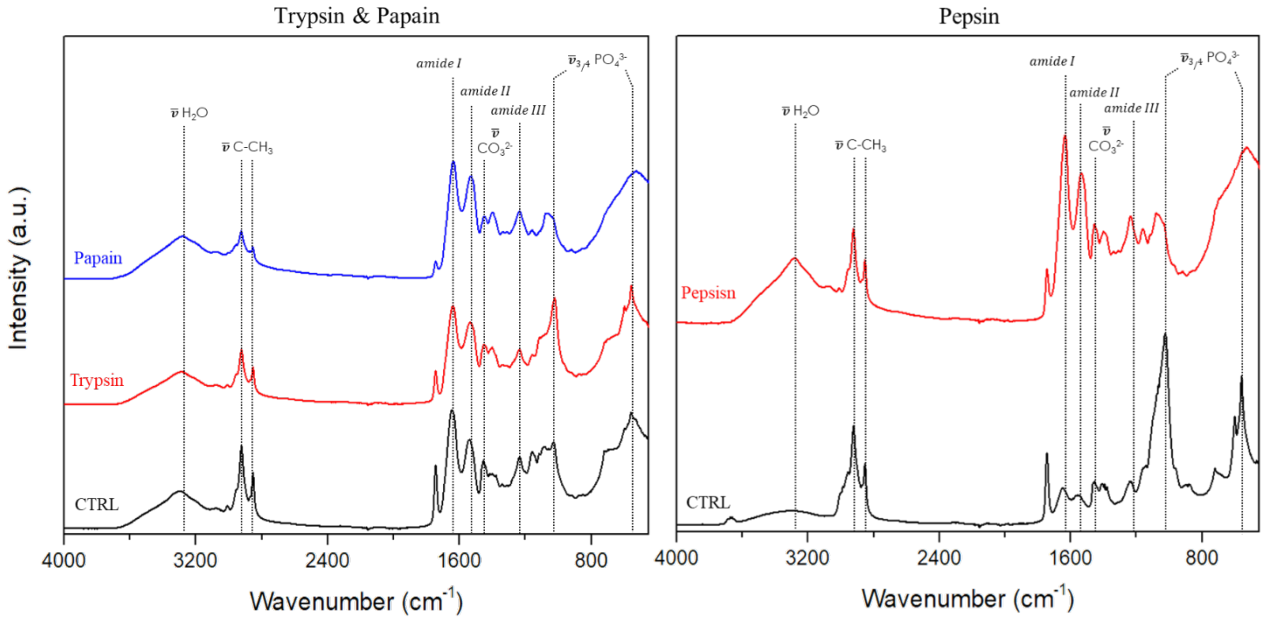

Figure 20. FTIR-ATR spectra of organic phases of enzymatic extractions. Trypsin and papain, on the left, and pepsin on the right.

Peaks ratio results are reported in Table 13.

Table 13. 1235/1450 cm^{-1} peaks ratio of samples extracted with enzymatic extractions

	1235/1450 cm^{-1} peaks ratio
CTRL	1.08
Trypsin	0.93
CTRL	1.14
Papain	1.07
CTRL	1.10
Pepsin	1.09

All extractions, regardless of the presence and type of enzyme, turned a 1235/1450 cm^{-1} peaks ratio values close to 1, indicating that native Col was obtained.

2.5. Conclusions

Salmon bones, a by-product of the fishing industry, were utilized as raw material to simultaneously obtain hydroxyapatite (HA) and collagen (Col) using innovative extraction protocols. Three extraction methods, namely BMIM/DES, alkaline hydrolysis and enzymatic hydrolysis, were employed.

The BMIM/DES method did not yield satisfactory results in terms of efficiency, selectivity, or scalability for industrial applications.

Subsequently, alkaline hydrolysis was performed at 30°C and 60°C for durations of 4 or 24h. Ultrasound pretreatment was also applied to evaluate its influence on the process. While the organic extraction was not entirely selective, the inorganic yields were comparable to those of unextracted bones, with no significant differences observed across samples extracted at varying temperatures or times. Estimated Col content was notably higher in ultrasound-pretreated samples, particularly those extracted at 60°C. However, the pretreatment did not significantly influence organic yields except for samples extracted at 60°C for shorter durations, which exhibited slightly higher values.

To enhance organic yields, a Design of Experiments (DoE) approach was employed to evaluate the impact of various extraction parameters. The results indicated that ultrasound pre-treatment followed by extraction at 45°C for 4h provided the most promising outcomes in terms of yields and purity of the extract.

Enzymatic extractions have been carried out using trypsin, papain, and pepsin, each operating at their respective optimal pH values of 8.2, 7.0, and 5.6. The presence of enzymes did not appear to affect inorganic yields. Also, the organic yields from papain and pepsin extractions showed no difference compared to the respective controls (same extraction conditions but without the enzymes). However, trypsin extraction yielded almost three times the organic content relative to the control and demonstrated high estimated Col content.

All the extractions yielded native Col, and the calcined materials proved not to contain elements potentially harmful to human health or the environment, thus proving their suitability for cosmetic and environmental purposes.

References

[1] J. Banothu, R. Gali, R. Velpula, and R. Bavantula, "Brønsted acidic ionic liquid catalyzed an efficient and eco-friendly protocol for the synthesis of 2,4,5-trisubstituted-1H-imidazoles under solvent-free conditions," *Arabian Journal of Chemistry*, vol. 10, pp. S2754–S2761, May 2017, doi: 10.1016/j.arabjc.2013.10.022.

[2] S. Yasuda, H. Svergja, C. E. Olsen, and B. H. Hoff, "Promotion of Water as Solvent in Amination of 4-Chloropyrrolopyrimidines and Related Heterocycles under Acidic Conditions," *ACS Omega*, vol. 9, no. 12, pp. 14142–14152, Mar. 2024, doi: 10.1021/acsomega.3c09673.

[3] M. Suljkanović, J. Suljagić, E. Bjelić, A. Prkić, and P. Bošković, "Chemical Characterization of Terpene-Based Hydrophobic Eutectic Solvents and Their Application for Pb(II) Complexation during Solvent Extraction Procedure," *Molecules*, vol. 29, no. 9, May 2024, doi: 10.3390/molecules29092122.

[4] H. Y. Lim and A. V. Dolzhenko, "Gluconic acid aqueous solution: A bio-based catalytic medium for organic synthesis," Jun. 01, 2021, *Elsevier B.V.* doi: 10.1016/j.scp.2021.100443.

[5] Z. T. Tsegay, S. Agriopoulou, M. Chaari, S. Smaoui, and T. Varzakas, "Statistical Tools to Optimize the Recovery of Bioactive Compounds from Marine Byproducts," Apr. 01, 2024, *Multidisciplinary Digital Publishing Institute (MDPI)*. doi: 10.3390/md22040182.

[6] C. Piccirillo, R. C. Pullar, E. Costa, A. Santos-Silva, M. M. E. Pintado, and P. M. L. Castro, "Hydroxyapatite-based materials of marine origin: A bioactivity and sintering study," *Materials Science and Engineering C*, vol. 51, pp. 309–315, Jun. 2015, doi: 10.1016/j.msec.2015.03.020.

[7] F. Ling Wen Xia *et al.*, “Turning waste into value: Extraction and effective valorization strategies of seafood by-products,” *Waste Management Bulletin*, vol. 2, no. 3, pp. 84–100, Sep. 2024, doi: 10.1016/j.wmb.2024.06.008.

[8] H. Jafari *et al.*, “Fish collagen: Extraction, characterization, and applications for biomaterials engineering,” Oct. 01, 2020, *MDPI AG*. doi: 10.3390/polym12102230.

[9] S. Gaikwad and M. J. Kim, “Fish By-Product Collagen Extraction Using Different Methods and Their Application,” Feb. 01, 2024, *Multidisciplinary Digital Publishing Institute (MDPI)*. doi: 10.3390/md22020060.

[10] P. Belibagli, Z. Isik, M. A. Mazmanci, and N. Dizge, “Phosphate recovery from waste fish bones ash by acidic leaching method and iron phosphate production using electrocoagulation method,” *J Clean Prod*, vol. 373, Nov. 2022, doi: 10.1016/j.jclepro.2022.133499.

[11] J. Swart, A. Bordoloi, and N. J. Goosen, “Optimization of phosphate recovery from monkfish, Lophius vomerinus, processing by-products and characterization of the phosphate phases,” *J Sci Food Agric*, vol. 99, no. 6, pp. 2743–2756, Apr. 2019, doi: 10.1002/jsfa.9450.

[12] K. Sockalingam, H. Z. Abdullah, and M. I. Idris, “Effects of Acid Pre-Treatment on Removal of Organic and Inorganic Substances from Black Tilapia Bones and Scales,” *International Journal of Integrated Engineering*, vol. 16, no. 5, pp. 26–33, 2024, doi: 10.30880/ijie.2024.16.05.003.

[13] R. P. Swatloski, S. K. Spear, J. D. Holbrey, and R. D. Rogers, “Dissolution of cellose with ionic liquids,” *J Am Chem Soc*, vol. 124, no. 18, pp. 4974–4975, May 2002, doi: 10.1021/ja025790m.

[14] Z. Meng, X. Zheng, K. Tang, J. Liu, Z. Ma, and Q. Zhao, “Dissolution and regeneration of collagen fibers using ionic liquid,” *Int J Biol Macromol*, vol. 51, no. 4, pp. 440–448, 2012, doi: 10.1016/j.ijbiomac.2012.05.030.

[15] S. Pandey, “Analytical applications of room-temperature ionic liquids: A review of recent efforts,” Jan. 18, 2006. doi: 10.1016/j.aca.2005.06.038.

[16] N. Muhammad *et al.*, “Extraction of biocompatible hydroxyapatite from fish scales using novel approach of ionic liquid pretreatment,” *Sep Purif Technol*, vol. 161, pp. 129–135, Mar. 2016, doi: 10.1016/j.seppur.2016.01.047.

[17] H. Zhu, W. Song, and Y. Deng, “Hydroxyapatite extracted by animal bone image analysis in ionic liquid choline chloride-glycerol,” *EURASIP J Image Video Process*, vol. 2018, no. 1, Dec. 2018, doi: 10.1186/s13640-018-0295-5.

[18] C. Samorì, “Use of solvents and environmental friendly materials for applications in Green Chemistry,” Alma Mater Studiorum-Università di Bologna.

[19] P. A. Hunt, B. Kirchner, and T. Welton, “Characterising the electronic structure of ionic liquids: An examination of the 1-butyl-3-methylimidazolium chloride ion pair,” *Chemistry - A European Journal*, vol. 12, no. 26, pp. 6762–6775, Sep. 2006, doi: 10.1002/chem.200600103.

[20] H. Vanda, Y. Dai, E. G. Wilson, R. Verpoorte, and Y. H. Choi, “Green solvents from ionic liquids and deep eutectic solvents to natural deep eutectic solvents,” *Comptes Rendus Chimie*, vol. 21, no. 6, pp. 628–638, Jun. 2018, doi: 10.1016/j.crci.2018.04.002.

[21] I. Wazeer, M. Hayyan, and M. K. Hadj-Kali, “Deep eutectic solvents: designer fluids for chemical processes,” Apr. 01, 2018, *John Wiley and Sons Ltd*. doi: 10.1002/jctb.5491.

[22] H. Zhu, W. Song, and Y. Deng, “Hydroxyapatite extracted by animal bone image analysis in ionic liquid choline chloride-glycerol,” *EURASIP J Image Video Process*, vol. 2018, no. 1, Dec. 2018, doi: 10.1186/s13640-018-0295-5.

[23] G. A. Ojeda, M. M. Vallejos, S. C. Sgroppo, C. Sánchez-Moreno, and B. de Ancos, “Enhanced extraction of phenolic compounds from mango by-products

using deep eutectic solvents," *Heliyon*, vol. 9, no. 6, Jun. 2023, doi: 10.1016/j.heliyon.2023.e16912.

[24] C. B. T. Pal and G. C. Jadeja, "Deep eutectic solvent-based extraction of polyphenolic antioxidants from onion (Allium cepa L.) peel," *J Sci Food Agric*, vol. 99, no. 4, pp. 1969–1979, Mar. 2019, doi: 10.1002/jsfa.9395.

[25] Y. Liu *et al.*, "Enhanced extraction of hydroxyapatite from bighead carp (Aristichthys nobilis) scales using deep eutectic solvent," *J Food Sci*, vol. 85, no. 1, pp. 150–156, Jan. 2020, doi: 10.1111/1750-3841.14971.

[26] G. B. Smejkal and S. Kakumanu, "Safely meeting global salmon demand," 2018, *Nature Research*. doi: 10.1038/S41538-018-0025-5.

[27] L. Kantor, "Americans' Seafood Consumption Below Recommendations," 2016.

[28] L. Sun, H. Hou, B. Li, and Y. Zhang, "Characterization of acid- and pepsin-soluble collagen extracted from the skin of Nile tilapia (Oreochromis niloticus)," *Int J Biol Macromol*, vol. 99, pp. 8–14, Jun. 2017, doi: 10.1016/j.ijbiomac.2017.02.057.

[29] Y. Pranoto, C. M. Lee, and H. J. Park, "Characterizations of fish gelatin films added with gellan and κ-carrageenan," *LWT*, vol. 40, no. 5, pp. 766–774, 2007, doi: 10.1016/j.lwt.2006.04.005.

[30] J. N. Zeng, B. Q. Jiang, Z. Q. Xiao, and S. H. Li, "Extraction of collagen from fish scales with papain under ultrasonic pretreatment," in *Advanced Materials Research*, 2012, pp. 421–424. doi: 10.4028/www.scientific.net/AMR.366.421.

[31] G. He, X. Yan, X. Wang, and Y. Wang, "Extraction and structural characterization of collagen from fishbone by high intensity pulsed electric fields," *J Food Process Eng*, vol. 42, no. 6, Oct. 2019, doi: 10.1111/jfpe.13214.

[32] P. Terzioğlu, H. Öğüt, and A. Kalemtaş, “Natural calcium phosphates from fish bones and their potential biomedical applications,” Oct. 01, 2018, *Elsevier Ltd*. doi: 10.1016/j.msec.2018.06.010.

[33] M. M. Schmidt *et al.*, “Collagen extraction process,” 2016.

[34] C. Sendrea, C. Carsote, E. Badea, and A. Adams, “Non-invasive characterisation of collagen-based materials by NMR-MOUSE and ATR-FTIR,” *Bull., Series B*, vol. 78, no. 3, 2016.

[35] A. Adamiano *et al.*, “Simultaneous extraction of calcium phosphates and proteins from fish bones. Innovative valorisation of food by-products,” *J Clean Prod*, vol. 385, Jan. 2023, doi: 10.1016/j.jclepro.2022.135656.

[36] D. D. Cissell, J. M. Link, J. C. Hu, and K. A. Athanasiou, “A Modified Hydroxyproline Assay Based on Hydrochloric Acid in Ehrlich’s Solution Accurately Measures Tissue Collagen Content,” *Tissue Eng Part C Methods*, vol. 23, no. 4, pp. 243–250, Apr. 2017, doi: 10.1089/ten.tec.2017.0018.

[37] A. A. Jaziri, R. Shapawi, R. A. M. Mokhtar, W. N. M. Noordin, and N. Huda, “Biochemical and Microstructural Properties of Lizardfish (Saurida tumbil) Scale Collagen Extracted with Various Organic Acids,” *Gels*, vol. 8, no. 5, May 2022, doi: 10.3390/gels8050266.

[38] A. George and A. Veis, “FTIRS in H20 Demonstrates That Collagen Monomers Undergo a Conformational Transition Prior to Thermal Self-Assembly in Vitro1",” UTC, 1991. [Online]. Available: https://pubs.acs.org/sharingguidelines

[39] C. Sendrea, C. Carsote, E. Badea, and A. Adams, “Non-invasive characterisation of collagen-based materials by NMR-mouse and ATR-FTIR,” *Bull., Series B*, vol. 78, no. 3, 2016.

CHAPTER III: SUN CARE

3.1. Introduction

Sunscreens are designed to protect our skin from the negative effects of the sun's UV radiations (UVR). In particular, they provide protection against UVB and UVA radiations, as UVC rays do not reach the Earth's surface and are shielded by the atmosphere.

The protective power of sunscreens is due to the UV filters contained in their formulations, which are substances able to reflect, absorb and/or disperse radiation. They can be divided into two categories:

- *organic* (or chemical) filters, which are capable of absorbing UVR.
- *inorganic* (or physical) filters, which are capable of absorbing, reflecting or dispersing incident UVR.

Both types of UV filters can cause several problems for human health and the environment [1], [2], [3], [4].

From an environmental perspective, the most significant problem is the bleaching of coral reefs. The presence of UV filters in solar products can damage coral organisms by producing reactive oxygen species (ROS) and impairing their biological functions. It's estimated that between 6000 and 14000 tons of solar products are leaked into coral reef areas each year, posing a significant threat to at least 40% of coral reefs along coastal areas around the world [5], [6]. In fact, water pollution from UV filters is well documented and is very difficult to remove with conventional treatments.

From the human health perspective, *organic filters* can penetrate the skin and the bloodstream, causing photoallergy, phototoxic reactions and skin irritation [7].

The use of *inorganic filters* is typically regarded as a more secure alternative, especially when they are in the micrometric size range; however, they present some minor shortcoming for final users. As an example, the use of micrometric inorganic filters

results in a white discolouration of the skin, due to their high refractive index, which reduces the aesthetic value of sunscreens [8]. To enhance the texture and therefore the spreadability of creams and avoid the so-called “whitening effect” of sun cream, inorganic filters are employed in the form of nanoparticles. If on one hand this solve a technical problem, on the other hand it poses a risk for consumers’ safety, as it has been hypothesized that these nanoparticles can penetrate the skin – especially the damaged one – causing allergies or skin irritation [9], [10].

The REACH in the EU and the US Food and Drug Administration (FDA) only allow the use of two types of inorganic UV filters, titanium dioxide (TiO_2) and zinc oxide (ZnO), despite their ability to generate free radicals or other reactive species when in a nanometric form, which may result in skin damage or long-term disease [11]. The increasing awareness of the risks of sun exposure and the risks associated with the use of sunscreens has therefore led to a paradoxical need: to formulate products with a high Sun Protection Factor (SPF) while reducing the concentration of UV filters [12].

Organics & inorganic UV filters employed

Organic filters are aromatic molecules, which often have a conjugated carbonyl group, that can absorb the UVR. Since absorption is related to specific energy values, each filter works in a characteristic wavelength range and has a specific maximum of absorption peak.

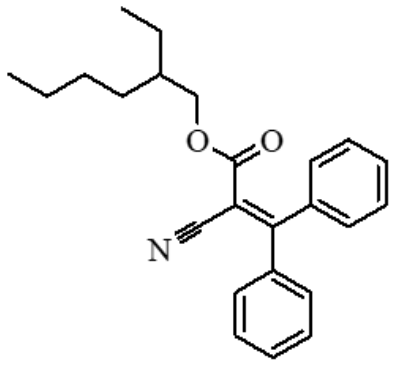

Figure 21. OCR chemical structure

Octocrylene (OCR, IUPAC: 2-cyano-3,3-diphenyl acrylic acid 2-ethylhexyl ester; Figure 21) is an organic UVB filter with a maximum absorption at 303 nm [12]. It's one of the most widely used UVB filters worldwide, as it is photostable and acts as a quencher in the presence of Avobenzone, stabilising it and providing broad spectrum UV photoprotection.

It is a photostable molecule, which makes it very useful in sun formulations, but can lead to bioaccumulation in the environment and aquatic species, due to its low water solubility and non-biodegradability.

The maximum concentration that can be used in sunscreen formulations set by the EU is 10% w/w [13].

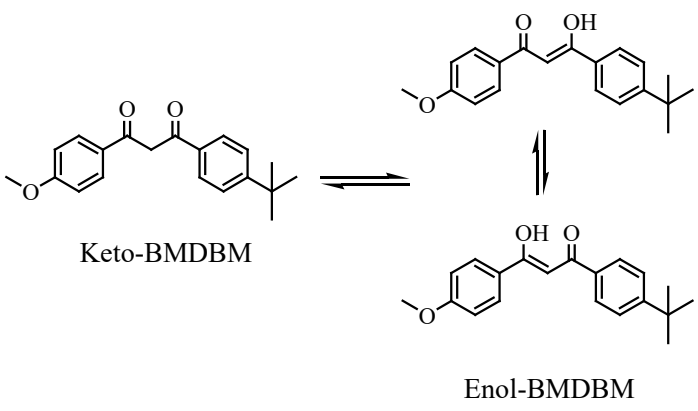

Figure 211. Tautomers of BMDBM: keto-form (sx) and enol-form (dx) [34]

Avobenzone (BMDBM, 3-(4-tert-butylphenyl)-1-(4-methoxyphenyl) propane-1,3-dione) is an organic UVA filter and is the only uniformly approved UVA filter worldwide [14]. Figure 22 shows the two tautomeric forms in which it can be found; however, only the enol form is capable of absorbing UVA radiation.Unfortunately, when subjected to photoexcitation, tautomerisation can occur

and part of the enol-BMDBM is converted into keto-BMDBM, which is ineffective for skin protection.

In the environment, it does not bioaccumulate and does not exhibit endocrine-disrupting activity in aquatic organisms, although it may reduce the mobility and growth of some species [15]. The maximum concentration that can be used in sunscreen formulations set by the EU is 5% w/w.

ZnO is a metal oxide with a high refractive index that can diffuse, reflect and absorb UVA rays. It is considered the safest UV filter as it presents a lower risk profile than both organic ones and TiO_2. As illustrated in Figure 23, the skin is made up of several layers through which various substances enter our bodies. In vitro and in vivo human studies have shown that nanometre-sized ZnO can penetrate the epidermis, the surface layer of the skin, but is unable to penetrate the dermis, the layer below. The whitening effect is less than that of TiO_2 and the environmental risk of ZnO nanoparticles is also considered to be very low, although knowledge is still limited [16], [17].

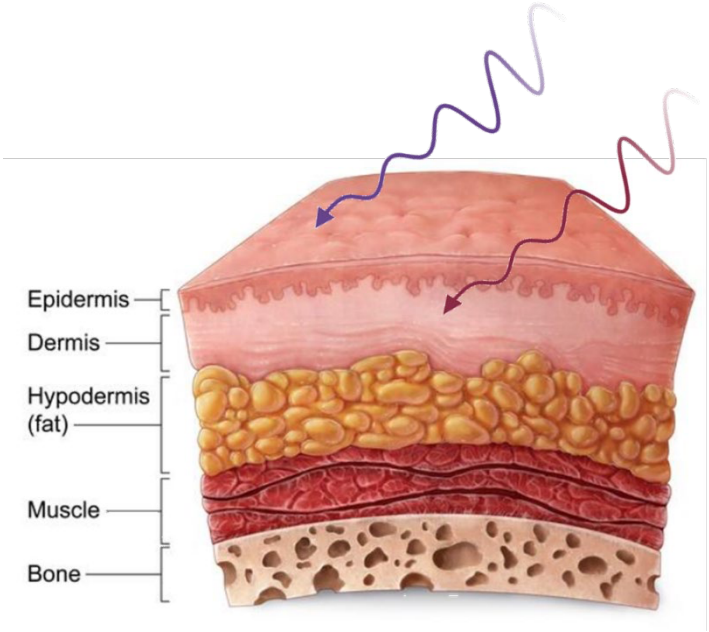

Figure 212. Different skin layers

CaPs as alternative ingredient in sunscreens

The interest in CaPs as sunscreen ingredients to replace ZnO or TiO_2 has increased in recent years [5], [18], [19], [20], [21], [22], as they are considered safe from a human health and environmental perspective, as they don't have photocatalytic effects. In particular, HA has demonstrated non-toxicity and biocompatibility properties, high dermal tolerance and a reduced bleaching effect compared to other inorganic agents. However, the only limitation to the use of CaPs is their limited capacity to absorb UV radiation, which is related to their electronic structure. Their optical absorption range is only from 200 to 340 nm, with a peak below 247 nm [23]. Fortunately, this range can be extended by introducing foreign elements into the CaPs crystal structure, such as Fe^{3+}, Cr^{3+}, Mn^{2+}, Zn^{2+} or Ag^{+}. Thanks to a cation exchange reaction between these dopant elements and the Ca ions on the CaPs' surface, the material can absorb in the range between UVB and UVA (290-400 nm) [21], [24], [25], [26], [27], [28].

Non-doped CaPs are nevertheless useful in sunscreen products, as they can act as boosters, i.e. substances that can increase the protective capacity of the sunscreen product without directly absorbing UVR. These ingredients work in synergy with UV filters and can increase the SPF value through two main mechanisms:

- optimisation of the absorption efficiency of the filters.
- optimisation of the film-forming properties of the product.

The absorption efficiency can be enhanced by incorporating particles into the formulation that can disperse radiation throughout the formulation, increasing the probability of absorption by the filters [19]. The incorporation of polymers and waxes, such as beeswax and alkenes [29] can also help by improving the film-forming properties of the product and increasing its thickness. This results in an improved distribution of the creams and filters over the skin's surface, enhancing the product's overall protection factor.

The data reported in this chapter are relative to the formulation and characterization of sunscreens containing CaP extracted from salmon bones as SPF booster in combination with OCR, BMDBM and ZnO at different concentrations as active UV-filtering ingredients. Synthetic HA – hereafter named CaP-S – was used as comparison and reference material, as it is already employed in commercial sunscreen in combination with UV-filters.

3.2. Materials & methods

Salmon bones (Salmo salar) were furnished by a local enterprise. *Phosphoric acid* (ACS reagent, ≥ 85 wt.% pure in H_2O) and *calcium hydroxide* (ACS reagent, purity ≥ 95.0%) and *synthetic hydroxyapatite* [$Ca_{10}(PO_4)_6(OH)_2$], used as a reference, were supplied by Sigma Aldrich. All the solutions were prepared with *ultrapure water* (18.2 MΩ × cm, 25°C, Arium© pro, Sartorius, Gottingen, Germany). *Glycerine* ($C_3H_8O_3$, BioXtra, ≥ 99%), *ethylenediaminetetraacetic acid disodium salt dihydrate - disodium EDTA* ($C_{10}H_{14}N_2Na_2O_8 \cdot 2H_2O$, Sigma Aldrich, purity ≥ 95%), *xanthan gum* ($C_{35}H_{49}O_{29}$, Sigma Aldrich), *Emulgade® 165* (mixture of glyceryl stearate and PEG-100 stearate, BASF), *cetearyl alcohol* ($CH_3(CH_2)_nOH$, ACEF), *Cetiol® CC* (dicaprylyl carbonate ($C_{17}H_{34}O_3$, BASF), *Myritol® 331* (mixture of decanoyl/octanoyl glyceride, BASF), *cetearyl alcohol* ($CH_3(CH_2)_nOH$, BASF), *silicone 200-350* (dimethicone, C_3H_9SiO-$[C_2H_6O]_n$-C_3H_9Si, n=200-350, ACEF) were used for the preparation of emulsions. Finally, *octocrylene* (OCR, $C_{24}H_{27}NO_2$) and *butyl methoxydibenzoylmethane* (avobenzone, BMDBM, $C_{20}H_{22}O_3$) were purchased by BASF, while *ZnO* was purchased by Sigma Aldrich. ZnO used in this work was coated with 2% of triethoxyprilysilane.

3.2.1. CaP-N production

In this work, the CaP used as booster in sun cream is the inorganic phase obtained from the calcination of salmon bones (CaP-N). Following the separation of the meat, the bones were subjected to an overnight drying process at 105°C to reduce the water content. The material was then calcined in an electric furnace with a thermal ramp of 100°C/h, followed by an isothermal treatment at 800°C for 1h [12]. An aliquot of the material was ground in a ball mill for 30' and sieved through a stainless-steel sieve to obtain particles with a diameter of 50 μm or less. A schematic representation of the process is shown in Scheme 1:

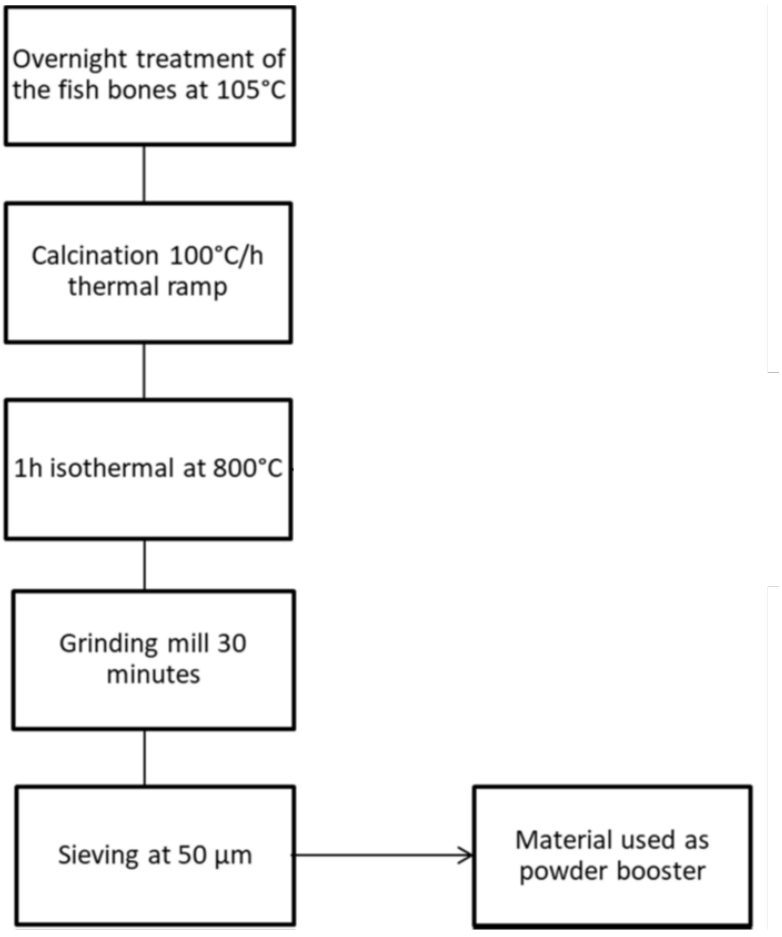

Scheme 1. Schematic representation of the CaP-N preparation process [12]

3.2.2. CaP-N characterisations

CaP-N was analysed by X-ray diffraction (*XRD*) using a D8 Advance diffractometer (Bruker) equipped with a position-sensitive Lynx-eye detector, with CuKα radiation (λ = 1.54178 Å), at 40 kV and 40 mA. XRD patterns were acquired in the range 10-60° (2θ), with a step size of 0.02° and a scan rate of 0.5s. The weight composition of the phases was refined on the basis of a multiphase system, using the tabulated atomic coordinates of HA (ASTM Card No. 09-0432) and β-TCP (ASTM Card No. 09-0169), by Rietveld refinement.

Sample morphology was evaluated with a scanning electron microscopy with a field-emission microscope (*FEG-SEM*, mod. ΣIGMA, ZEISS NTS Gmbh, Oberkochen, Germany) equipped with an EDS probe (INCA Energy 300, Oxford Instruments, Abingdon-on-Thames, UK) in secondary electrons mode at an acceleration voltage of 4 kV. For each specimen and treatment, at least four randomly selected fields were acquired at magnifications ranging from 2,500x to 100,000x. The preparation of powdered samples consisted in their deposition on a carbon tape mounted on an aluminium SEM stub and sputter coated (Polaron E5100, Polaron Equipment, Watford, Hertfordshire, UK) with 10 nm of gold to improve the electrical conductance. Accelerating voltage in the range between 3.0 and 5.0 keV was used to observe samples in the secondary electron imaging mode.

The elementary composition of samples was determined using inductively coupled plasma optical emission spectrometry (*ICP-OES*) on a Liberty 200 spectrometer (Agilent Technologies 5100 ICP-OES, Santa Clara, CA, USA Varian, Palo Alto, USA). Samples preparation was achieved by putting 10 mg of each powdered sample in 50 mL of 2.0 wt.% HNO_3 solution. Atomic emission of the main elements composing the samples was measured at the following wavelengths: 422.673 nm for Ca, 213.618 nm for P and 279.553 nm for Mg, 257.610 nm for Mn, 396.152 nm for Al, 202.548 nm for Zn and 460.733 nm for Sr.

Fourier transform infrared spectroscopy analyses in attenuated total reflection mode (*FTIR-ATR*) were carried out using a Nicolet iS5 spectrometer (Thermo Fisher Scientific Inc., Waltham, MA, USA) with a resolution of 1 cm^{-1} by accumulation of 32 scans covering the 4000 to 400 cm^{-1} range, using a diamond ATR accessory model iD7.

3.2.3. SPF analysis

The SPF value was determined by in vitro SPF analysis using the COLIPA and the Diffey-Robson methods, described in the following chapters.

COLIPA Method [30]

The most widely method used to determine the in vitro SPF is the COLIPA method, which employs spectrophotometric techniques to determine the absorbance of a sun formulation in the UVR range (290-400 nm for SPF, 320-400 nm for UVA-PF) and correlates the absorbance values with the SPF through mathematical processing.

The test is performed on 25 cm x 25 cm UV-transparent, non-fluorescent, photostable polymethylmethacrylate (PMMA) plates with a roughened side that simulates the texture of the skin. 1.3 mg/cm2 (32.5 mg tot) of sunscreen is applied to each plate and evenly distributed by spreading it with a pre-saturated finger.

The plates are then left in the dark for 15' to allow the volatile components of the formulation to evaporate and then analysed using a UV-vis spectrophotometer between 290 and 400 nm. Four sets of measurements are taken for each plate, rotating the plate through 90° between each measurement to reduce the estimation error due to a not perfectly uniform coating.

The SPF is then calculated by Equations 1 and 2, which combine the absorbance values obtained with tabulated parameters [30].

$$SPF_{\text{in vitro}} = \frac{\int_{\lambda=290}^{\lambda=400} E(\lambda) \cdot I(\lambda) \cdot d\lambda}{\int_{\lambda=290nm}^{\lambda=400nm} E(\lambda) \cdot I(\lambda) \cdot 10^{-A(\lambda)} \cdot d\lambda}$$

Equation 1. COLIPA in vitro SPF calculation

$$UVAPF_{\text{in vitro}} = \frac{\int_{\lambda=320nm}^{\lambda=400nm} P(\lambda) \cdot I(\lambda) \cdot d\lambda}{\int_{\lambda=320nm}^{\lambda=400nm} P(\lambda) \cdot I(\lambda) \cdot 10^{-A(\lambda)} \cdot d\lambda}$$

Equation 2. COLIPA in vitro UVA-PF calculation

Where:

- E (λ) is the erythema action spectrum (CIE 1987), it represents the relative effect of individual wavelengths or wavebands on a specified biological response.
- I (λ) is the spectral irradiance of the UV source, irradiance per unit wavelength (Wm^{-2} nm).
- A (λ) is the mean monochromatic absorbance measurement per plate, corresponding to the sunscreen absorbance for each wavelength.
- dλ is the wavelength step (1 nm).
- P (λ) is the PPD (permanent pigment darkening) action spectrum.

Diffey-Robson Method [31]

An alternative approach for calculating the in vitro SPF value is the Diffey-Robson method. The experimental procedure is the same as for the COLIPA method, except for the mathematical processing and the utilisation of a blank, as illustrated in Equation 3. Transmittance values are acquired instead of absorbance values and the wavelengths considered are not all, but one in every 5.

The blank consists of a PMMA plate covered with a thin layer of glycerine, which is analysed like any other sample.

$$SPF_{\text{in vitro}} = \frac{\sum_{400\ \text{nm}}^{290\ \text{nm}} E(\lambda)\varepsilon(\lambda)}{\sum_{400\ \text{nm}}^{290\ \text{nm}} E(\lambda)\varepsilon(\lambda)/PF(\lambda)}$$

Equation 3. Diffey-Robson in vitro SPF calculation

Where:

- E (λ) the erythemal spectral effectiveness.
- ε(λ) is the solar spectral irradiance.
- dλ is the wavelength step (5 nm).
- PF is the monochromatic protection factor, given by the ratio of the transmittance of the blank to that of the sample at each wavelength.

It has been shown that among the various in vitro SPF determination methods, the Diffey-Robson method gives the best correlation with the results obtained in vivo [26].

3.2.4. Sunscreen formulations with CaP-N

O/W emulsions containing a single UV filter at a time were prepared. The UV filters used are those described in chapter 1.1, i.e. OCR, BMDBM and ZnO.

Sunscreen formulations using organic UV filters

The creams were prepared with a fixed CaP-N booster concentration (9% w/w) and a variable concentration of UV filters. OCR was used at 10% and 20% w/w, while those containing BMDBM were prepared at 5% w/w, i.e. the maximum legal concentration. Additionally, a control cream without CaP as booster was prepared for each set.
The sunscreen formulation consists of three phases:

- aqueous phase (*phase A*), containing: glycerine, a humectant, disodium EDTA, a chelating agent, and xanthan gum, a gelling agent.
- oil phase (*phase B*), containing: Emulgade® 165, mixture non-ionic emulsifiers, lanette O, an emollient and rheological modifier, Cetiol® CC, a fast spreading emollient, Myritol® 331, a medium spreading emollient, silicone 200-350, a polymer with film-forming and anti-foaming properties.
- booster (*phase C*): mineral phase of salmon bones.

Phases A and B were treated to obtain an O/W emulsion using the hot/hot method, followed by the addition of the booster.
The composition of the formulation with varying amount of UV filters and booster is shown in Tables 14 and 15.

Table 14. Formulation with 10-20% w/w of OCR and 9% w/w of CaP-N powder as booster

OCR + CaP-N						
			UV Filter + booster concentrations			
			10%+ 0% (w/w)	*10% + 9% (w/w)*	*20% + 0% (w/w)*	*20%+ 9% (w/w)*
Phases	*Ingredients*	*INCI name*	*Ingredients amounts (g)*			
A	Water	Water	34.20	30.78	30.40	26.98
	Glycerin	Glycerin	1.50	1.35	1.33	1.18
	EDTA	Disodium EDTA	0.05	0.05	0.05	0.04
	Xanthan gum	Xanthan gum	0.10	0.09	0.09	0.08
B	Emulgade 165	-Glyceryl stearate -PEG 100 stearate	2.75	2.48	2.44	2.17
	Lanette O	Cetearyl alcohol	0.90	0.80	0.80	0.75
	Cetiol CC	Dicaprylyl carbonate	2.50	2.25	2.22	1.97
	Myritol 331	Cocoglycerides	2.50	2.25	2.22	1.97
	Silicone 200-350	Dimethicone	0.50	0.45	0.45	0.40
	UV filter		5	5	10	10
C	Booster		0	4.5	0	4.5
Total mass cream (g)			50	50	50	50

Table 15. Formulation with 5% w/w of BMDBM and 9% w/w of CaP-N powder as booster

BMDBM + CaP-N				
			UV Filter + booster concentrations	
			5% + 0% (w/w)	*5% + 9% (w/w)*
Phases	*Ingredients*	*INCI name*	*Ingredients amounts (g)*	
A	Water	Water	36.10	32.68
	Glycerin	Glycerin	1.58	1.43
	EDTA	Disodium EDTA	0.05	0.05
	Xanthan gum	Xanthan gum	0.11	0.11
B	Emulgade 165	-Glyceryl stearate -PEG 100 stearate	2.90	2.52
	Lanette O	Cetearyl alcohol	0.95	0.86
	Cetiol CC	Dicaprylyl carbonate	2.64	2.43
	Myritol 331	Cocoglycerides	2.64	2.43
	Silicone 200-350	Dimethicone	0.53	0.49
	UV filter		2.5	2.5
C	Booster		0	4.5
Total mass cream (g)			50	50

The components of phase B and A, except for the xanthan gum, were weighted in two separate beakers using an analytical balance. Both phases are heated up to about 75°C keeping the aqueous phase under agitation by an overhead stirrer (LD Overhead Stirrer - Velp Scientifica model 2). When the desired temperature is reached, the xanthan gum is added to phase A. Then phase B is slowly added to the aqueous phase under vigorous stirring.

Phase C, when present, is added to the already formed emulsion, keeping the system under agitation. Finally, the emulsion was homogenized with a Helidolph Diax 600 Homogenizer. The obtained emulsion is slowly left to cool down at RT and then stored in a fresh and dark cabinet. A schematic representation of the process is reported in Figure 24:

Figure 213. A schematic representation of the emulsion preparation process

Formulations with OCR were analysed and processed according to the COLIPA and Diffey-Robson methods. For the BMDBM, the SPFs of three different final cream weights were analysed and processed according to the COLIPA and Diffey-Robson methods.

Sunscreen formulations using inorganic UV filters

After the CaP-N extraction process described in Chapter 2.2.2., 100 g of the obtained material was ground for 20' in a ball mill together with 100 mL of water and 200 g of grinding media. The dried products were sieved through a 32 μm stainless steel sieve to obtain homogeneous powders and to remove any impurities.

The creams were prepared with a fixed UV filter concentration (20% w/w) and a variable booster concentration (4% and 9% w/w), and their in vitro SPF values were calculated using the standard COLIPA and the Diffey-Robson methods.

The SPF results obtained were compared with those of ZnO-based creams containing CaP-S, to compare the performance of the natural booster with a synthetic one as a reference.

The sunscreens were obtained with an O/W emulsion using the hot/hot method, as for the formulation with organic filters. However, in this case, there are only two phases: phase A is the oil phase and phase B is the water phase. The ingredients used for the formulation are listed in the Table 16.

Table 16. Composition of the formulation with 20% w/w ZnO and 4% and 9% w/w of CaPs booster

ZnO + CaPs					
			UV Filter + booster concentrations		
			20% + 0% (w/w)	*20% + 4% (w/w)*	*20% + 9% (w/w)*
Phases	*Ingredients*	*INCI name*	*Ingredients amount (g)*		
A	Emulgade 165	-Glyceryl stearate -PEG 100 stearate	2.20	2.20	2.20
	Cetiol CC	Dicaprylyl carbonate	6.02	6.02	6.02
	Myritol 331	Cocoglycerides	6.02	6.02	6.02
	UV filter	-Glyceryl stearate -PEG 100 stearate	10	10	10
	Booster		0	2	4.5
	Lanette O	Cetearyl alcohol	0	1	2.25
B	Water	Water	24.01	20.76	16.51
	Glycerine	Glycerine	1.5	1.5	1.5
	Xanthan gum	Xanthan gum	0.25	0.5	1
Total mass cream (g)			50	50	50

The two phases were heated in two separate beakers to 75°C under agitation with an LD - Velp Scientifica model 2 overhead stirrer. Once phase A had reached this temperature, the inorganic filter was added and stirred until homogeneous mixing was achieved, after which phase B was added. The two phases were stirred for a few minutes and then homogenised using a Helidolph Diax 600 homogeniser. The resulting emulsion was allowed to cool slowly to RT and then stored in a cool, dark cupboard.

3.3. Results

It is important to note that the formulations tested were standard base and research formulations, without important components for commercial products, such as preservatives. Furthermore, each formulation contained a single filter, in some cases at concentrations not allowed for commercial use, whereas commercial sunscreens always contain a blend of filters to provide broad-spectrum protection.

3.3.1. Boosters' characterisation

The physicalo-chemical properties and the morphology of the powders have been characterized by X-Ray Diffraction, Scanning Electron Microscopy and Ion Coupled Plasma analysis.The XRD patterns shown in Figure 25 indicate that CaP-N has a biphasic composition consisting of 41.5% of HA (ASTM Card file No. 00-009-0432) and 58.5% of β-TCP (ASTM Card file No. 00-009- 0169).

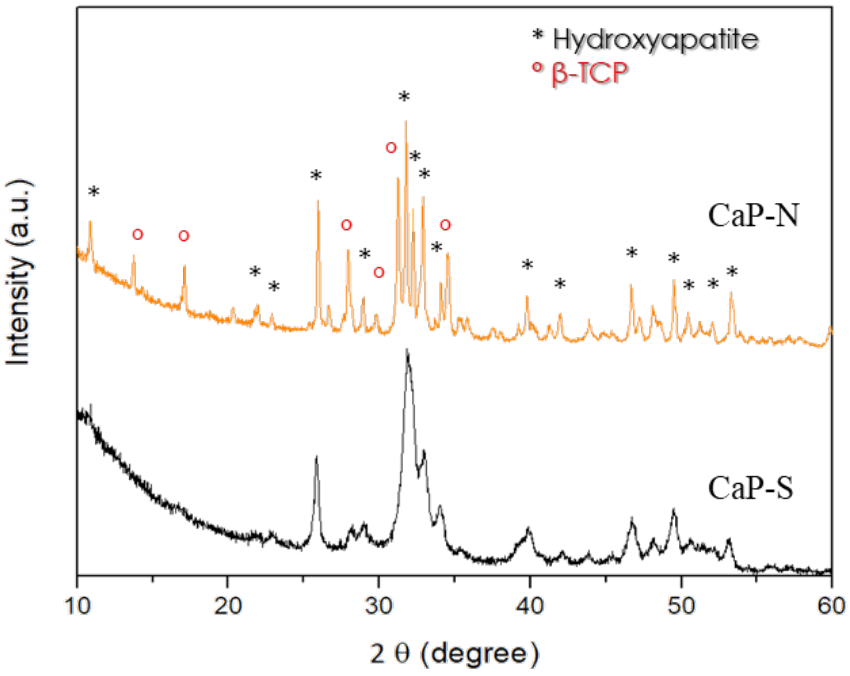

Figure 214. XRD patterns of calcined CaP-N & CaP-S powders

The spectrum indicates a highly crystalline material due to partial grain growth and sintering during the heat treatment, leading to β-TCP formation and recrystallisation of the material. Conversely, CaP-S consists entirely of HA and present a spectrum typical of nanocrystalline apatite.
The presence of β-TCP in CaP-N powder was expected, as it's commonly obtained by calcination of biological or biomimetic HA around 700-800°C.

SEM images in Figure 26 show the presence of two populations of particles, with different sizes and shapes: rod-like shaped and sub-micrometric crystals.

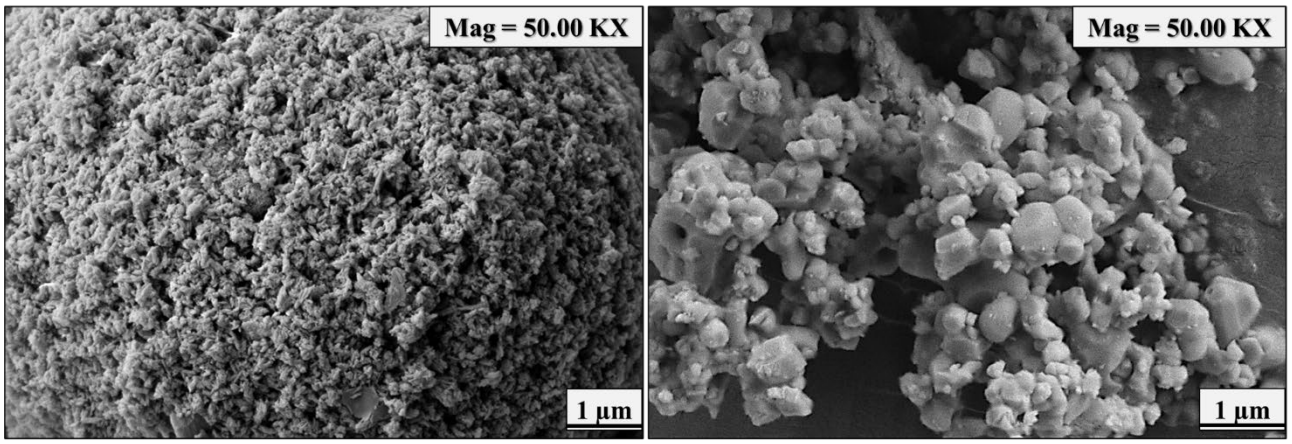

Figure 215. SEM micrographs of powder CaP-S, on the left, and powder CaP-N, on the right

The heat treatment to which the fish bones were subjected completely eliminated all traces of organic matter.

In fact, in the FTIR-ATR spectrum of the calcined materials shown in Figure 27, only the peaks for phosphate and carbonates groups can be seen, both for CaP-N and, of course, for CaP-S.

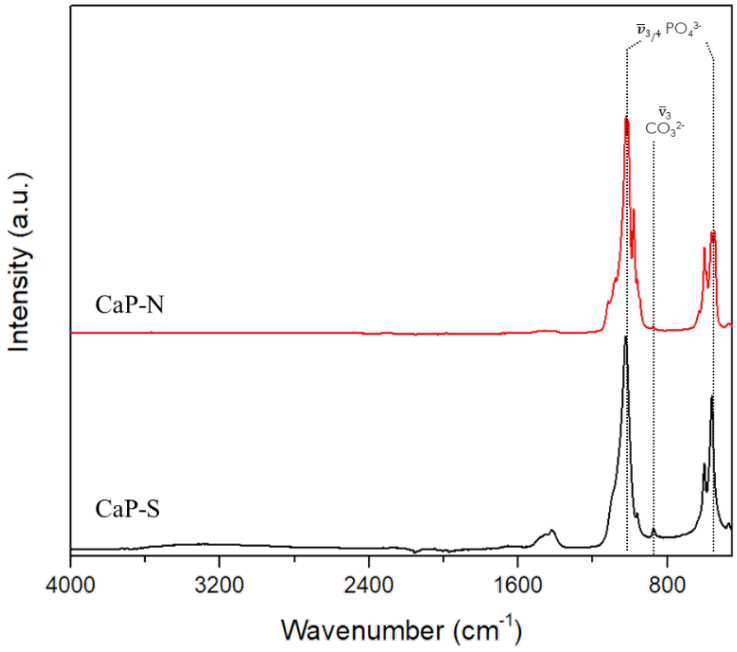

Figure 216. FTIR-ATR of CaP-N & CaP-S calcined powder

The ICP analysis of CaP-S and CaP-N excluded the presence of toxic elements or pollutants, showing that both powders were composed primarily of Ca and P ions, with only a few traces of foreign elements, as can be seen in Table 17. Of the two materials, CaP-N contains a higher amount of foreign elements, like Mg, Al and Sr, due to its biogenic nature. The presence of these elements, along with the composition of the powder, which includes not only HA but also β-TCP, results in a decreased Ca/P ratio with respect to the stoichiometric value of 1.67. CaP-S is composed almost entirely of Ca and P, with only a minor quantity of Mg, probably due to impurities in the synthesis. Its Ca/P ratio is in fact much closer to the stoichiometric value than that of CaP-N, but is still slightly lower. These results are in accordance with those previously reported in the literature concerning CaPs synthesised from salmon, along with synthetic hydroxyapatite [32], [33].

Table 17. ICP-OES results of CaP-N & CaP-S calcined powders. Results are shown as the mean of three measurements ± standard deviation.

	CaP-N	*CaP-S*
Ca *(Average ± SD wt.%)*	32.79 ± 2.17	33.58 ± 3.73
P *(Average ± SD wt.%)*	18.09 ± 1.14	16.09 ± 1.86
Al *(Average ± SD wt.%)*	0.10 ± 0.02	0.03 ± 0.00
Mg *(Average ± SD wt.%)*	0.73 ± 0.06	0.28 ± 0.03
Mn *(Average ± SD wt.%)*	0.00 ± 0.00	0.01 ± 0.00
Sr *(Average ± SD wt.%)*	0.07 ± 0.00	0.01 ± 0.00
Zn *(Average ± SD wt.%)*	0.02 ± 0.00	0.01 ± 0.00
Ca/P *(mol/mol ± SD)*	1.40 ± 0.01	1.61 ± 0.01
Cations/P *(mol/mol ± SD)*	1.46 ± 0.01	1.64 ± 0.01

3.3.2. SPF results

Organic filters

Formulation with 10% w/w and 20% w/w OCR

The formulations described in this study are intended for research purposes only. Notably, the EU permits a maximum OCR concentration of 10% w/w. Therefore, the relevance of these results lies in exploring the potential relationship between the boosting effect and filter concentration, rather than their direct market applicability. The results of the SPF tests conducted in accordance with the COLIPA method for a control emulsion (containing no booster but only the UV filter) and for a series of creams containing 10% or 20% w/w OCR + 9% w/w CaP-N, are reported in Table 18.

Table 18. 10% and 20% w/w OCR SPF results obtained with the COLIPA method. Results are shown as the mean of four measurements ± standard deviation.

Formulations	**SPF**	**UVA-PF**
10% w/w OCR	16.4 ± 0.7	2.32 ± 0.03
10% w/w OCR + 9% w/w CaP-N	15.1 ± 0.5	2.40 ± 0.03
20% w/w OCR	43.6 ± 4.6	3.81 ± 0.21
20% w/w OCR + 9% w/w CaP-N	65.6 ± 2.3	4.20 ± 0.05

The SPF results obtained for the same creams using the Diffey-Robson method are shown in Table 19.

Table 19. 10% and 20% w/w OCR SPF results obtained with the Diffey-Robson method. Results are shown as the mean of four measurements ± standard deviation.

Formulations	**SPF**
10% w/w OCR	11.2 ± 0.4
10% w/w OCR + 9% w/w CaP-N	10.5 ± 0.3
20% w/w OCR	24.1 ± 1.7
20% w/w OCR + 9% w/w CaP-N	31.2 ± 0.7

Results obtained with the two methods are very different from each other, especially for 20% w/w formulations, since the Diffey-Robson method takes into account a blank which is not present in the mathematical reworking of COLIPA, and the tabulated data for the two methods are different from each other.

The addition of the booster proved to increase the SPF value for the 20% w/w formulations, while it didn't seem to have any effect on the 10% w/w formulations, where the SPF actually decreased. The UVA-PF values also showed no improvement after the addition of the booster, remaining almost unchanged for all formulations.

Formulation with 5% w/w BMDBM

Creams containing BMDBM were studied at the highest concentration allowed by the EU, as no data are available on its behaviour in combination with CaP-N.
Tables 20 and 21 show the SPF values obtained from the absorbance and transmittance values processed by the COLIPA and Diffey-Robson methods.

Table 20. 5% w/w BMDBM SPF results obtained with the COLIPA method. Results are shown as the mean of four measurements ± standard deviation.

Formulations	SPF	UVA-PF
1. 5% w/w BMDBM	11.0 ± 1.1	30.3 ± 7.1
2. 5% w/w BMDBM		
3. 5% w/w BMDBM		
1. 5% w/w BMDBM + 9% booster	13.8 ± 2.5	40.8 ± 10.7
2. 5% w/w BMDBM + 9% booster		
3. 5% w/w BMDBM + 9% booster		

Table 21. 5% w/w BMDBM SPF results obtained with the Diffey-Robson method. Results are shown as the mean of four measurements ± standard deviation.

Formulations	SPF
1. 5% w/w BMDBM	9.1 ± 0.9
2. 5% w/w BMDBM	
3. 5% w/w BMDBM	
1. 5% w/w BMDBM + 9% booster	11.3 ± 2.0
2. 5% w/w BMDBM + 9% booster	
3. 5% w/w BMDBM + 9% booster	

It can be observed that the SPF values in all formulations remains almost constant. It should be noted that BMDBM is a photo-unstable filter, and that in commercial formulations it is always coupled with a stabiliser, whereas in these formulations it's not stabilised. As the protocol involves three different series of measurements of four irradiations, resulting in a total of twelve, there is a high probability of photodegradation of the filter, due to its nature. For this reason, the analysis cannot be considered conclusive, and it would be useful to test the behaviour of stabilised BMDBM.

Inorganic filter

Formulation with 20% w/w ZnO

The results of the SPF tests conducted in accordance with the COLIPA and Diffey-Robson methods for a control emulsion (containing no booster but only the UV filter) and for a series of creams containing 20% w/w ZnO + 4% or 9% w/w booster, are reported in Tables 22 and 23.

Table 22. 20% w/w ZnO SPF results obtained with the COLIPA method. Results are shown as the mean of four measurements ± standard deviation.

Formulations	**SPF**	**UVA-PF**
20% w/w ZnO	16.6 ± 1.2	12.9 ± 0.8
20% w/w ZnO + 4% w/w CaP-N	21.5 ± 1.0	15.7 ± 0.7
20% w/w ZnO + 4% w/w CaP-S	33.4 ± 1.0	20.7 ± 0.5
20% w/w ZnO + 9% w/w CaP-N	18.3 ± 4.8	14.5 ± 3.0
20% w/w ZnO + 9% w/w CaP-S	19.1 ± 2.2	14.6 ± 1.7

Table 23. 20% w/w ZnO SPF results obtained with the Diffey-Robson method. Results are shown as the mean of four measurements ± standard deviation.

Formulations	**SPF**
20% w/w ZnO	10.4 ± 1.1
20% w/w ZnO + 4% w/w CaP-N	15.5 ± 0.6
20% w/w ZnO + 4% w/w CaP-S	22.5 ± 1.7
20% w/w ZnO + 9% w/w CaP-N	13.3 ± 3.1
20% w/w ZnO + 9% w/w CaP-S	20.2 ± 3.8

The SPF values increased in the presence of the 4% w/w booster, whereas at the higher concentration lower SPF values were obtained, comparable to those of the cream without booster. It is hypothesised that this behaviour is due to the fact that 4% CaPs is sufficient to achieve the maximum SPF-increasing effect, so even by increasing the booster concentration, the SPF does not increase.

In contrast to the formulations with OCR, in this case the UVA-PF values also increase in the presence of the booster, particularly with 4% w/w CaP-N, indicating that it is able to extend the protection of the inorganic filters across the entire UV spectrum.

3.4. Conclusions

This study evaluated the performance of a SPF booster made from waste products from the fishing industry, particularly from *Salmo salar* bones, to be used in sunscreens in combination with widely used UV-filters, in accordance with the principles of the Circular Economy. The material was tested in combination with two organic filters at different concentrations, OCR (10% and 20% w/w) and BMBDM (5% w/w), and an inorganic filter, the ZnO at 20% w/w.

The results showed that all the filters employed exhibited synergistic effects with the CaP-N powder, demonstrating that the booster activity of the material can be enhanced. Indeed, in all cases, higher SPF values were obtained in the presence of the booster compared to the control creams; in particular the best results for ZnO formulations were obtained with 4% w/w of CaP-N, the lowest concentration tested. This result is particularly noteworthy as it enables the production of 'full mineral' sunscreens containing only mineral UV-active components.

Such formulations meet the dual requirements of being both safe for consumers and environmentally friendly, while also providing high protection against UV radiation. However, further studies are needed to determine the behaviour of the booster in the presence of a filter mixture.

References

[1] Y. Matsumura and H. N. Ananthaswamy, “Toxic effects of ultraviolet radiation on the skin,” Mar. 15, 2004. doi: 10.1016/j.taap.2003.08.019.

[2] K. Geoffrey, A. N. Mwangi, and S. M. Maru, “Sunscreen products: Rationale for use, formulation development and regulatory considerations,” Nov. 01, 2019, Elsevier B.V. doi: 10.1016/j.jsps.2019.08.003.

[3] T. G. Smijs and S. Pavel, “Titanium dioxide and zinc oxide nanoparticles in sunscreens: Focus on their safety and effectiveness,” 2011, Dove Medical Press Ltd. doi: 10.2147/nsa.s19419.

[4] M. F. Holick, “Vitamin D: A D-Lightful health perspective,” in Nutrition Reviews, Oct. 2008. doi: 10.1111/j.1753-4887.2008.00104.x.

[5] F. Carella, L. Degli Esposti, A. Adamiano, and M. Iafisco, “The use of calcium phosphates in cosmetics, state of the art and future perspectives,” Nov. 01, 2021, MDPI. doi: 10.3390/ma14216398.

[6] C. A. Downs et al., “Toxicopathological Effects of the Sunscreen UV Filter, Oxybenzone (Benzophenone-3), on Coral Planulae and Cultured Primary Cells and Its Environmental Contamination in Hawaii and the U.S. Virgin Islands,” Arch Environ Contam Toxicol, vol. 70, no. 2, pp. 265–288, Feb. 2016, doi: 10.1007/s00244-015-0227-7.

[7] J. Labille et al., “Assessing Sunscreen Lifecycle to Minimize Environmental Risk Posed by Nanoparticulate UV-Filters – A Review for Safer-by-Design Products,” Jul. 10, 2020, Frontiers Media S.A. doi: 10.3389/fenvs.2020.00101.

[8] E. Manová, N. von Goetz, U. Hauri, C. Bogdal, and K. Hungerbühler, “Organic UV filters in personal care products in Switzerland: A survey of occurrence and concentrations,” Int J Hyg Environ Health, vol. 216, no. 4, pp. 508–514, Jul. 2013, doi: 10.1016/j.ijheh.2012.08.003.

[9] L. A. Baker, M. D. Horbury, and V. G. Stavros, “Ultrafast photoprotective properties of the sunscreening agent octocrylene,” Opt Express, vol. 24, no. 10, p. 10700, May 2016, doi: 10.1364/oe.24.010700.

[10] C. Chaiyabutr et al., “Ultraviolet filters in sunscreens and cosmetic products—A market survey,” Contact Dermatitis, vol. 85, no. 1, pp. 58–68, Jul. 2021, doi: 10.1111/cod.13777.

[11] E. Spongano, “Determination of the SPF booster effect of natural calcium phosphates in sunscreens: an investigation on the effect of different stabilizers,” ALMA MATER STUDIORUM - BOLOGNA UNIVERSITY, 2022.

[12] Erika Spongano, “Determination of the SPF booster effect of natural calcium phosphates in sunscreens: an investigation on the effect of different stabilizers,” ALMA MATER STUDIORUM - Università di Bologna, Rimini, 2022.

[13] European Commission, “Commission regulation (EU) 2022/1176,” Official Journal of the European Union, Jul. 2022, [Online]. Available: https://ec.europa.eu/health/sites/default/files/

[14] N. A. Shaath, “Ultraviolet filters,” 2010, Royal Society of Chemistry. doi: 10.1039/b9pp00174c.

[15] A. C. P. da Silva, B. A. M. C. Santos, H. C. Castro, and C. R. Rodrigues, “Ethylhexyl methoxycinnamate and butyl methoxydibenzoylmethane: Toxicological effects on marine biota and human concerns,” Jan. 01, 2022, John Wiley and Sons Ltd. doi: 10.1002/jat.4210.

[16] Caroppo Priscilla, “Development of a mineral sunscreen formulation using calcium-phosphates from circular economy as SPF booster,” ALMA MATER SUDIORUM - Università di Bologna, Rimini, 2023.

[17] S. L. Schneider and H. W. Lim, “A review of inorganic UV filters zinc oxide and titanium dioxide,” Nov. 01, 2019, Blackwell Publishing Ltd. doi: 10.1111/phpp.12439.

[18] Rachel. Pears, Jessica. Stella, and D. R. Wachenfeld, Final report: 2016 coral bleaching event on the Great Barrier Reef. Great Barrier Reef Marine Park Authority (GBRMPA), 2017.

[19] Ziosi Paola et al., “SPF booster: un nuovo approccio nello sviluppo di prodotti solari,” Cosmet Technol, 2026.

[20] A. Pal, K. Hadagalli, P. Bhat, V. Goel, and S. Mandal, “Hydroxyapatite—a promising sunscreen filter,” Journal of the Australian Ceramic Society, vol. 56, no. 1, pp. 345–351, Mar. 2020, doi: 10.1007/s41779-019-00354-2.

[21] A. Huynh, M. S. Abou-Dahech, C. M. Reddy, G. W. O’Neil, M. Chandler, and G. Baki, “Alkenones, a renewably sourced, biobased wax as an SPF booster for organic sunscreens,” Cosmetics, vol. 6, no. 1, Mar. 2019, doi: 10.3390/cosmetics6010011.

[22] M. Boutinguiza, J. Pou, R. Comesaña, F. Lusquiños, A. De Carlos, and B. León, “Biological hydroxyapatite obtained from fish bones,” Materials Science and Engineering C, vol. 32, no. 3, pp. 478–486, Apr. 2012, doi: 10.1016/j.msec.2011.11.021.

[23] Faurschou A. and Wulf H.C., “The relation between sun protection factor and amount of sunscreen applied in vivo,” in British Journal of Dermatology, vol. 156, 2007, pp. 716–719.

[24] H. J. W. Van Den Haak and L. L. M. Krutzer, “Design of pigment dispersants for high-solids paint systems,” 2001.

[25] A. Dimitrovska Cvetkovska et al., “Factors affecting SPF in vitro measurement and correlation with in vivo results,” Int J Cosmet Sci, vol. 39, no. 3, pp. 310–319, Jun. 2017, doi: 10.1111/ics.12377.

[26] C. Couteau, E. Paparis, S. El-Bourry-Alami, and L. J. M. Coiffard, “Influence on SPF of the quantity of sunscreen product applied,” Int J Pharm, vol. 437, no. 1–2, pp. 250–252, Nov. 2012, doi: 10.1016/j.ijpharm.2012.08.019.

[27] G. Magnani, “Photo-protective performances and Life Cycle Assessment of a novel SPF booster developed from the circular economy of food by-products: towards more sustainable sunscreen,” ALMA MATER STUDIORUM - Bologna University, 2021.

[28] S. Fortunati, L. Martiniello, and D. Morea, “The strategic role of the corporate social responsibility and circular economy in the cosmetic industry,” Sustainability (Switzerland), vol. 12, no. 12, Jun. 2020, doi: 10.3390/su12125120.

[29] A. Huynh, M. S. Abou-Dahech, C. M. Reddy, G. W. O’Neil, M. Chandler, and G. Baki, “Alkenones, a renewably sourced, biobased wax as an SPF booster for organic sunscreens,” Cosmetics, vol. 6, no. 1, Mar. 2019, doi: 10.3390/cosmetics6010011.

[30] COLIPA In vitro UV Protection Method Task Force, “In vitro method for the determination of the UVA protection factor and ‘critical wavelenght’ values of sunscreen products,” Mar. 2011.

[31] Diffey B. L. and Robson J., “A new substrate to measure sunscreen protection factors throughout the ultraviolet spectrum,” Journal of the Society of Cosmetic Chemists, vol. 40, no. 3, pp. 127–133, 1989.

[32] A. Adamiano et al., “Simultaneous extraction of calcium phosphates and proteins from fish bones. Innovative valorisation of food by-products,” J Clean Prod, vol. 385, Jan. 2023, doi: 10.1016/j.jclepro.2022.135656.

[33] F. Carella et al., “Thermal conversion of fish bones into fertilizers and biostimulants for plant growth-A low tech valorization process for the development of circular economy in least developed countries,” J Environ Chem Eng, vol. 9, no. 1, Feb. 2021, doi: 10.1016/j.jece.2020.104815.

CHAPTER IV: ORAL CARE

4.1. Introduction

Dental caries was defined in 2017 as the most widespread non-communicable disease, affecting billions of people worldwide [1]. When the pH of the oral microenvironment becomes lower than a critical value - ca. 5.5 for dental enamel and 6.2 for dentin – the mineral constituent of the tooth, hydroxyapatite (HA, $Ca_{10}(PO_4)_6(OH)_2$), starts to dissolve [2]. The main factors for this phenomenon are the metabolism of cariogenic bacteria, the consumption of acidic foods, and gastroesophageal reflux disease (GERD) [3]. The consequence of demineralization is the formation of an ionic imbalance on the tooth surface, causing progressive loss of Ca^{2+} and PO_4^{3-} ions and tissue degradation.

Demineralization is a reversible process, and if (i) the pH of the oral microenvironment is higher than the critical values and (ii) free Ca^{2+} and PO_4^{3-} ions are available, the ionic balance is inverted and remineralization of the depleted tissues occurs [4]. In ideal physiological conditions, saliva provides ions and buffering effect, stimulating remineralization. Unfortunately, this activity is insufficient to contrast and restore demineralization generated by cariogenic bacteria [3]; thus, an external supply of calcium and phosphate ions is required to shift the equilibrium toward remineralization [5, 6]. Naturally, among most common remineralizing agents are calcium phosphate (CaP) materials [7], which have a chemical composition similar to that of dental hard tissues [8]. Most frequently, CaPs are represented by synthetic HA nanoparticles. Nano-HA has been proven to have excellent action as it releases remineralizing ions and adheres to tooth surface, restoring demineralized lesions [9, 10]. In addition, HA nanoparticles can contrast dentin hypersensitivity by occluding exposed dentinal tubules and forming a mineralized barrier [11].

This chapter has been published as "L. Degli Esposti, A. C. Ionescu, S. Gandolfi et al., "Natural, biphasic calcium phosphate from fish bones for enamel remineralization and dentin tubules occlusion", in Dental Materials, 40 (2024) 593–607

In the last few years, it has been proposed that synthetic CaPs could be complemented or substituted by CaPs from natural sources following a circular economy approach [12, 13]. Food industries produce millions of tons of by-products per year, whose disposal is a severe environmental and economic issue [14]. However, these by-products contain valuable compounds, e.g., CaPs of bones from slaughterhouses or fisheries. In this case, the circular economy approach consists in the extraction and valorization of these CaPs, having the benefits of decreasing the amounts of by-products sent to incinerators and landfills and providing an added economic value to otherwise useless materials [13, 15].

Several natural sources that could yield CaPs have been investigated [13]. In particular, there is a high interest in CaPs from marine sources, as the fish food industry produces large quantities of by-products - e.g., European fisheries produce about 3.1 million tons of by-products per year - that are rich in CaPs (fish scales and bones) [14, 16, 17]. Our research group has recently studied the extraction of CaPs from salmon fish bones (hereafter referred to as CaP-N, being derived from a natural source) by thermal treatment as an effective and easily scalable method [18]. Advanced applications of CaP-N include UV-scattering agents, nutrient delivery agents, and dye adsorbent phases for water remediation [18-20]. As a consequence of extraction through thermal treatment, CaP-N consists of a biphasic mixture of β-tricalcium phosphate (β-TCP, β-form of $Ca_3(PO_4)_2$) and HA [18]. This biphasic composition suggests that CaP-N might be an attractive material for dental remineralization and desensitization. β-TCP is more soluble than HA both in neutral and acidic conditions [21]; thus, CaP-N could have substantial ion release for stimulating remineralization while having at the same time the economic and environmental benefits of being from circular economy sources. Synthetic mixtures of HA and β-TCP similar to CaP-N are known as biphasic calcium phosphates (BCP) and were successfully employed in orthopedics as material for bone substitution [22]. However, to the best of our knowledge, no study has investigated the use of BCP on dental hard tissues. Few recent works have used HA from fish by-products for dental applications such as dental resin composite fillers or enamel

remineralization [23-25]. However, these works have employed pure HA minerals, not BCPs. All these reasons make CaP-N a potentially attractive but still unexplored alternative to synthetic CaPs for dental application.

The present work tested circular economy CaP-N as occlusive agent of dentinal tubules and enamel remineralization agent. The null hypothesis was the absence of remineralizing action on demineralized enamel and dentine and the absence of occlusive action on dentinal tubules. A synthetic stoichiometric nano-HA (CaP-S) was used as a positive control of remineralization and occlusion, while water was used as a negative control.

4.2. Materials & methods

Calcium hydroxide ($Ca(OH)_2$, 95% pure), *lactic acid* ($C_3O_4H_6$, 85 wt.% in H_2O), *phosphate buffered saline* (Dulbecco's modified PBS without $CaCl_2$ and $MgCl_2$, composition: KCl 0.2 g/L, KH_2PO_4 0.2 g/L, Na_2HPO_4 1.15 g/L, NaCl 8.0 g/L), *orthophosphoric acid* (H_3PO_4, 85 wt.% in H_2O), and *sodium lactate solution* ($NaC_3O_4H_5$, 50 wt.% in H_2O) were purchased from Sigma Aldrich (St. Luis, MO, USA). All the solutions were prepared with *ultrapure water* (18.2 MΩ × cm at 25°C, Arium pro, Sartorius, Göttingen, Germany).

4.2.2. Preparation and characterization of CaP-N and CaP-S

CaP-N was prepared from salmon fish bones, as reported by Adamiano et al. [19]. Briefly, clean and dry salmon fish bones were thermally treated at 800°C with a heating ramp of 120°C/h and 1h of dwell time, then ground with a jet mill (PilotMill-2, Food and Pharma Systems s.r.l., Como, Italy) and sieved with a 20 μm sieve.

As reported in a previous work, CaP-S was synthesized by wet precipitation to obtain nanosized HA [26], where the nominal molar Ca/P ratio was set to the stoichiometric value of 1.67. Briefly, 30 mL of an aqueous solution of phosphoric acid (H_3PO_4, 8.87 g) was added drop-wise into 100 mL of calcium hydroxide ($Ca(OH)_2$, 10.00 g) water suspension kept under stirring at RT and atmospheric conditions. After adding the acid, the suspension was stirred for 3h and left overnight before recovering the synthesis product by centrifugation. The obtained material was repeatedly washed with ultrapure water and freeze-dried overnight.

For both CaP-N and CaP-S, powder X-ray diffraction (*PXRD*) patterns were recorded with a D8 Advance Diffractometer (Bruker, Karlsruhe, Germany) equipped with a Lynx-eye position sensitive detector, using the CuKα radiation (λ = 1.54178 Å) generated at 40 kV and 40 mA. PXRD patterns were acquired in the 10-60° (2θ) range with a step size of 0.02° and a scanning speed of 0.5 s. Crystal phase quantification was performed through Rietveld refinement with the software TOPAS5 [27]

considering a multiphase system and using tabulated atomic coordinates of HA (ASTM Card file No. 00–009-0432) and β-TCP (ASTM Card file No. 00–009-0169). All acquisitions were performed in triplicate.

The chemical composition of the materials was analysed on three replicates for each sample using an inductively coupled plasma optical emission spectrometer (*ICP-OES*) (Agilent 5100, Agilent Technologies, Santa Clara, CA, USA). Before analysis, 10 mg of samples were dissolved in 50 mL of 2 wt.% HNO_3 solution. The Ca, P, and Mg content of the samples were measured by their atomic emission at the following wavelengths: 422.673 nm for Ca, 213.618 nm for P, and 279.553 nm for Mg.

The materials' morphology and particle dimension were evaluated by field-emission gun scanning electron microscopy (*FEG-SEM*) (ΣIGMA, ZEISS NTS Gmbh, Oberkochen, Germany). Powders were mounted on aluminum stubs using an adhesive carbon tape and sputter-coated with an 80:20 Pt:Pd alloy in an E5100 Sputter Coater (Polaron Equipment, Watford, Hertfordshire, UK) to improve the electrical conductance. Micrographs were collected at 4 kV acceleration voltage in secondary electron mode at 2500 × - 100,000 × magnifications.

4.2.3. Ion release from CaP samples and characterization of materials after release

Cumulative ion release tests from the tested CaP materials were performed as reported by Degli Esposti *et al.* [28] with some modifications. In detail, slurries of either CaP-S or CaP-N were made by mixing 2 g of dry powders with 6 mL of ultrapure water (pH 7.0) or 0.1 M lactic acid solution (pH 4.5) in triplicate and incubated at 37°C under horizontal agitation. After 30', 2h, 6h, 24h, 3d, and 7d the materials were centrifuged (7000 rpm, 4°C, 5'), and 4.8 mL of the supernatant was collected and replaced with an equal volume of fresh solution. The pH of the supernatants was measured, then the supernatants were diluted 1:5 with 2 wt.% HNO_3 solution and analyzed by ICP-OES to quantify the content of Ca, P, and Mg.

To assess changes to CaPs during ion release, additional samples prepared in the same conditions were centrifuged after 7d of incubation, and the pelleted material was freeze-dried. PXRD and FEG-SEM analyses of the dried powders were performed as reported above.

4.2.4. In vitro evaluation of enamel remineralization and dentinal tubules occlusion

Enamel remineralization and dentinal tubules occlusion in vitro tests were performed as reported by Ionescu *et al.* [5]. In brief, a total of 6 sound (caries-free) erupted human wisdom teeth extracted for clinical reasons were obtained (Oral Surgery Unit, Department of Biomedical, Surgical and Dental Sciences, Milan, Italy) and used for the in vitro experiments. The Ethical Commission of the University of Milan approved the use of the teeth (codename: SALTiBO–2017). All in vitro experiments were performed in accordance with the Declaration of Helsinki, updated by the World Medical Association in 2013. Horizontal sections of the teeth specimens were obtained under constant water cooling using a low-speed saw (Isomet 1000, Buehler, Lake Bluff, IL, USA). First, the crown was sectioned from the root with a cut 2 mm apical to the cementoenamel junction. Then, horizontal cuts of the crown were performed at two depth levels to obtain flat enamel (n = 6) and dentin (n = 6) surfaces from each tooth (Figure 28A). Then, on both dentin and enamel sections, two parallel 0.5 mm-deep notches were made on the top surface of each specimen to mark three areas using a low-speed diamond disc (Horico, Berlin, Germany) (Figure 28B). All surfaces were polished using silicon carbide paper (600 and 1200 grit). The surfaces were etched with a 37 wt.% H_3PO_4 solution for 30 s, followed by extensive rinsing with filter-sterile tap water to generate a superficial demineralization comparable to a white spot lesion of enamel [29].

Before each treatment, an aliquot of CaP-N or CaP-S dry powder was mixed with ultrapure water to obtain a 25 wt.% aqueous slurry.

The three regions of each enamel or dentin specimen were soft-brushed for 3’ using disposable microbrushes (Microbrush, Microbrush International, Grafton, WI, USA) with:

- CaP-N slurry.
- CaP-S slurry (positive control).
- filter-sterile tap water (negative control).

The distribution of groups in the three regions of each specimen was randomized (Figure 28C). After brushing a single region, the specimen was rinsed with filtered sterile tap water for 1’ to stop exposure to the CaP sample. In total, 6 regions of enamel and 6 regions of dentin were brushed with each sample group.

This treatment was repeated twice daily for one week; the slurries were prepared fresh for each treatment. Specimens were stored at 37°C in fresh Dulbecco’s modified PBS (formulation without calcium and magnesium to avoid precipitation of calcium phosphates unrelated to treatments). After the last treatment, half of the specimens (n = 3 for both enamel and dentin) destined for FEG-SEM analysis were dehydrated by immersion in ethanol solution with progressively higher concentrations (35%, 70%, 80%, 90%, and 100% twice) for 5’ each, then left to dry overnight. The remaining specimens were stored under 100% humidity until instrumented indentation tests (Figure 28D).

The dried specimens were fixed on aluminum stubs using conductive graphitic glue with the treated surface upward to observe surface morphology. All specimens were sputter-coated as described above and observed with the FEG-SEM instrument equipped with an EDS probe (INCA Energy 300, Oxford Instruments, Abingdon-on-Thames, UK) in secondary electrons mode at an acceleration voltage of 4 kV. For each specimen and treatment, at least four randomly selected fields were acquired at magnifications ranging from 2500 × to 100000 ×.

For dentin samples, the occlusion of dentinal tubule openings was quantified by digital image analysis of FEG-SEM micrographs using the method reported by Ahmed *et al.* and the open image processing package Fiji [30, 31]. For each treated sample, at least six 5000 × micrographs were acquired, noise was removed by the despeckling process, and then the black openings were selected by adjusting black/white threshold levels. Afterward, the "analyze particles" Fiji plugin was used to measure the opening area. A total of 300 distinct measurements were performed.

Energy-dispersive spectroscopy (EDS) surface compositional analysis was performed with an acceleration voltage of 15 kV. Immediately before sample analysis, the EDS instrument was calibrated by measuring the spectrum of a NIST standard sample of metallic cobalt as suggested by the instrument manufacturer. Six randomly selected fields were acquired for each specimen/treatment combination at 2500 × magnification in full-frame mode using an acquisition time of 50 s. Each field represented a volume area of 10 × 10 x ≈ 1 μm (thickness) of the specimen surface.

After these observations, specimens were carefully detached from the stubs, and a 0.2 mm-deep vertical notch was made on the surface opposite the treated region. Then, a section running through the remineralized layer of enamel and dentin specimens was obtained through fracturing by applying pressure on a 0.2 mm steel wedge placed in the notch. Extreme care was taken through these procedures not to touch the fractured surface to avoid the presence of dirt or artifacts. Finally, the fractured sections were mounted again on aluminium stubs with the fractured surface upward, sputtered, and observed again with the FEG-SEM.

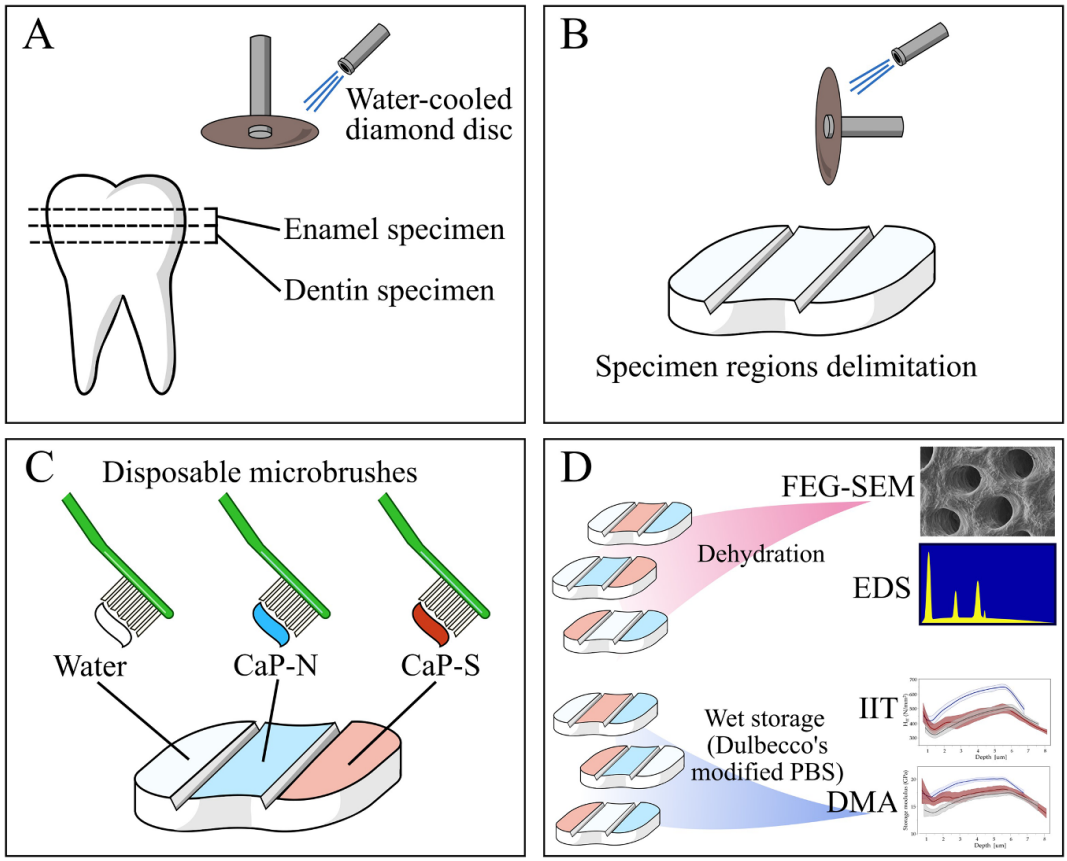

Figure 28. Schematic representation of specimen preparation and treatment. (A) Horizontal sectioning of the tooth to expose enamel and dentin, (B) delimitation of regions by parallel notches, (C) randomized treatment with negative control and samples, (D) post-treatment specimen preparation for characterizations.

4.2.5. Instrumented Indentation Test (IIT)

The ratio of the elastic reverse deformation work of indentation (Welast) and the total mechanical work of indentation (Wtotal) was assessed (Welast/Wtotal = μIT) according to ISO 14577 [32] by using an automated micro-indenter (FISCHERSCOPE® HM2000) equipped with a Vickers diamond tip. This parameter (μIT) is a prerequisite for the dynamic mechanical analysis (DMA) test. For this purpose, 10 measurements were carried out randomly in the dentin and enamel reference specimens under wet conditions. Inside each notch that was created on the specimens' surfaces, a thin cotton thread was placed and connected on both ends to small containers filled with Dulbecco's modified PBS. Thus, the specimen under test was kept from desiccating due to capillarity through the thread. This method allowed to maintain hydrated the specimens during analysis as the instrument cannot operate on completely submerged specimens. The indentation was force-controlled and at RT; the test load increased within 20 s and decreased within 20 s with constant speed in the 0.4 mN to 500 mN range. Load (F) and indentation depth (h) of the indenter were continuously measured during the load-unload-cycle, allowing calculating the elastic and plastic deformation. A part of the mechanical work, Wtotal (= Fdh), during the indentation procedure is consumed as plastic deformation work (Wplast), while the rest is set free as work of the reverse elastic deformation (Welastic). During indentation, an impression is produced with a projected area of contact of the indenter (Ac) determined from the force/indentation depth curve, taking into account the indenter correction based on the Oliver and Pharr model and described in ISO 14577 [32]. The indenter area function was calibrated on two materials with uniform and well-known properties (sapphire and fused quartz). Corrections obtained from the tip calibration are then used for further computational data evaluation. The indentation hardness (HIT = Fmax/Ac) is calculated from the maximum force and the projected contact area and represents a measure of the resistance to plastic deformation. This value is convertible to HV (Vickers hardness). The indentation modulus (EIT) was then calculated from the slope of the tangent of the indentation depth-curve at maximum force [32].

Dynamic Mechanical Analysis (DMA)

The DMA analysis involved a quasistatic force applied in 20 steps varying in the load cycle from 10 mN to 500 mN. Upon reaching each step interval, a low magnitude oscillating force (1.0 Hz) was superimposed on the quasistatic force. The oscillation amplitude was set at 5 nm, so the sample deformation was kept within the linear viscoelastic regime. For each tooth substrate and treatment, 20 indentations were performed randomly.

For the used frequency (1.0 Hz), the force oscillation generates oscillations on the displacement signal with a phase angle δ. The sinusoidal response signal was then separated into real and imaginary parts representing the storage (E') and the loss moduli (E''), respectively. E' is a measure of the elastic response of material behavior, whereas E'', characterizes the viscous material behavior. The quotient E''/ E' is defined as the loss factor (tan δ) and is a measure of the material damping behavior.

4.2.6. Statistical analysis

Structural and compositional analyses of the materials were performed in triplicate and repeated at least three times. Results are reported as the mean of the three experiments ± 1 standard deviations.

EDS data of enamel and dentin surfaces were analyzed to compare the quantity of each element between the CaP-treated regions against negative control. One-way ANOVA and Tukey-Kramer's HSD multiple comparisons post-hoc tests were applied for $p < 0.05$.

Data regarding dentinal tubule opening areas obtained by FEG-SEM image analysis had a non-normal distribution. Therefore, they were analyzed by applying the Mann-Whitney U test comparing the opening area of CaP-treated regions vs. negative control and setting the significance level to $p < 0.05$.

Data were log-transformed for each microhardness parameter of the enamel surfaces, except tan δ, to approximate normal distribution. Data were first analyzed as overall means comparisons for the treatment groups on enamel and dentin using one-way ANOVA and Tukey-Kramer's HSD ($p < 0.05$). After that, curves were plotted considering the variation of each indentation parameter against the indentation depth using the locally estimated scatterplot smoothing (LOESS) method for regression, adjusting for alpha smoothing parameter (range: 0.5 - 0.65) and setting robustness to 1.0 on each parameter to re-weight and de-emphasize the points that are farther from the fitted curve. Confidence intervals of the estimate were also computed.

4.3. Results

4.3.1. CaP materials characterization

The PXRD patterns of CaP-N and CaP-S are reported in Figure 29A. Peak indexing shows that CaP-N is a biphasic mixture of 33 wt.% HA (ASTM Card file No. 00-009-0432) and 67 wt.%, β-TCP (ASTM Card file No. 00-009- 0169), as estimated by Rietveld refinement. For both CaP-N's crystalline phases, the diffraction peaks are narrow and intense, indicating a high level of crystallinity.

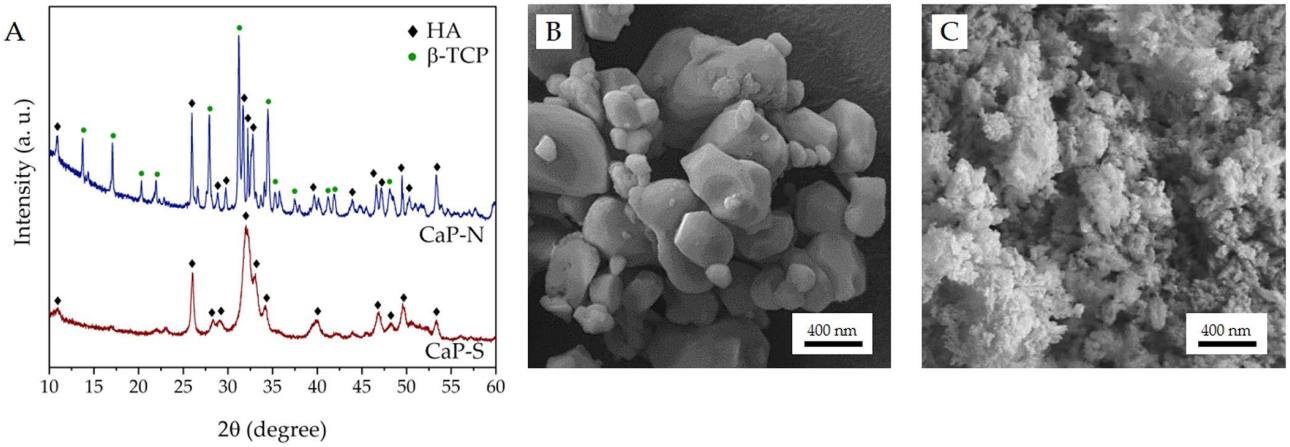

Figure 29. (A) PXRD patterns of CaP-N and CaP-S; (B-C) FEG-SEM micrographs of (B) CaP-N and (C) CaP-S.

CaP-S, on the other hand, is made of pure and stoichiometric HA, and its peaks are broad and poorly defined, indicating a low level of crystallinity and the presence of nanocrystals.

These observations were confirmed by FEG-SEM analysis (Figure 29B, C). Micrographs of CaP-N (Figure 29B) show that the material is composed of rounded particles ranging from 200 nm to 1 µm. In the case of CaP-S, micrographs (Figure 29C) illustrate that the material is composed of nanometric elongated particles, < 100 nm long and < 50 nm wide. Both sub-micrometric CaP-N and nanometric CaP-S particles tend to aggregate into micrometric grains when they are in a dry state.

The chemical composition of the two materials is reported in Table 24:

Table 24. Chemical composition of CaP samples.

	CaP-N	*CaP-S*
Ca *(Average ± SD wt.%)*	33.9 ± 0.9	34.6 ± 1.0
P *(Average ± SD wt.%)*	18.0 ± 0.6	16.1 ± 0.4
Mg *(Average ± SD wt.%)*	0.69 ± 0.02	0.14 ± 0.01
Ca/P *(mol/mol ± SD)*	1.46 ± 0.01	1.66 ± 0.01
(Ca + Mg)/P *(mol/mol ± SD)*	1.50 ± 0.02	1.67 ± 0.01

Both CaP-N and CaP-S are almost mainly composed of Ca and P, containing only traces of magnesium (< 1.0 or < 0.2 wt.%, respectively). The evolution over time of CaP-N and CaP-S as a concentrated slurry (25 wt.%) in neutral (pH 7.0) or acidic (pH 4.5) aqueous solutions was studied. Both materials increased the environmental pH in the acidic solution despite repeated washouts (Figure 30A). CaP-N neutralized the acidic solution, while CaP-S leveled at 6.0–6.5. When immersed in the pH 7.0 solution, the two materials showed a different behavior, as CaP-N raised the pH to ~ 11.0 while CaP-S did not alter the pH significantly (Figure 30B).

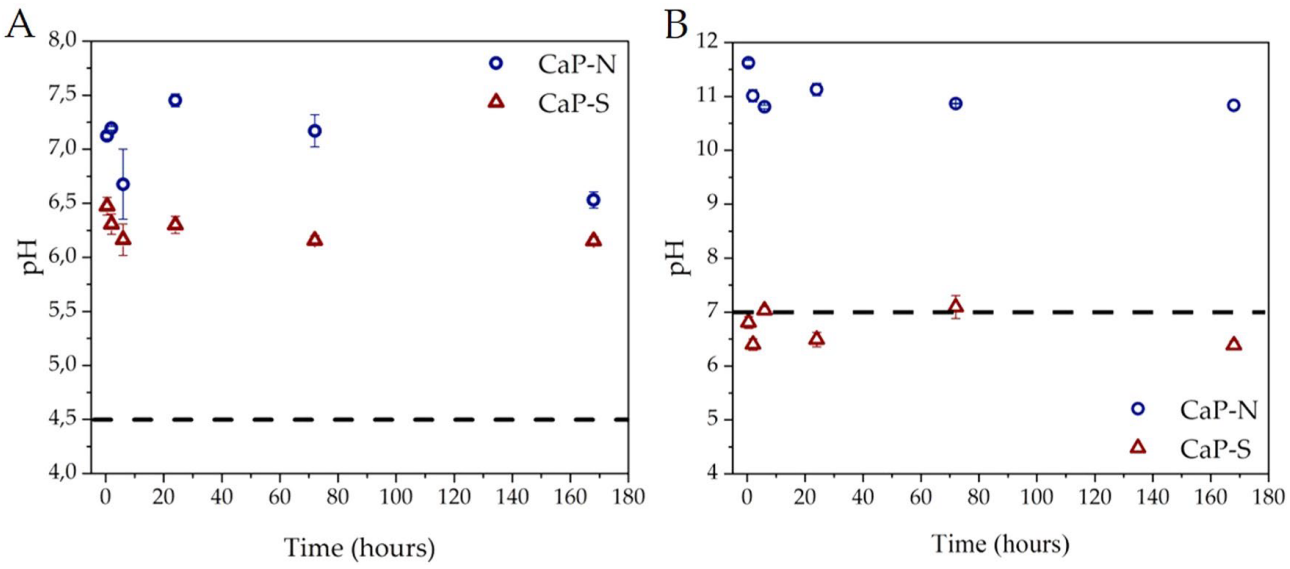

Figure 30. Evolution over time of pH in (A) acidic or (B) neutral solutions. The dashed line indicates the pH of the solutions after each refresh

Cumulative ion release curves of the sample slurries in the two solutions expressed as the absolute concentration of ions in the solution and as the weight percentage of ions released are reported in Figure 31. Unsurprisingly, Ca release (Figure 31A) was more intense when both CaP materials were in contact with the pH 4.5 solution than under neutral pH conditions.

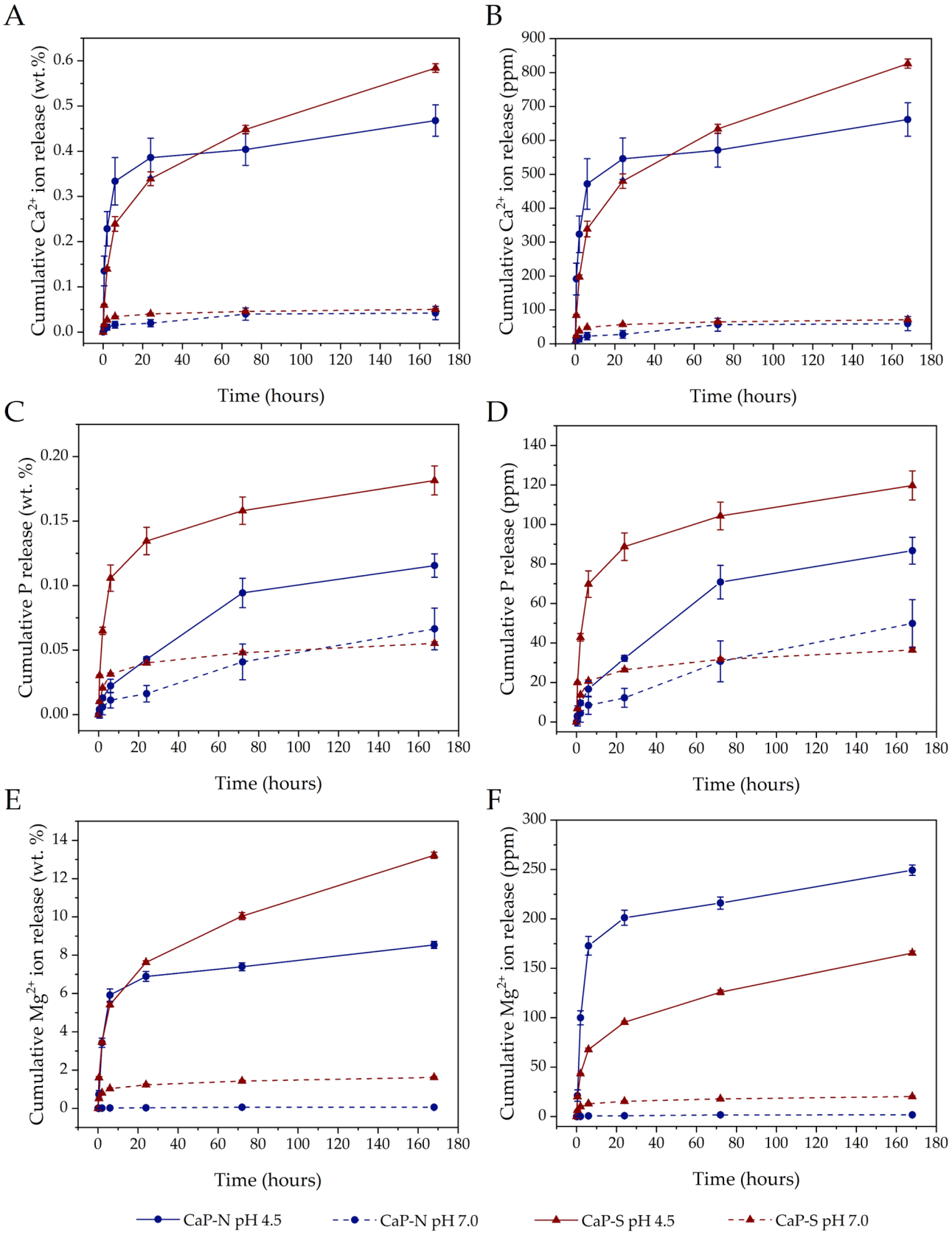

Figure 31. Cumulative ion release curves for (A, B) Ca, (C, D) P, and (E, F) Mg expressed as (A, C, E) relative weight percentage or as (B, D, F) absolute concentration (ppm)

CaP-N at pH 4.5 had a burst calcium release in the first 6h of incubation and then leveled off after 24h, while CaP-S release is less intense but steadier so that the release was still present after 7 days. At pH 7.0, the differences between materials were less evident, with a slightly higher Ca release for CaP-S. The P release (Figure 31B) was also pH-dependent and higher at acidic pH. Both CaP materials showed a relatively intense release of Mg compared to Ca and P, especially under acidic conditions (Figure 31C).

After 7 days of incubation, PXRD patterns (Figure 32A) and their Rietveld refinements show that the HA content of CaP-N increased while β-TCP content decreased independently from solution pH (Table 25).

Table 25. Crystal phase composition of CaP samples before and after incubation for 7 days in acidic or neutral solutions.

	pH	**HA** *(Average ± SD wt.%)*	**β-TCP** *(Average ± SD wt.%)*
CaP-N	As prepared	33.1 ± 0.4	66.9 ± 0.4
	4.5	43.2 ± 0.3	56.8 ± 0.3
	7.0	47.7 ± 0.3	52.3 ± 0.3
CaP-S	As prepared	100	/
	4.5	100	/
	7.0	100	/

In detail, CaP-N was composed by ca. 45 wt.% HA in comparison to 33 wt.% HA of the pristine material. CaP-S had no changes with incubation.

FEG-SEM micrographs of CaP-N after incubation (Figure 32B, C) showed that new nanometric particles ~ 100 nm long and 50 nm wide appeared onto CaP-N

independently from solution pH. In contrast, no significant morphological changes in CaP-S were observed (Figure 32D, E).

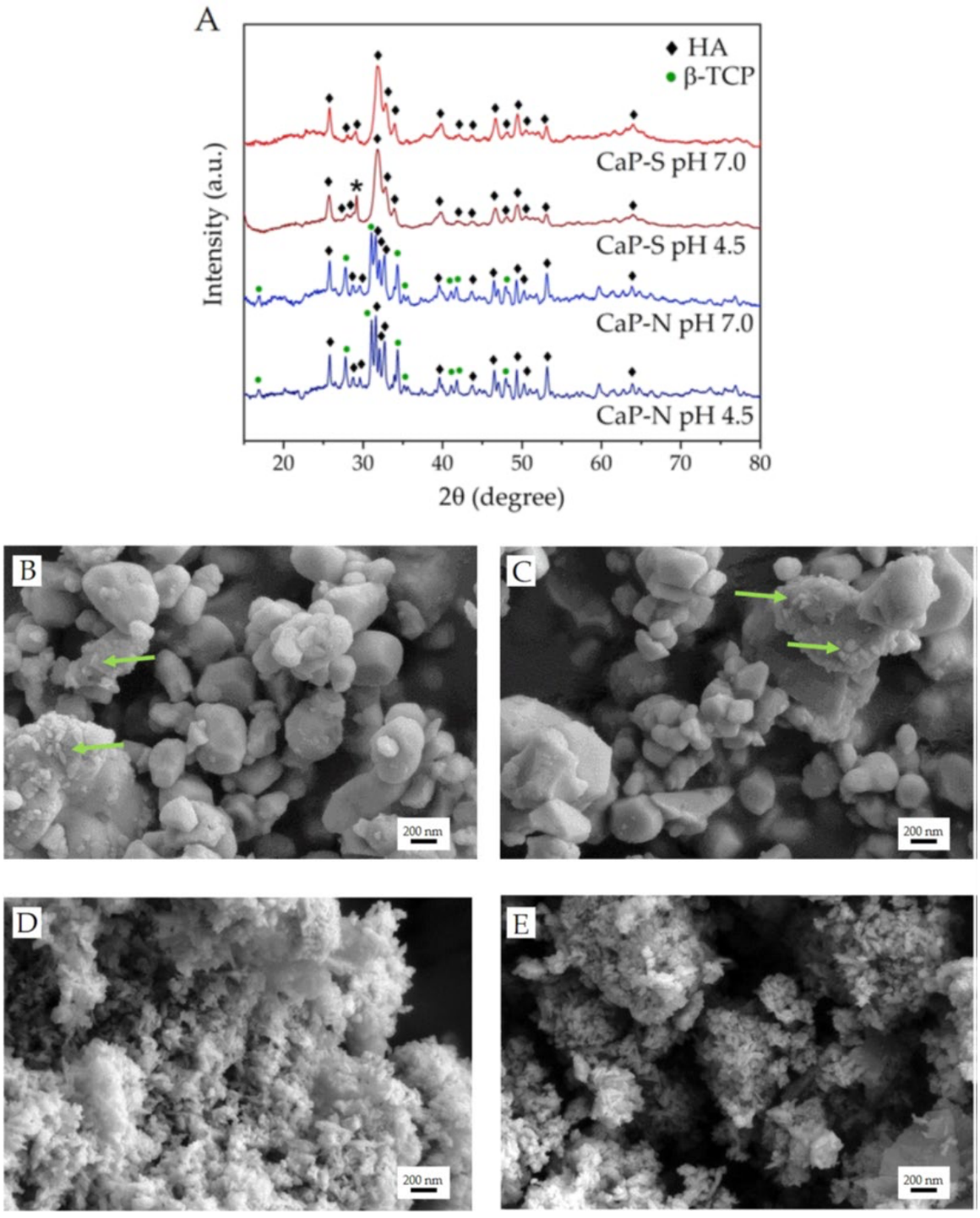

Figure 32. (A) PXRD patterns of CaP samples after 7 days of incubation in solutions at pH 4.5 or 7.0. The CaP-S samples exposed to the pH 4.5 buffer presented an additional diffraction peak (marked with an asterisk symbol) that might be related to crystalline lactate salts precipitated during incubation. (B-E) FEG-SEM micrographs of CaP-N after 7 days of incubation in (B) acidic or (C) neutral buffer in comparison to CaP-S after 7 days of incubation in (D) acidic or (E) neutral buffer. Green arrows in panels (B, C) highlight the newly formed nanoparticles.

4.3.2. Dentin tubules occlusion and enamel remineralization

Dentin tubules occlusion

FEG-SEM showed open and demineralized tubules in the negative control sample (Figure 33A, D). Single collagen fibrils can be discerned at higher magnification with their characteristic 67 nm-banded structure (Figure 33G). In contrast, dentin treated with CaP-N (Figure 33B, E) shows an almost complete occlusion of tubule openings. A similar result was obtained with CaP-S treatment (Figure 33C, F). The occlusion of dentinal tubule openings (Figure 33L) as quantified by digital image analysis showed an average tubule opening area of 4 - 8 μm2 (2 - 3 μm diameter) in the negative control, while for CaP-N, the opening area was reduced to 0.3 - 0.9 μm2 (0.6 - 1 μm diameter), indicating a statistically significant high occlusion ($p < 0.05$). CaP-S treated region had an opening area of 0.3 - 2.1 μm2, (0.6 - 1.6 μm diameter), showing a less intense occlusion compared to CaP-N ($p < 0.05$). High magnification micrographs of CaP-N treated samples (Figure 33H) showed the presence of two types of particles on the dentin surface: (i) rounded particles < 1 μm in size together with (ii) new small and irregular particles < 100 nm in size evenly covering the dentinal surface (marked in Figure 33H with a green and a light blue arrow, respectively). The high magnification micrographs of dentin after CaP-S treatment (Figure 33I) show that the dentinal surface is covered by nanoparticles.

FEG-SEM observation of fractured dentin specimens allowed to assess the penetration of CaP materials within the dentinal tubules (Figure 34). Control specimen tubules were found entirely open, where demineralization involved the first micrometers below the exposed surface (Figure 34A, D). CaP-N particles were found inside the tubules up to 4 μm depth. In addition, some sparse 1-2 μm thick mineral plugs could be observed obliterating tubule surface opening (Figure 34E). CaP particles and mineral plugs could also be seen in the dentin specimens treated with CaP-S (Figures 34C and F, respectively). In this case, the mineral plug was a deposition of CaP-S nanoparticles (marked by green arrows in Figure 34C, F).

The chemical composition of dentin surfaces was assessed through elemental quantification by SEM-EDS calibrated with a metallic Co NIST standard (Figure 35). This approach, previously used for chemical composition analysis of enamel surfaces treated with remineralizing toothpastes, provides a reliable elemental composition of the first micrometers of surface [5]. All specimens contained Ca, O, P, and C; in some cases, traces of Mg were also detected. Ca and P contents were shallow in the negative control, while a significantly higher amount was present in the regions treated with CaP-N ($p < 0.05$). The treatment with CaP-S induced a significant increase of Ca and P compared to the control, albeit to a lower extent than CaP-N ($p < 0.05$). The Ca/P ratio of the negative control dentin surface (Figure 35D) was 1.16, while CaP-treated samples had a ratio of 1.45 for CaP-N and 1.68 for CaP-S.

Regarding the mechanical behavior, the quasistatic indentation test determined the indentation hardness and indentation modulus (referred to as HIT and EIT, respectively). Both tested CaPs improved dentin's resistance to plastic deformation (Figure 36A-D). The improvement was depth-dependent, and the materials showed different behaviors.

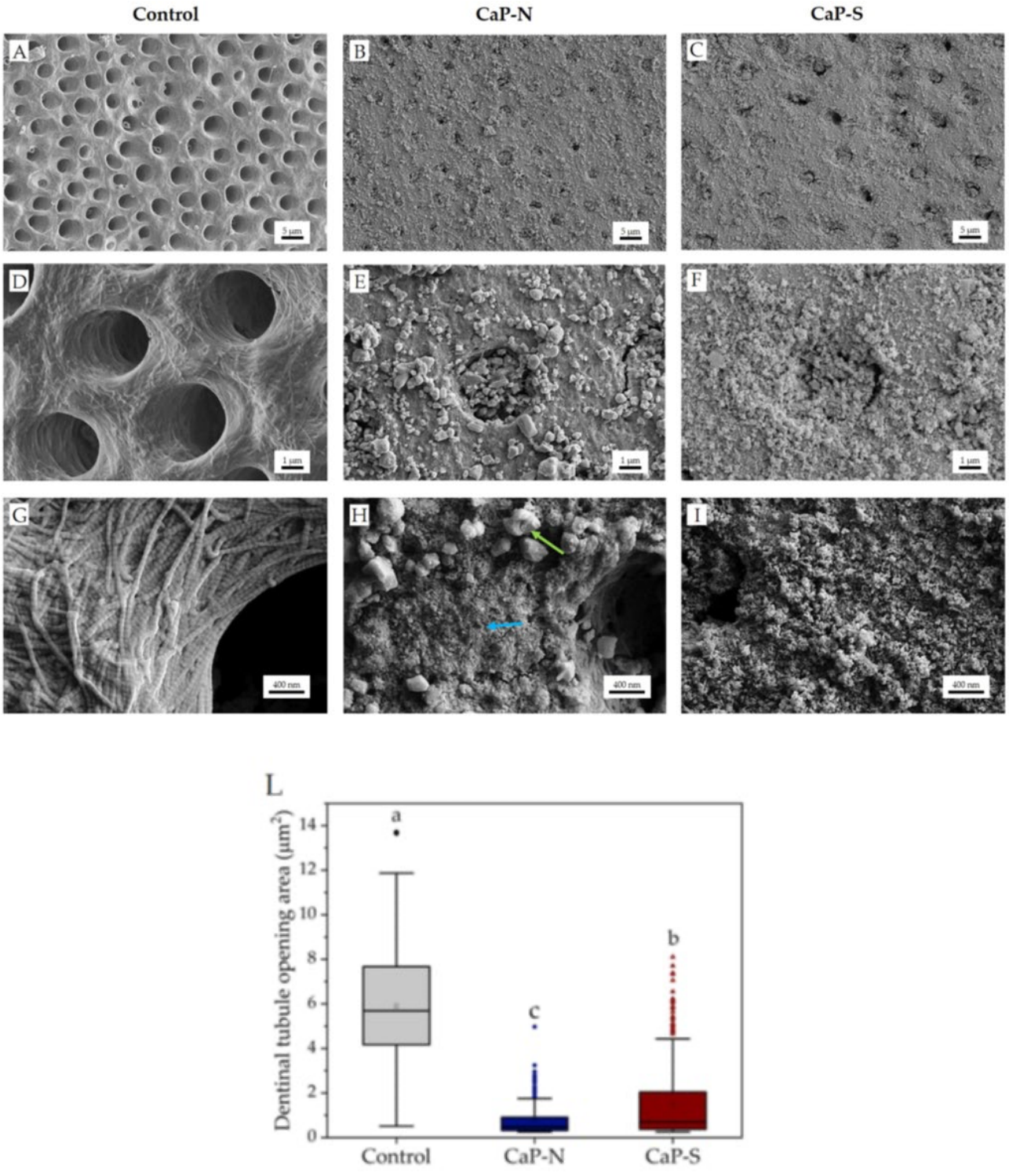

Figure 33. FEG-SEM micrographs of demineralized dentin surfaces after treatment with (A, D, G) water, (B, E, H) CaP-N and (C, F, I) CaP-S. (L) Tubule occlusion quantification by digital image analysis. The green arrow in panel (H) highlights CaP-N particles, while the light blue arrow highlights the newly formed mineral phase deposited onto the dentin surface. Different superscript letters in panel (L) represent statistically different groups ($p < 0.05$)

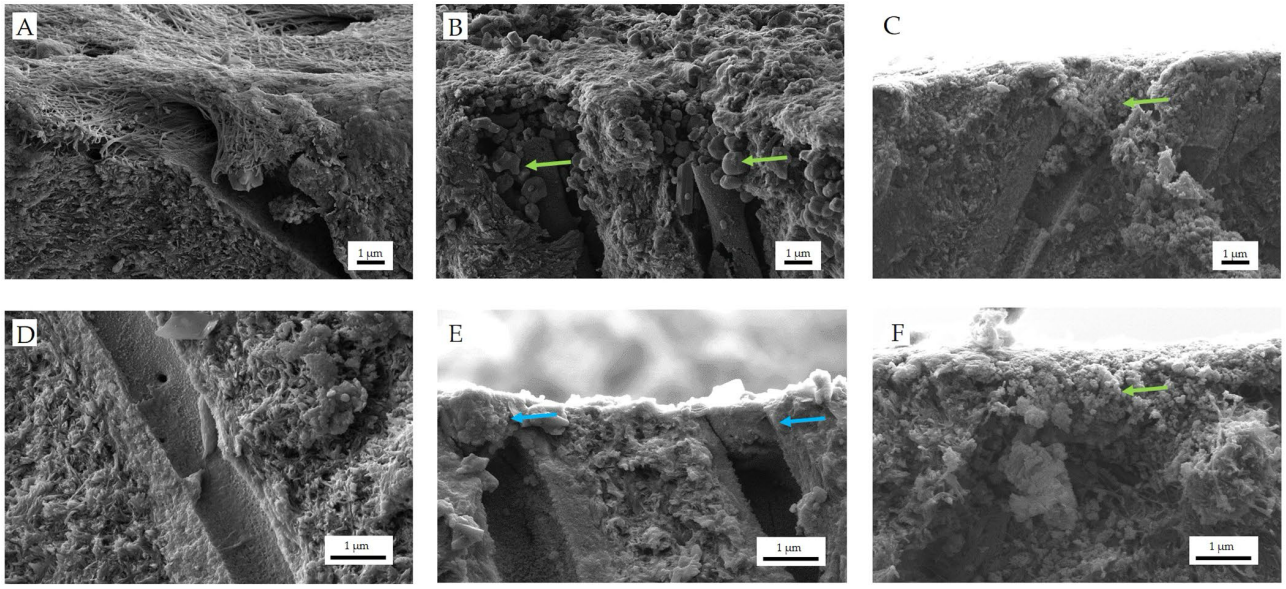

Figure 34. FEG-SEM micrographs of demineralized dentin sections after treatment with (A,D) water, (B,E) CaP-N and (C,F) CaP-S. Green arrows in panels (B, C, F) highlight the CaP particles deposited within dentinal tubules, while the light blue arrows in panel (E) highlight the newly-formed mineral plugs. In panel (B), the cylindrical residues of Tomes fibers present in dentin at the moment of treatment can be observed

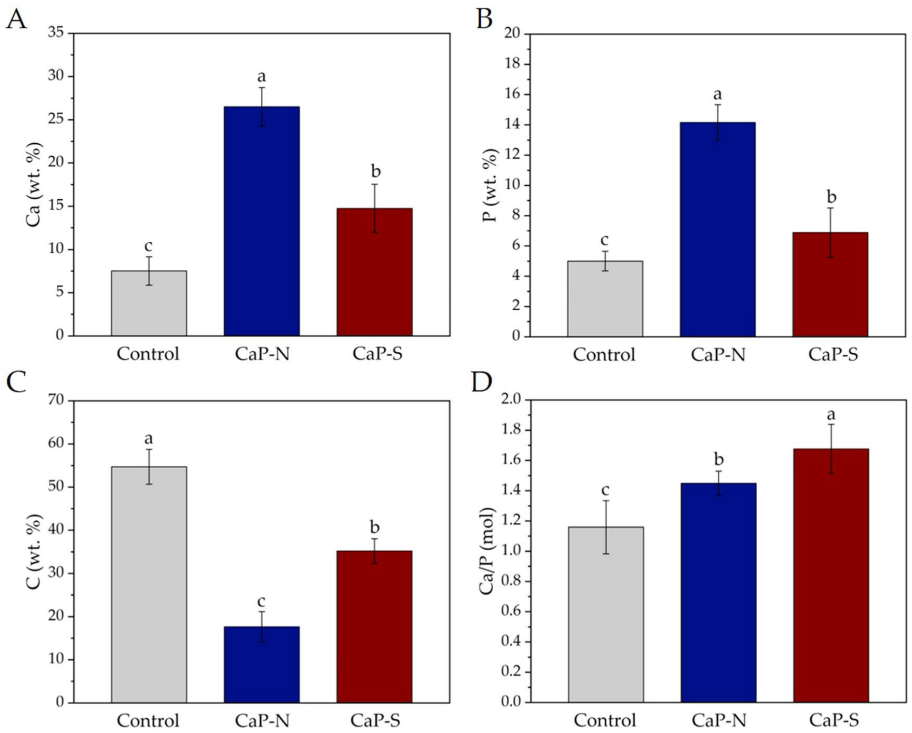

Figure 35. SEM-EDS measurement of (A) Ca and (B) P, and (C) C content and (D) Ca/P molar ratio of dentin surfaces after treatment. Different superscript letters in each panel represent statistically different groups ($p < 0.05$)

CaP-N increased HIT by about 50% compared to the negative control up to a depth of 6 μm (Figure 36A) and increased EIT by about 25% up to the same depth (Figure 36C). CaP-S showed the highest EIT value in the first 0.5 μm of depth, and for the following 2.5 μm of depth, a HIT and EIT higher than the negative control but lower than CaP-N (Figure 36A, C). At depths > 2.5 μm, there was no difference between CaP-S and control.

DMA was used to study the viscoelastic behavior of CaP-treated dentin compared to the negative control (Figure 36E-L). The storage modulus of dentin treated with the tested CaP materials in function of depth was similar to the indentation hardness curve (Figure 36E, F). Both treatments increased the storage modulus, with CaP-S showing a significant increase up to 2.5 μm depth, while CaP-N reached 6.5 μm. Both CaP treatments also significantly increased loss modulus up to 7 μm depth, and no significant difference between the behavior of the treatments was highlighted (Figure 36G, H). Regarding tan δ, CaP-N slightly decreased this parameter, while CaP-S slightly increased it compared to the negative control; this effect was not depth-dependent (Figure 36I, L).

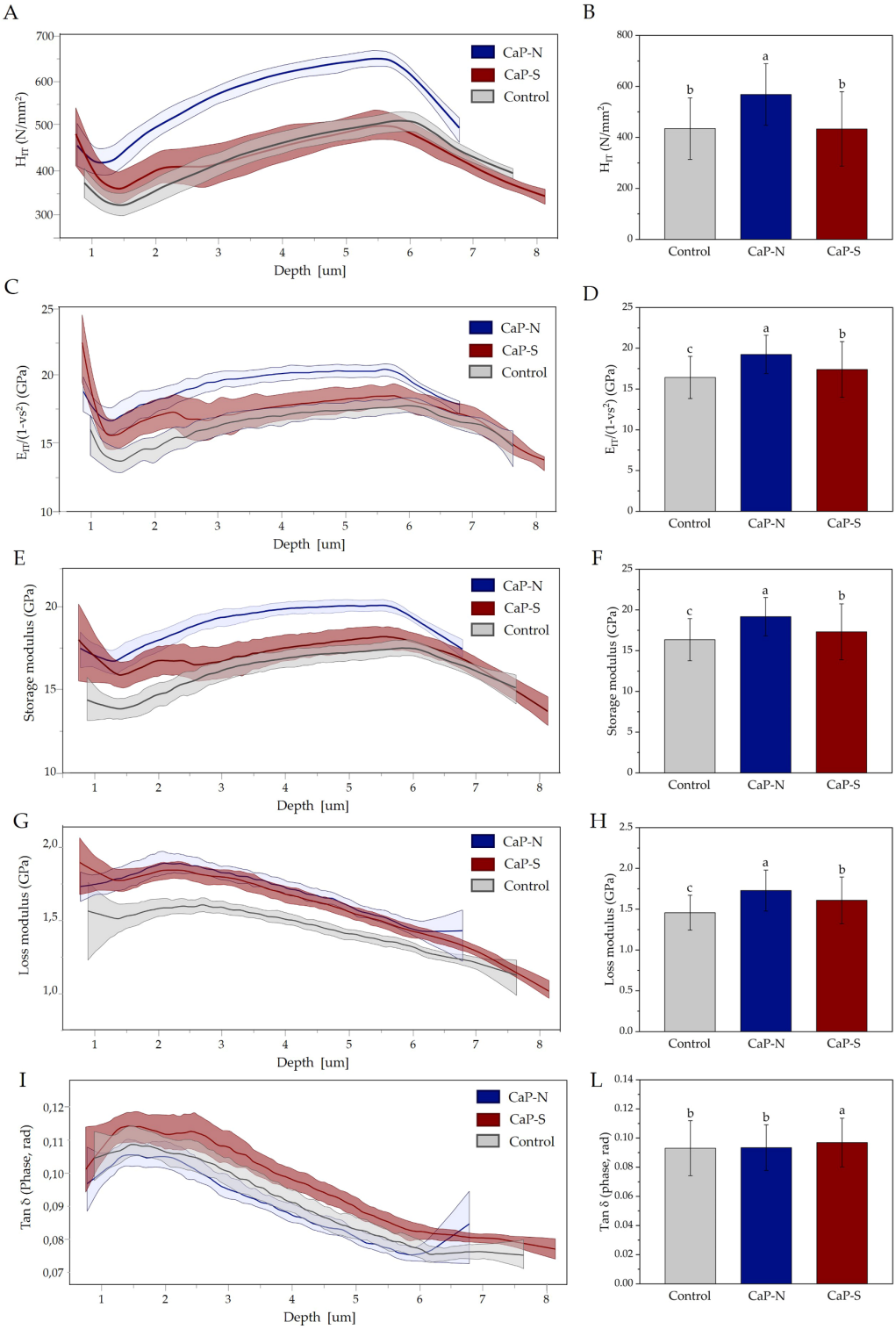

Figure 36. (A-D) Quasistatic indentation parameters of dentin surfaces after treatment. (A) Indentation hardness as a function of indentation depth and (B) average indentation hardness. (C) Indentation modulus as a function of indentation depth and (D) average indentation modulus. (E-L) Viscoelasticity parameters of enamel surfaces after treatment. (E) Storage modulus as a function of indentation depth and (F) average storage modulus. (G) Loss modulus as a function of indentation depth and (H) average loss modulus. (I) Tan δ as a function of indentation depth and (L) average tan δ. Different superscript letters in panels (B, D, F, G, L) represent statistically different groups. Note that panels show reverse-transformed data while statistics were performed on log-transformed data.

Enamel remineralization

FEG-SEM micrographs of the negative control show initial demineralization of the enamel surface (Figure 37A, D). At higher magnification, voids are formed between the prisms due to the dissolution of the interprismatic mineral phase, which is usually more prone to demineralization being less crystalline. After treatment with CaP-N (Figure 37B), the enamel surface displayed a continuous aspect without interprismatic voids.

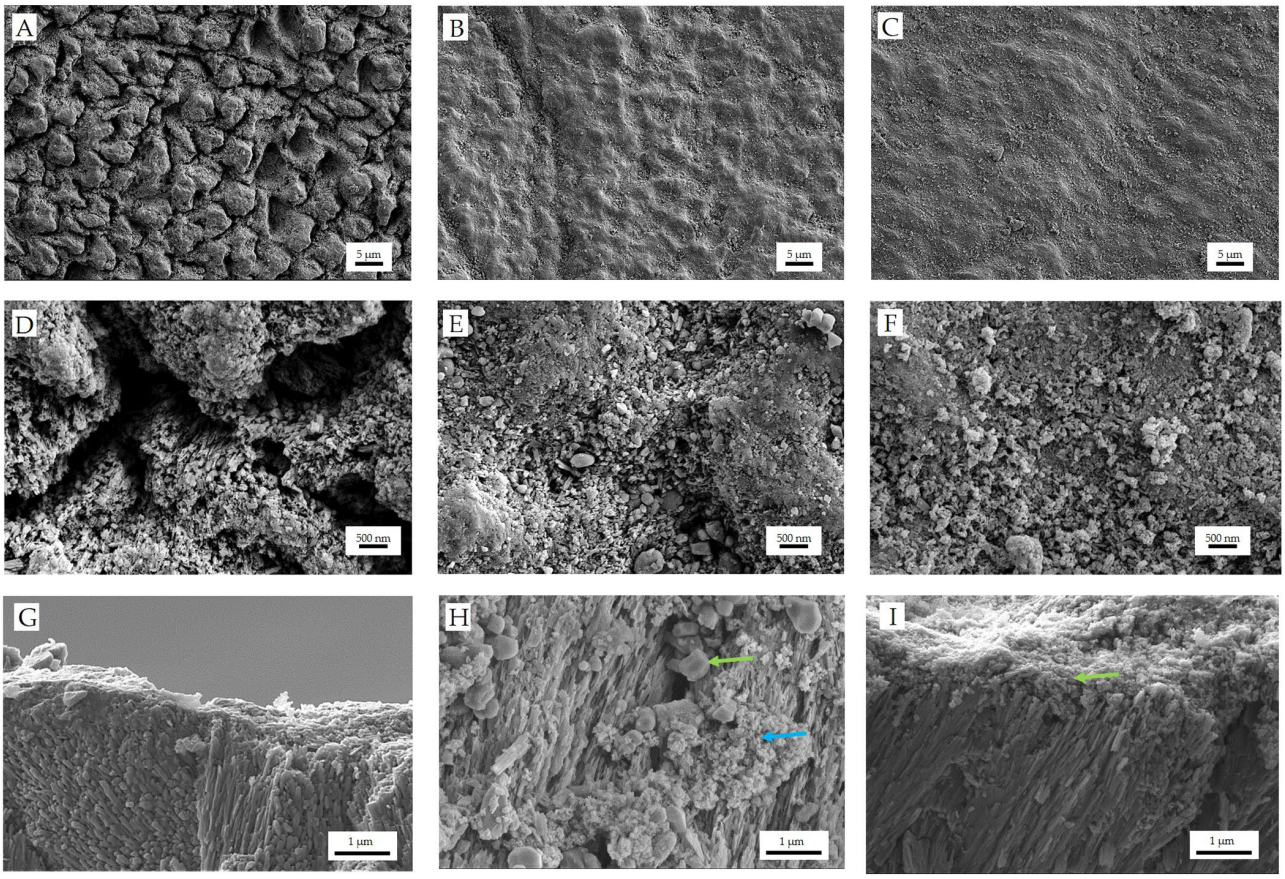

Figure 37. (A-F) FEG-SEM micrographs of the demineralized enamel surfaces after treatment with (A, D) water, (B, E) CaP-N, or (C, F) CaP-S. (G-I) Micrographs of demineralized enamel prism sections after treatment with (G) water, (H) CaP-,N, or (I) CaP-S. Green arrows in panels (H, I) highlight the CaP particles deposited within enamel prisms, while the light blue arrows in panel (H) highlight the newly-formed nanoparticles

High-magnification micrographs (Figure 37E) reveal the deposit of CaP-N particles and newly formed nanoparticles in the interprismatic region. A similar effect was observed after treatment with CaP-S (Figure 37C); in this case, the stoichiometric HA nanoparticles filled interprismatic voids and deposited onto the enamel surface (Figure 37F).

FEG-SEM micrographs of the sectioned enamel specimens are displayed in Figure 37G-I. The negative control showed the typical structure of enamel tissue (Figure 37G), including HA prisms arranged into staggered rows showing interlocking and offsetting of prism heads. CaP-N treated samples (Figure 37H) showed CaP-N particles deposited between prisms together with newly formed nanoparticles. The micrographs of CaP-S treated regions (Figure 37I) showed a similar outcome, with the deposition of nanoparticles mainly in the interprismatic space.

SEM-EDS (Figure 38) of the negative control mainly showed Ca, O, and P signals with traces of Mg. There was no statistically significant difference in Ca or P content between the control and treated surfaces ($p > 0.05$). Also, Ca/P molar ratios were not statistically different ($p > 0.05$).

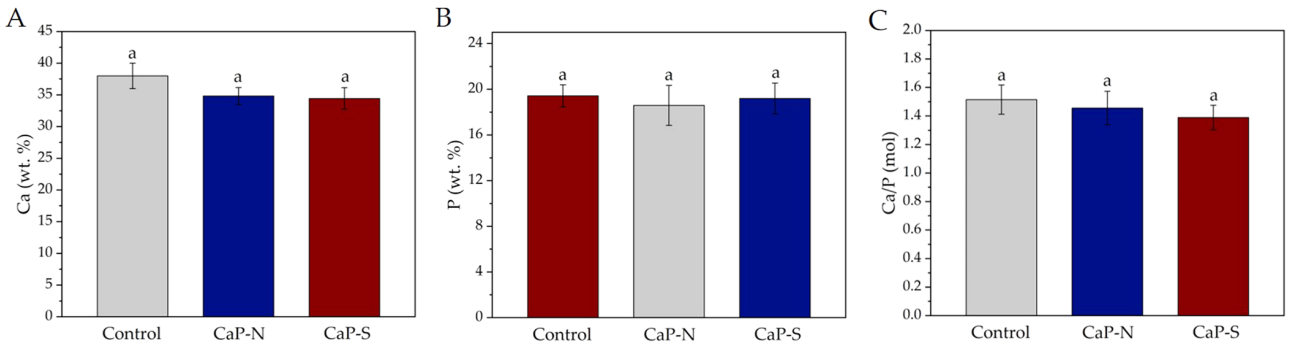

Figure 38. SEM-EDS measurement of (A) Ca and (B) P, and (C) Ca/P molar ratio of enamel surfaces after treatment. Different superscript letters in each panel represent statistically different groups ($p < 0.05$)

Hardness parameters of the quasistatic indentation test showed that both tested CaPs improved enamel's resistance to plastic deformation (Figure 39A-D), yet CaP-N had a distinctly higher effect than CaP-S up to 2.5 μm depth. The negative control showed an initial high hardness value at the enamel surface level (< 0.1 μm) and then swiftly decreased in the first 0.5 μm to be slowly restored, reaching 3.0 μm depth.

Similarly to HIT and EIT, both tested CaPs increased enamel storage modulus (Figure 39E, F). Both CaP treatments decreased the loss modulus compared to the negative control, with CaP-S producing a higher effect than CaP-N (Figure 39G, H). The consequence was that both CaPs sharply decreased the tan δ value compared to the control, flattening the tan δ curve concerning the probing depth (Figure 39I, L).

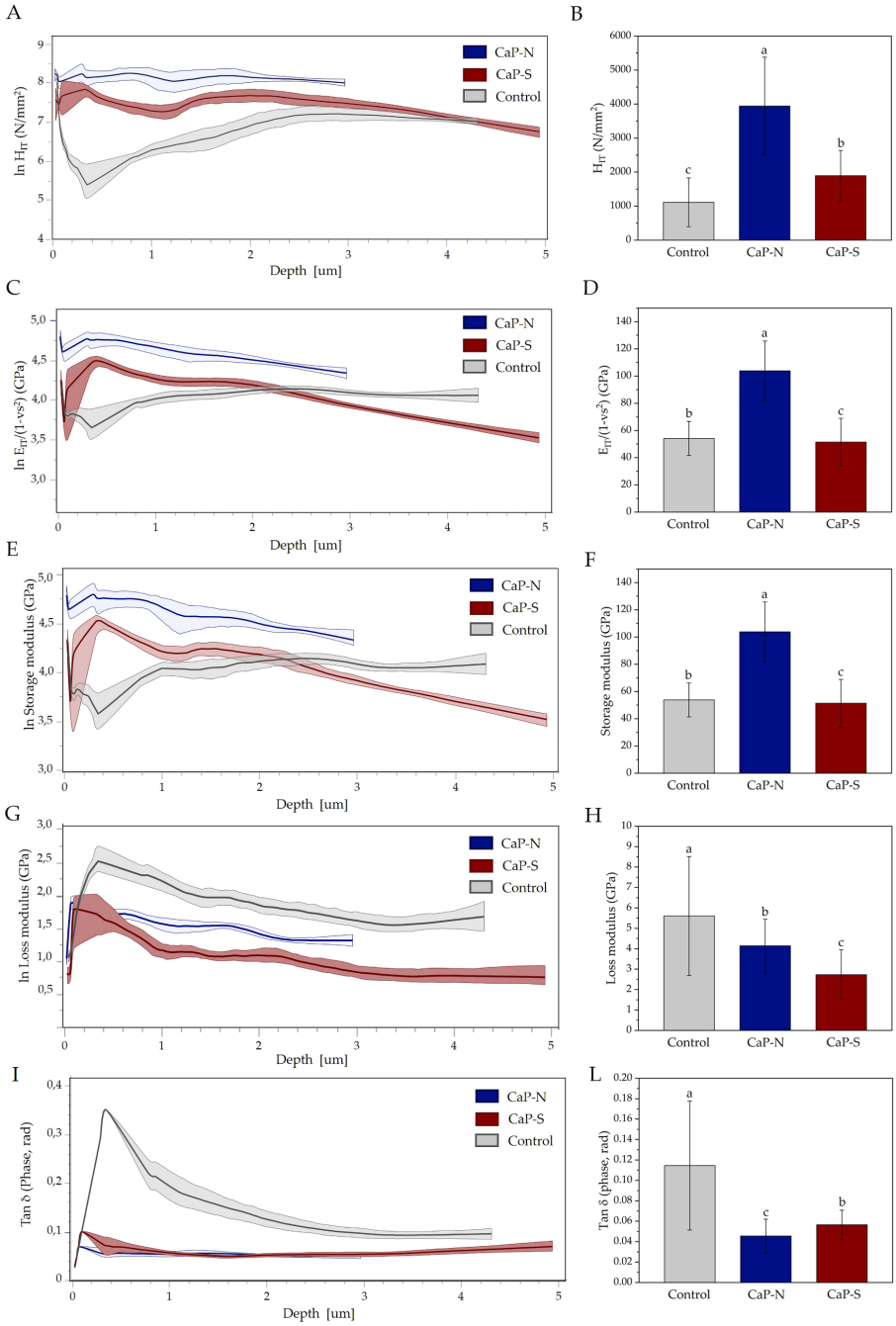

Figure 39. (A-D) Quasistatic indentation parameters of enamel surfaces after treatment. (A) Indentation hardness as a function of indentation depth and (B) average indentation hardness. (C) Indentation modulus as a function of indentation depth and (D) average indentation modulus. (E-L) Viscoelasticity parameters of enamel surfaces after treatment. (E) Storage modulus as a function of indentation depth and (F) average storage modulus. (G) Loss modulus as a function of indentation depth and (H) average loss modulus. (I) Tan δ as a function of indentation depth and (L) average Tan δ. Different superscript letters in panels (B, D, F, G, L) represent statistically different groups. Note that panels show reverse-transformed data while statistics were performed on log-transformed data

4.4. Discussion

The present work aimed to test a CaP material derived from fish industry circular economy to be used as dentine tubules occlusion and enamel remineralization agent.

The characterization of CaP-N showed that it occurs as a biphasic mixture of HA and β-TCP, confirming previous findings [18]. The presence of β-TCP is due to the calcination of fish bones' calcium-deficient biogenic HA (i.e., with a Ca/P molar ratio < 1.67), as at temperatures above 700°C Ca-deficient HA partially recrystallizes into the β-TCP phase, as widely reported in the literature [33]. Thermal treatment leads to the formation of a highly crystalline material characterized by a round particle morphology due to partial grain growth and sintering during the heating and to β-TCP recrystallization, in agreement with previous reports on the thermal treatment of fish bones [34]. In contrast, CaP-S is poorly crystalline and characterized by a nano-morphology that imparts a high specific surface area, typical of HA synthesized by wet precipitation in the selected conditions [35]. The Ca and P content and their molar ratio for CaP-N are in good agreement with the values reported for other thermally-treated fish bones [36, 37]. At the same time, Mg is more abundant in CaP-N than CaP-S as HA from marine biogenic sources is often cation-substituted [33]. Overall, material characterization revealed that CaP-N differed from stoichiometric nano-HA (CaP-S) in terms of particle size, morphology, crystallinity, and phase composition, suggesting that very different behavior may arise when these two materials are supplied to dental hard tissues.

CaP-N behavior in an acidic aqueous solution showed that it could efficiently buffer the acidic environment as effectively as CaP-S, stabilizing the pH at neutral values. It is well reported in literature that CaP materials dissolve at low pH, releasing PO_4^{3-} ions, which in turn form a phosphate buffer at pH ~ 6-7 [38]. This pH-dependent solubility is proved by the experiments of ions release. Over time, the ions release in the acidic solution tends to level off due to the increase of pH, which in turn decreases dissolution. Differently, in a neutral aqueous solution, CaP-S does not affect pH, while CaP-N

increases it significantly. This behavior may be attributed to the presence of traces of calcium oxide (CaO) on CaP-N particles' surface in amounts that cannot be detected by PXRD (< 0.5 wt.%). CaO formation is a by-product of thermal treatment of non-stoichiometric carbonate-doped apatites due to carbonate decomposition, and this occurrence has been previously reported for calcined pig bones [39,40]. In water, CaO hydrates to calcium hydroxide, which is a base. Hence, in water the increase of pH was likely due to the presence of CaO traces in the concentrated CaP-N suspension (25 wt.%). Nevertheless, an alkaline environment is not detrimental to dental tissues, as a comparable pH is generated by mineral trioxide aggregate (MTA), which is commonly used in endodontic treatment as a root repair material and does not cause harmful effects [41]. Moreover, due to CaO presence, CaP-N neutralizes the acidic solution to pH 7.0-7.5 while CaP-S buffers the pH at a lower value of 6.0-6.5.

The faster calcium release of CaP-N compared to CaP-S may be related to the presence of β-TCP phase, which is more soluble than HA and thus could release a significant amount of Ca^{2+} ions [22]. Because of β-TCP solubility, CaP-N quickly shifts solution pH to higher values than CaP-S. Regarding the relatively high Mg release of both CaP materials, we hypothesize that their Mg-rich regions dissolved preferentially, as Mg^{2+} distorts HA crystal lattice, decreasing crystallinity and thus resistance to acidic dissolution. It is of particular interest that CaP-N, after 7 days of incubation, had a lower β-TCP content and formed new nanoparticles independently from the solution pH. This data confirms a preferential dissolution of the more soluble β-TCP phase, in agreement with the literature [21], that induced the precipitation of new CaP minerals. In contrast, CaP-S did not show any significant change with incubation.

Based on these preliminary data, the behavior of CaP-N in terms of dentinal tubule occlusion and enamel remineralization was tested, using protocols and experimental conditions that simulated the clinical use as closely as possible. To compensate for the intrinsic variability of enamel and dentine surfaces and avoid using a high number of replicates, the three experimental groups (treatment with water/CaP-N/ CaP-S) have been applied randomly on separate regions of the same tooth slice. CaP-N treatment

led to an excellent occlusion of tubule openings and the formation of mineral plugs at the sub-surface level. This result indicates that the sub-micrometric granules of CaP-N (200 nm - 1 μm) are small enough to penetrate and occlude dentinal tubules, which usually range from 1 to 3 μm in size for tooth sections taken close to dentin-enamel junction [42]. In addition, the observation highlighted the presence of deposited CaP-N particles (rounded particles < 1 μm in size) together with a newly deposited nano-structured mineral phase. These small nanoparticles were not present in pristine CaP-N powder (Figure 29B) or in dentin (Figure 33A, D, G) but were very similar to the ones that formed when CaP-N was incubated in an aqueous slurry (Figure 32B, C). Therefore, it is likely that they have formed in situ. An interpretation is that during treatment, CaP-N particles adhered to the partially demineralized dentin, releasing Ca^{2+} and PO_4^{3-} ions over time, and then such ions interacted with the exposed collagen, inducing a new mineral phase deposition. This finding suggests that treatment with CaP-N can stimulate dentin remineralization. SEM-EDS data confirm the collagen-based dentin remineralization, as the negative control has a low Ca and P content and a high C content, mainly due to the exposed collagen. At the same time, these values are inverted after treatment with CaP-N. In addition, the fact that the Ca/P ratio of the dentin specimens treated with either CaP-N or CaP-S matches their respective Ca/P ratios confirms that the mineral observed in the outer dentin layer is primarily due to deposited CaP materials.

In the case of CaP-S, FEG-SEM, and SEM-EDS, data show that a carpet of nanoparticles evenly covers the dentinal surface. However, it is impossible to determine whether this mineral layer is due to the direct deposition of CaP-S nanoparticles or a new mineral phase induced by CaP-S. CaP-S treatment achieved a penetration depth comparable to CaP-N within dentin tubules and could induce the formation of mineral plugs, although with a slightly lower efficiency. These findings suggest that CaP-N and CaP-S might have different mechanisms of action when applied to dentin. In the case of CaP-N, its bigger particles can easily obstruct the tubule and get stuck in the first two microns of the tubule depth, as the tubule diameter

corresponds to the size of about 2-4 particles. Then, the release of ions stimulated the remineralization of the demineralized dentin tissue, inducing the formation of thick plugs. For CaP-S particles, their nanometric size may lead to a diffusion deep inside the tubule, which in turn achieves an overall lower tubule occlusion. However, if enough particles are repeatedly administered, they can effectively obstruct the opening and form a mineral plug over time.

All dentinal hypersensitivity treatments aim to close the exposed dentinal tubules quickly and permanently. However, if the intertubular dentinal collagen is not simultaneously remineralized, the exposed dentin may become a region of reduced hardness prone to mechanical failure [43]. For this reason, it is of paramount importance to look at the mechanical behavior of the dentin exposed to the remineralizing treatment to better understand the efficacy of such procedures. The microindentation data suggest that CaP-N and CaP-S could both improve dentin's mechanical characteristics. In particular, CaP-N provided a homogeneous increase of the tissue hardness as a function of dentin depth. In contrast, CaP-S provided a very high hardness increase at the dentin surface and within the first two micrometers of depth. Variations in the mechanical properties within the dentin, such as the ones found in the CaP-S treated samples, mean an increased risk of cracking and breakdown of the substrate when an external force is applied, as low modulus regions (below 2.5 μm) lead to energy concentration in high elastic modulus regions (above 2.5 μm) [44]. From this point of view, treatment with CaP-N might be considered a better choice over CaP-S since the latter may concentrate the stress at the very surface where the remineralizing layer is formed, posing a higher risk for fracture at the interface of the newly formed layer.

The viscoelastic behavior of CaP-treated dentin was studied using DMA, as it is a complex composite biomaterial exhibiting both viscous and elastic components when it undergoes deformation. The viscoelasticity of the bulk dentin matrix represents the interaction between the collagen fibrils, collagen crosslinking and density, associated proteoglycans, and the mineral phase [45, 46]. The first parameter is the storage

modulus, representing the material's ability to store energy elastically. Both CaP materials increased dentin's storage modulus, with CaP-N positively affecting deeper regions than CaP-S. This stiffening effect could result from the remineralizing activity by the tested treatments, leading to the precipitation of minerals inside the tissue, thus indicating that CaP-N also induced remineralization in deep dentin. On the other hand, the loss modulus represents the material's ability to dissipate stress (viscous behavior). The increase of loss modulus and, thus, the capability to dissipate mechanical energy by both CaP treatments could be due to a large interface area between the collagen fibrils and the newly formed mineral particles of the remineralized structures [47]. Finally, tan δ represents the ratio of the viscous to elastic response of the material, providing information on the overall damping ability or the capacity to absorb shock. The decrease of tan δ values induced by CaP-N treatment in comparison to negative control and the opposite increase by CaP-S can be attributed to particle size. Indeed, the damping behavior is related to the internal friction generated by grain or interphase relaxation, which in CaP-S offers a larger stress dissipation area due to the much smaller particle size than CaP-N. It has been reported that the dissolution of CaP compounds supplied to dentin creates an ions-rich environment that induces dentin remineralization, which is reflected in a decrease of tan δ and increased storage and loss modules in the material [48]. Therefore, a possible interpretation of the DMA data is that both tested CaPs induced nucleation and growth of nanocrystals into dentin, remineralizing it, and the treatment induced an excellent connection between the newly formed mineralized structures and the pristine tissue, in particular with the exposed collagen fibrils.

Altogether, data demonstrates that CaP-N is a very promising material for dentin remineralization and occlusion of dentinal tubules, improving the mechanical characteristics of the tissue. CaP-N treatment on dentin can be considered at least as effective as stoichiometric HA nanoparticles, which is an excellent material for this application. Future works will assess the effect of prolonged CaP-N treatments, evaluating the formation of the mineral plugs and their resistance to repeated acidic

lesions caused by physiological and pathological pH changes in the oral microenvironment. Moreover, the hydraulic conductance of dentine after long-term treatment with CaP-N should also be assessed to further corroborate the tubules occlusion efficacy.

The efficacy of CaP-N as a material for enamel remineralization was also evaluated. FEG-SEM observation indicated that the treatment, similarly to CaP-S, induced enamel remineralization by deposition into interprismatic defects and stimulated the formation of a new crystalline phase in direct contact with the pristine one.

Quasistatic indentation and DMA tests of the negative control showed that the maximal decrease in hardness and storage modulus was localized in a sub-surface zone within the first micrometer of depth. This observation matches clinical data on initial enamel demineralization lesions (white spots), where a demineralized sub-surface region can be observed underneath an otherwise intact superficial enamel layer. Both CaP materials and mainly CaP-N improved hardness parameters and storage modulus, showing that they could remineralize subsurface enamel layers. In addition, CaP treatments sharply decreased the enamel's tan δ values. Healthy, highly mineralized enamel has a tan $\delta < 0.1$; higher values indicate an excessive viscous behavior caused by demineralized tissue. Therefore, viscoelastic measurements indicate that both treatments could restore the subsurface enamel lesions by creating a structure that tightly connects with the pristine one, effectively remineralizing the tissue and restoring its mechanical characteristics. The generated enamel lesions had a shallow depth (≤ 3.0 μm) due to the demineralization protocol applied; thus, the lesion depth was shallower than dentin, possibly impacting the evaluation of the activity of the tested CaP materials. In future works, different demineralization protocols (e.g., 48h at pH 3.5-4.0 [49]) will be applied to test the efficacy of CaP materials on simulated early caries under conditions more closely resembling clinical ones.

In the present study, the experiments were designed to avoid specimen dehydration and consequent artifacts and misinterpretations when performing the microindentation measurements. Also, the choice of the storage medium (Dulbecco's modified PBS) was made to replicate conditions occurring in the external environment. Dulbecco's modified PBS more closely simulates such an environment compared to a simulated body fluid that is commonly used to test biomaterials' behaviour when placed inside the human body. For the same reason, specimens were observed without the use of any chemical fixation or collagen degradation inhibition, that would have affected the micromechanical parameters of the tested specimens. In the latter case, the instrumentation would have measured the effect of the fixative on the substrate rather than the effect of the tested treatments. It is clear from the results of the present study that mechanical characteristics differed between tested treatments in a depth-dependent manner. If surface degradation occurred, some difference would have been expected and noticeable in the depth profile as occurring on the outermost layers mainly.

4.5. Conclusions

Both CaP treatments possessed an excellent remineralizing behaviour for initial enamel lesions and dentinal tubules occlusion, and CaP-N has efficacy at least comparable to CaP-S. In addition, CaP-N, due to its different mode of action, could have an edge over CaP-S on dentin desensitization. These findings may suggest using different CaP-based remineralizing agents with tailored remineralization kinetics and mechanisms depending on the specific tissue requirements (i.e., dentine vs. enamel). The findings also show that biphasic calcium phosphate from fish bones, apart from being a more sustainable alternative material, could be a promising circular economy therapeutic agent for dental hard tissues due to its remineralizing and occlusive activity, which will be investigated more in future studies.

References

[1] James SL, Abate D, Abate KH, Abay SM, Abbafati C, Abbasi N, et al. Global, regional, and national incidence, prevalence, and years lived with disability for 354 diseases and injuries for 195 countries and territories, 1990–2017: a systematic analysis for the Global Burden of Disease Study 2017. Lancet 2018;392:1789–858.

[2] Neel EAA, Aljabo A, Strange A, Ibrahim S, Coathup M, Young AM, et al. Demineralization–remineralization dynamics in teeth and bone. Int J Nanomed 2016;11:4743–63.

[3] Fejerskov O., Nyvad B., Kidd E. Dental caries: the disease and its clinical management: John Wiley & Sons; 2015.

[4] García-Godoy F, Hicks MJ. Maintaining the integrity of the enamel surface: the role of dental biofilm, saliva and preventive agents in enamel demineralization and remineralization. J Am Dent Assoc 2008;139:25S–34S.

[5] Ionescu AC, Degli Esposti L, Iafisco M, Brambilla E. Dental tissue remineralization by bioactive calcium phosphate nanoparticles formulations. Sci Rep 2022;12(1): 16.

[6] Cochrane NJ, Cai F, Huq NL, Burrow MF, Reynolds EC. New approaches to enhanced remineralization of tooth enamel. J Dent Res 2010;89:1187–97.

[7] Sauro S, Spagnuolo G, Del Giudice C, Neto DMA, Fechine PB, Chen X, et al. Chemical, structural and cytotoxicity characterisation of experimental fluoridedoped calcium phosphates as promising remineralising materials for dental applications. Dent Mater 2023;39:391–401.

[8] Carella F, Degli Esposti L, Adamiano A, Iafisco M. The use of calcium phosphates in cosmetics, state of the art and future perspectives. Materials 2021;14:6398.

[9] Enax J, Epple M. Synthetic hydroxyapatite as a biomimetic oral care agent. Oral Health Prev Dent 2018;16:7–19.

[10] Melo MAS, Guedes SFF, Xu HHK, Rodrigues LKA. Nanotechnology-based restorative materials for dental caries management. Trends Biotechnol 2013;31: 459–67.

[11] Steinert S, Zwanzig K, Doenges H, Kuchenbecker J, Meyer F, Enax J. Daily application of a toothpaste with biomimetic hydroxyapatite and its subjective impact on dentin hypersensitivity, tooth smoothness, tooth whitening, gum bleeding, and feeling of freshness. Biomimetics 2020;5:17.

[12] Russ W, Meyer-Pittroff R. Utilizing waste products from the food production and processing industries. Crit Rev Food Sci Nutr 2004;44:57–62.

[13] Terzio˘glu P, ¨O˘güt H, Kalemtas¸ A. Natural calcium phosphates from fish bones and their potential biomedical applications. Mater Sci Eng: C 2018;91:899–911.

[14] Caldeira C, De Laurentiis V, Corrado S, van Holsteijn F, Sala S. Quantification of food waste per product group along the food supply chain in the European Union: a mass flow analysis. Resour Conserv Recycl 2019;149:479–88.

[15] Ohtake H, Tsuneda S. Phosphorus recovery and recycling. Springer,; 2019.

[16] Ferraro V, Carvalho AP, Piccirillo C, Santos MM, Castro PM, Pintado ME. Extraction of high added value biological compounds from sardine, sardine-type fish and mackerel canning residues—A review. Mater Sci Eng: C 2013;33:3111–20.

[17] Rustad T. Utilisation of marine by-products. Electron J Environ Agric Food Chem 2003;2:458–63.

[18] Adamiano A, Fellet G, Vuerich M, Scarpin D, Carella F, Piccirillo C, et al. Calcium phosphate particles coated with humic substances: a potential plant biostimulant from circular economy. Molecules 2021;26:2810.

[19] Adamiano A, Carella F, Degli Esposti L, Piccirillo C, Iafisco M. Calcium phosphates from fishery byproducts as a booster of the sun protection factor in sunscreens. ACS Biomater Sci Eng 2022.

[20] Falini G, Basile ML, Gandolfi S, Carella F, Guarini G, Degli Esposti L, et al. Natural calcium phosphates from circular economy as adsorbent phases for the remediation of textile industry wastewaters. Ceram Int 2022.

[21] Ebrahimi M, Botelho MG, Dorozhkin SV. Biphasic calcium phosphates bioceramics (HA/TCP): concept, physicochemical properties and the impact of standardization of study protocols in biomaterials research. Mater Sci Eng: C 2017;71:1293–312.

[22] LeGeros R, Lin S, Rohanizadeh R, Mijares D, LeGeros J. Biphasic calcium phosphate bioceramics: preparation, properties and applications. J Mater Sci: Mater Med 2003;14:201–9.

[23] Mathirat A, Dalavi PA, Prabhu A, GV YD, Anil S, Senthilkumar K, et al. Remineralizing potential of natural nano-hydroxyapatite obtained from epinephelus chlorostigma in artificially induced early enamel lesion: an in vitro study. Nanomaterials 2022;12:3993.

[24] Devitasari SP, Hudiyati M, Anastasia D. Effect of hydroxyapatite from waste of tilapia bone (Oreochromis niloticus) on the surface hardness of enamel. J Phys: Conf Ser: IOP Publ 2019:012009.

[25] Razali R, Rahim N, Zainol I, Sharif A. Preparation of dental composite using hydroxyapatite from natural sources and silica. J Phys: Conf Ser: IOP Publ 2018: 012050.

[26] Adamiano A, Sangiorgi N, Sprio S, Ruffini A, Sandri M, Sanson A, et al. Biomineralization of a titanium-modified hydroxyapatite semiconductor on conductive wool fibers. J Mater Chem B 2017;5:7608–21.

[27] Coelho A. Topas Academic V5. Coelho Softw 2012.

[28] Degli Esposti L, Ionescu AC, Carella F, Adamiano A, Brambilla E, Iafisco M. Antimicrobial activity of remineralizing ion-doped amorphous calcium phosphates for preventive dentistry. Front Mater 2022;9:846130.

[29] Degli Esposti L, Ionescu AC, Brambilla E, Tampieri A, Iafisco M. Characterization of a toothpaste containing bioactive hydroxyapatites and in vitro evaluation of its efficacy to remineralize enamel and to occlude dentinal tubules. Materials 2020;13 (13).

[30] Ahmed T, Mordan N, Gilthorpe M, Gillam D. In vitro quantification of changes in human dentine tubule parameters using SEM and digital analysis. J Oral Rehabil 2005;32:589–97.

[31] Schindelin J, Arganda-Carreras I, Frise E, Kaynig V, Longair M, Pietzsch T, et al. Fiji: an open-source platform for biological-image analysis. Nat Methods 2012;9: 676 82.

[32] Standardization IOf. Metallic materials: instrumented indentation test for hardness and materials parameters. Test Method: ISO 2015.

[33] Boutinguiza M, Pou J, Comesa˜na R, Lusqui˜nos F, De Carlos A, Le´on B. Biological hydroxyapatite obtained from fish bones. Mater Sci Eng: C 2012;32:478-86.

[34] Piccirillo C, Adamiano A, Tobaldi DM, Montalti M, Manzi J, Castro PML, et al. Luminescent calcium phosphate bioceramics doped with europium derived from fish industry byproducts. J Am Ceram Soc 2017;100:3402–14.

[35] Dorozhkin SV. Nanosized and nanocrystalline calcium orthophosphates. Acta Biomater 2010;6:715–34.

[36] Ideia P, Degli Esposti L, Miguel CC, Adamiano A, Iafisco M, Castilho PC. Extraction and characterization of hydroxyapatite-based materials from grey triggerfish skin and black scabbardfish bones. Int J Appl Ceram Technol 2021;18:235-43.

[37] Carella F, Seck M, Degli Esposti L, Diadiou H, Maienza A, Baronti S, et al. Thermal conversion of fish bones into fertilizers and biostimulants for plant growth–A

low tech valorization process for the development of circular economy in least developed countries. J Environ Chem Eng 2021;9:104815.

[38] Meyer F, Enax J, Epple M, Amaechi BT, Simader B. Cariogenic biofilms: development, properties, and biomimetic preventive agents. Dent J 2021;9:88.

[39] Merry J, Gibson I, Best S, Bonfield W. Synthesis and characterization of carbonate hydroxyapatite. J Mater Sci: Mater Med 1998;9:779–83.

[40] Sobczak-Kupiec A, Wzorek Z. The influence of calcination parameters on free calcium oxide content in natural hydroxyapatite. Ceram Int 2012;38:641–7.

[41] Torabinejad M, Parirokh M. Mineral trioxide aggregate: a comprehensive literature review—part II: leakage and biocompatibility investigations. J Endod 2010;36: 190–202.

[42] Mj¨or I, Nordahl I. The density and branching of dentinal tubules in human teeth. Arch Oral Biol 1996;41:401–12.

[43] Marshall G, Habelitz S, Gallagher R, Balooch M, Balooch G, Marshall S. Nanomechanical properties of hydrated carious human dentin. J Dent Res 2001;80: 1768–71.

[44] Misra A, Spencer P, Marangos O, Wang Y, Katz JL. Micromechanical analysis of dentin/adhesive interface by the finite element method. J Biomed Mater Res Part B: Appl Biomater: J Soc Biomater Jpn Soc Biomater Aust Soc Biomater Korean Soc Biomater 2004;70:56–65.

[45] Farina AP, Vidal CM, Cecchin D, Aguiar TR, Bedran-Russo AK. Structural and biomechanical changes to dentin extracellular matrix following chemical removal of proteoglycans. Odontology 2019;107:316–23.

[46] Matos AB, Reis M, Alania Y, Wu CD, Li W, Bedran-Russo AK. Comparison of collagen features of distinct types of caries-affected dentin. J Dent 2022;127: 104310.

[47] Caridade SG, Merino EG, Alves NM, de Zea Bermudez V, Boccaccini AR, Mano JF. Chitosan membranes containing micro or nano-size bioactive glass particles: evolution of biomineralization followed by in situ dynamic mechanical analysis. J Mech Behav Biomed Mater 2013;20:173–83.

[48] Toledano M, Osorio E, Aguilera FS, Osorio MT, Toledano R, L´opez-L´opez MT, et al. Dexamethasone and zinc loaded polymeric nanoparticles reinforce and remineralize coronal dentin. A morpho-histological and dynamic-biomechanical study. Dent Mater 2023;39:41–56.

[49] Sfalcin RA, da Silva JVP, Pessoa VO, Santos J, Olivan SRG, Fernandes KPS, et al. Remineralization of early enamel caries lesions induced by bioactive particles: an in vitro speckle analysis. Photo Photodyn Ther 2019;28:201–9.

CHAPTER V: WASTEWATER TREATMENT

5.1. Introduction

Textile industry is a primary source of water pollutants and is the main responsible for the release of ecotoxic dyes in water bodies [1]. During processing, up to 15% of used dyes can be released into wastewaters and discharged in the environment. Dyes used in the textile industry are of particular concern for their very long persistence, as most of them are by-design highly soluble in water, and very sturdy to discoloration, photodegradation, oxidation and microbial attack [2, 3] as they contain chromogenic-chromosphere structures which are difficult to biodegrade [4]. Moreover, textile dyes and their intermediate degradation products can be toxic to aquatic life and human health, as some are carcinogenic and mutagenic with potential for bioaccumulation [5].

Treatments aiming to decolour dye-containing effluents by conventional physical-chemical and biological processes are often ineffective [6]. This led to the study of new and more effective treatments for the decontamination of dye-containing wastewaters, such as adsorption, coagulation, precipitation, filtration, electro-dialysis, and membrane separation. Since adsorption prevents the formation of dyes' by-products, is easily applicable on a large scale and is more economically viable with respect to the other techniques, it is one of the most investigated approaches [7].

Many materials characterized by high specific surface areas (SSA) such as zeolites, silica and activated carbon have been used for dyes' adsorption from wastewaters [8–10].

This chapter has been published as "Falini G., Basile M. L., Gandolfi S. et al., "Natural calcium phosphates from circular economy as adsorbent phases for the remediation of textile industry wastewaters", in Ceramics International, 49 (2023) 243 – 252.

Among these, calcium phosphates (CaPs) in the form of hydroxyapatite ($Ca_{10}(PO_4)_6(OH)_2$, HA) nanoparticles (NPs) have been indicated as a cost-effective adsorbent phase al biocompatibility and its ubiquity through the biosphere [12], and is employed for several applications, including environmental remediation. In fact, HA NPs have been already employed for the decontamination of heavy metal polluted wastewaters and sites [13], and for the removal of dyes commonly used in the textile industry [4].

HA has been also reported as photocatalyst for the removal of organic dyes like methylene blue both in the form of non-stoichiometric HA, and in combination with photocatalytic materials like titanium dioxide [14, 15]; however, it is more frequently employed as adsorbent phase [16]. In this respect, the application of HA for the adsorption of cationic and anionic dyes such as brilliant green, malachite green and rhodamine B on one side, and reactive acid blue, congo-red, methyl blue and methyl yellow on the other, has been extensively investigated [4]. In these works, HA is prevalently of synthetic origin and often in the form of nanocomposites with metals or metallic ions, graphene, and synthetic or natural polymers such as chitosan, poly-lactic acid, carboxymethyl cellulose and acrylamide [17, 18]. Other works explored the possibility to use HA or other CaPs deriving from food by-products - such as fish bones, bovine bones or pig bones - as adsorbent phases for water remediation, but most of them are focused on the immobilization of heavy metals such as lead and cadmium [19], while only a few investigated the adsorption of textile dyes [20]. H. Hossini et al. (2017) reported on the use of a composite made of chitosan and bone char (i.e., a material obtained from the pyrolysis of animal bones containing CaPs) for the removal of anionic textile dyes from water, without giving any information on the quantity nor on the physical-chemical properties of the CaPs in it (e.g., CaP phase, particles size etc.) [20]. On the other hand, Miyah et al. extensively investigated the adsorption of brilliant green by HA extracted from fish bones, reporting large amount of data on the obtained material [21]. However, the SSA and degree of carbonation reported in this work are not in line with what reported in the literature on CaPs obtained by thermal

treatment of bones at high calcination temperatures (>800°C). Fish bones and bone meal are cheap sources of natural CaPs from circular economy as the food industry produces large amounts of them. In Europe, about 5.2 Mt per year of fish by-products are produced, posing serious environmental and economic issues to the fish industry that has to manage their appropriate disposal. In the case of bone meal, more than 18.0 Mt are produced yearly, with the majority being destined to thermal waste treatment plants producing CaPs-rich ashes destined to landfill [22]. In such a context, it is of fundamental importance to find new applications of CaPs recovered from animal bones so to reduce waste amount by valorising at the same time abundant by-products [23].

Biological CaPs can have different physical-chemical properties between them and with respect to synthetic ones, especially in relation to the source (i.e., mammalian or fish bone) and to the extraction process employed [24, 25]. Thus, it is of fundamental importance to determine the main process parameters that can affect the performance of CaPs produced by thermal treatment of food by-products in view of the envisioned application.

In this work, we investigated the possibility to use natural CaPs thermally extracted from different kinds of animal bones as adsorbent phases for the removal of the anionic dye copper phthalocyanine tri-sulfonic acid – also known as acid blue 185 (AB-185) - from water at different pH, and compared the results with those obtained using synthetic HA. AB-185 was chosen as model compound for two main reasons. Firstly, it is one of the most frequently employed dyes all over the world for textiles such as silk, polyamide fibres, wool and modified acrylics, especially in Asia where wastewaters contaminated by it are often discharged in rivers and other superficial water bodies, creating severe environmental problems [26]. Secondly, adsorption of this family of dyes by different adsorbent phases has been already investigated by several works in the literature [16, 27-29]; hence, the interaction between acid blue dyes and different materials is known.

Physico-chemical characteristics of synthetic CaPs (CaP-S), CaPs from fish bones (CaP-FM) and CaPs from bone meal (CaP-BM) were determined, and the mechanism of adsorption of AB-185 on them was investigated by conducting equilibrium and kinetic studies.

Finally, this study compares the performance in terms of textile dyes adsorption of synthetic and natural CaPs and identify the most critical production process parameters and physical-chemical properties of CaPs extracted from different kinds of bones (i.e., a mixture of bovine and porcine bones, and fish bones), giving indications for future studies on the application of CaPs from circular economy for wastewaters treatment.

5.2. Materials & methods

Calcium hydroxide ($Ca(OH)_2$, purity ≥ 95.0%), *phosphoric acid* (H_3PO_4, purity 80%), *sodium acetate anhydrous* (CH_3COONa, ReagentPlus®, purity ≥ 99.0%), *glacial acetic acid* (CH_3CO_2H, ReagentPlus®, purity ≥ 99%), *sodium hydrogen carbonate* ($NaHCO_3$, ACS reagent, purity ≥ 99.7%), *sodium carbonate* (Na_2CO_3, ACS reagent, anhydrous, purity ≥ 99.5%), *sodium hydroxide* (NaOH, ACS reagent, purity ≥ 97.0%) and *hydrochloric acid* (HCl, ACS reagent, 37%) were supplied by Sigma- Aldrich (St. Luis, MO, USA). All the solutions were prepared with *ultrapure water* (18.2 MΩ × cm, 25°C, Arium© pro, Sartorius, Gottingen, Germany). The textile dye *AB-185* was supplied in the form of sodium salt by Shandong Zhi Shang Chemical Co. Ltd (Tianjin, China) while *fish bones* (*Salmon salar*) and *bone meal* (mixed bovine and porcine bones) were supplied by a local enterprise.

5.2.1. Preparation of CaPs from fish bones and bovine bones

Natural CaPs were prepared following the procedure already described in a previous paper, with some minor modifications [30]. Briefly, fish bones (FB) and bone meal (BM) are dried at 120°C overnight in a ventilated oven and heated by a 120°C/h thermal ramp followed by a 1h isotherm at 800°C in an electric furnace (Nannetti – model KL 20/13, Faenza, Italy). The materials are cooled at RT and grinded with a planetary ball mill (MMS S.r.l. and Nannetti, Faenza, Italy) as follows. Briefly, 200 g of calcined materials are placed in a jar with 300 mL of Millipore water and 500 g of alumina grinding balls with a ∅ between 1.0 and 1.5 cm, and then the planetary ball mill is actioned for 30 min. Grinding balls are removed and the solution is poured in a 1.0 L beaker and left still until powder sedimentation. After removing the water on the top, the powder is placed in a ventilated drier at 105°C overnight and sieved through a stainless-steel sieve with a 450 mesh (32.0 μm). The obtained materials are named below as CaP-FM and CaP-BM and correspond to the CaP obtained from calcination of FB and BM, respectively.

5.2.2. CaPs synthesis

Synthetic CaP (CaP-S) were obtained by modifying a previously reported method [31]. Briefly, 10.0 g of $Ca(OH)_2$ (purity 95.0%) are added to 100 mL of Millipore water under constant stirring at 300 rpm for 30 min. A water solution obtained adding 8.87 g of H_3PO_4 (85.0 wt%) to 30 mL of deionized water is added drop-wise into the $Ca(OH)_2$ suspension to reach a final pH in the range between 6.5 and 7.0. The solution is left aging at room temperature for 3h, then the powder is recovered by centrifugation, rinsed three times with water and left in a ventilated oven at 40°C overnight. Before any use, the material grinded in an agate mortar and sieved through a stainless-steel sieve with a 450 mesh (32.0 μm).

5.2.3. Characterization of obtained CaPs

Sample morphology was evaluated with a scanning electron microscopy with a field-emission microscope (*FEG-SEM*, mod. ΣIGMA, ZEISS NTS Gmbh, Oberkochen, Germany). The preparation of powdered samples consisted in their deposition on a carbon tape mounted on an aluminium SEM stub and sputter coated (Polaron E5100, Polaron Equipment, Watford, Hertfordshire, UK) with 10 nm of gold to improve the electrical conductance. Accelerating voltage in the range between 3.0 and 5.0 keV was used to observe samples in the secondary electron imaging mode.

Thermal Gravimetric Analysis (*TGA*) was performed to quantify volatile and/or decomposable substances contained in the sample with a STA 449 Jupiter (Netzsch GmbH, Selb, Germany) instrument. 10.0 mg of powdered samples were heated from room temperature (RT) to 1100°C under air flow with a heating rate of 10°C/min in an alumina crucible.

Fourier transform infrared spectroscopy analyses in attenuated total reflection mode (*FTIR-ATR*) were carried out using a Nicolet iS5 spectrometer (Thermo Fisher Scientific Inc., Waltham, MA, USA) with a resolution of 1 cm^{-1} by accumulation of 16 scans covering the 4000 to 400 cm^{-1} range, using a diamond ATR accessory model iD7.

Dynamic Light Scattering (*DLS*) analyses were performed by using a Zetasizer Nano instrument ZSP (Malvern Instruments, UK). For the analysis, samples were dispersed in water at a concentration of 0.5 mg/mL at pH7.0. ζ-potentials were quantified by laser Doppler velocimetry as electrophoretic mobility at 25 ◦C using a disposable electrophoretic cell (DTS1061, Malvern Ltd., Worcestershire, UK) of three separate measurements (maximum 100 runs each).

Particle size distribution of powdered samples was determined by using a *Sedigraph5100 III plus* (Micromeritics, USA). The instrument exploits an X-ray which passes through the sample and moves vertically, evaluating the particles from the largest and heaviest ones up to the smallest and best dispersed ones. Sample preparation consisted of dispersing 3.5 g in approximately 80.0 mL of hexametaphosphate (Calgon) followed by ultrasound treatment with a sonication probe set at 50% amplitude for 3'.

The elemental composition was determined using inductively coupled plasma optical emission spectrometry (*ICP-OES*) on a Liberty 200 spectrometer (Agilent Technologies 5100 ICP-OES, Santa Clara, CA, USA Varian, Palo Alto, USA). Samples preparation was achieved putting 10 mg of each powdered sample in 50 mL of 2.0 wt% HNO_3 solution. Atomic emission of the main elements composing the samples was measured at the following wavelengths: 422.673 nm for Ca, 213.618 nm for P and 279.553 nm for Mg.

Specific surface area (SSA) of samples was measured through N_2 gas adsorption modelled by the Brunauer–Emmett–Teller (*BET*) method using a Surfer instrument (Thermo Fisher Scientific Inc., Waltham, MA, USA).

Finally, X-Ray Diffraction (*XRD*) analysis was performed using a DS Advance Diffractometer (Bruker), equipped with a Lynx-eye position sensitive detector, with a CuKα radiation (λ = 1.54178 Å), at 40.0 kV and 40.0 mA. XRD patterns were acquired in the 10-60° 2θ range at step size of 0.02°, and a scanning speed of 0.5 s. Phase identification was performed through Rietveld refinement using the software TOPAS5. The weight composition of the phases was refined considering a multiphase system,

using tabulated atomic coordinates of hydroxyapatite (ASTM Card file No. 00-009-0432), and β-TCP (ASTM Card file No. 00-009- 0169). The crystallinity degree of samples was calculated according to equation 4:

$$Cristallinity\ [\%] = 100\frac{C}{A+C}$$

Equation 4. Calculation of the degree of crystallinity

where C was the sum of peaks area and A was the area between peaks and background in the diffraction pattern [32].

5.2.4. Colorant adsorption on CaPs

The adsorption study was performed in two main steps: kinetic and isothermal adsorption. Moreover, both kinetic and isothermal adsorption were conducted in water and in 0.1 M acetate and carbonate buffer at pH values of 5.5 and 9.0, respectively. Finally, kinetic adsorption curves were fitted using the common models of pseudo first/second-order kinetics, while the isothermal adsorption curves, were fitted using Langmuir, Freundlich and Langmuir-Freundlich common models.

5.2.5. Kinetic adsorption of AB-185 on CaPs

The kinetic adsorption of AB-185 on CaPs was performed putting in contact 5.0 mL of a 0.1 mg/mL AB-185 solution at different starting pH with 20.0 mg of different materials (CaP-S, CaP-FM and CaP-BM). The suspension was kept in a horizontal shaker at RT. After several time points ranging from 5' to 1h, CaPs were separated by centrifugation (6000 rpm, 1') and the amount of AB-185 was determined analysing the supernatant by UV-Vis spectrophotometry (UV/Vis Perkin Elmer Lambda 35, and NanoDrop OneC, Thermo Fisher Scientific). The obtained curves were fitted with pseudo-first order and pseudo-second order kinetic models in order to better understand the adsorption mechanism of AB-185 on CaPs. In detail, the pseudo first-order model considers the reversibility of the adsorption, and the direct proportionality between the dye adsorption rate on the substrate depending on time and the difference among the amount of dye adsorbed at equilibrium and the amount already adsorbed, according to equation 5:

$$Q(t) = Qads,e[1 - e^{(-k1 \cdot t)}]$$

Equation 5. Pseudo first-order kinetic model

where *Q(t)* and *Qads,e* represent the amount of dye adsorbed per unit weight of sorbent (mg/g) at time t and at equilibrium, respectively, and *k1* parameter consists in the pseudo first-order adsorption rate coefficient (t^{-1}) [33].

The pseudo second-order kinetic model, instead, assumes that the rate-limiting step is chemisorption. According to this model, adsorption rate does not depend on the adsorbate concentration, but on the availability of adsorption sites on the substrate, and that the interaction between adsorbate and adsorbent is not reversible [34]. This model is described by equation 6:

$$Q(t) = Qads,e[1 - (\frac{1}{1 + k2 \cdot t})$$

Equation 6. Pseudo second-order kinetic model

where *k2* represents the pseudo second-order adsorption rate coefficient (t^{-1}).

5.2.6. Isothermal adsorption of AB-185 on CaPs

Isothermal adsorption was carried out putting in contact 20 mg of CaPs with 5 mL of a buffered solution of AB-185 at several concentrations (0.05, 0.5, 1, 5 mg/mL). Contact time was set at 30' based on the results obtained by the kinetic adsorption study. CaPs were separated by centrifugation (6000 rpm, 5') and the amount of AB-185 was determined analyzing the supernatant by UV-Vis. The curves were fitted to Langmuir, Freundlich and Langmuir- Freundlich models. Langmuir model (Equation 7) assumes four hypotheses:

- solid particles are characterized by a limited adsorption capacity.
- all the adsorption sites could be considered identical.
- each site retains only one molecule of the given compound.
- all sites are energetically and sterically independent from the adsorbed quantity [35].

$$Q = Qm\,[Klf \cdot Ce/(1 + Klf \cdot Ce)]$$

Equation 7. Langmuir model equation for isothermal adsorption

in which *Q* is the quantity of molecules adsorbed per unit weight of the sorbent (mg/g), *Ce* is the equilibrium concentration of adsorbate in solution (mg/mL), *Qm* is the maximum loading capacity (mg/g), and *Klf* is Langmuir affinity constant (mL/mg).

Freundlich model (Equation 8) considers the adsorption as non-ideal and reversible, and it is not only restricted to the formation of the monolayer. This model could be applied to multilayer adsorption systems, which are characterized by a non-uniform distribution of adsorption sites and affinities over a heterogeneous surface.

$$Q = Kf \cdot Ce \cdot e^{1/n}$$

Equation 8. Freundlich model equation for isothermal adsorption

in which *Kf* represents Freundlich affinity constant (mL/mg), while *Ce* is the same as described above, and n is the heterogeneity parameter.

Finally, Langmuir-Freundlich model combines the two models above described, and it is commonly used to predict heterogeneous adsorption systems (Equation 9).

$$Q = Qm\frac{(Klf \cdot Ce)^n}{1 + (Klf \cdot Ce)^n}$$

Equation 9. Langmuir-Freundlich model equation for isothermal adsorption

in which *Klf* represents Langmuir-Freundlich affinity constant (mL/mg), and *Qm*, *Ce* and *n* remain the same as the original models. In particular, the coefficient *n* can give information on the heterogeneity of the surface and on the positive or negative cooperativity between adsorbed molecules.

5.3. Results

5.3.1. Chemical-physical characterization of CaPs

CaPs samples were characterized from the physical-chemical point of view before being used for dye adsorption experiments. The XRD patterns reported in Figure 40(a) have all distinctive features. The diffraction pattern of synthetic CaP-S is that of a typical poorly nanocrystalline HA obtained at low temperature by wet precipitation, and is featured by broad peaks corresponding to the diffraction signals of HA reference pattern (ASTM Card file No. 00-009-0432). The signals of the diffraction profile of CaP-BM also match those of HA reference pattern, but in this case, peaks are more intense, sharp and resolved. Hence, both CaP-S and CaP-BM consist of pure HA, and the difference in their XRD patterns is ascribable to a different degree of crystallinity of the materials, the former being poorly crystalline and the latter being a thermally annealed highly crystalline HA, respectively.

The XRD profile of CaP-FM is different from those recorded for the other samples and indicates that the sample is made of a bi-phasic mixture of β-tricalcium phosphate (β-TCP, β-$Ca_3(PO_4)_2$, ASTM Card file No. 00-009-0169) and HA in a 1:1 ratio as quantified by Rietveld refinement. As for CaP-BM, the sample is more crystalline respect to CaP-S as a consequence of the thermal treatment to which bones undergo to extract the mineral component, but it is less crystalline respect to CaP-BM as denoted by the higher full width at half maximum (FWHM) of the main peaks. To summarize, CaP-S and CaP-BM consist of single-phase HA while CaP-FM is made of a 1:1 HA: β-TCP biphasic mixture, the three samples having different crystallinity degree, calculated as in equation 4) as follows: CaP-BM (77.0%) > CaP-FM (67.0%) > CaP-S (55.0%).

ATR spectra are reported in Figure 40(b). Briefly, the spectra of CaP-S and CaP-BM are similar while that of CaP-FM is significantly different, confirming the results of the XRD analysis. More in details, the spectrum of CaP-S is featured by a poorly resolved

and intense band centred around 1000 cm^{-1} ascribable to the asymmetric stretching mode ($v_3(PO_4)^{3-}$) and to the symmetric stretching mode ($v_1(PO_4)^{3-}$) of HA phosphate tetrahedron. This feature is typical of ATR spectra of nanocrystalline HA synthesized at RT. In the case of CaP-BM signals are more resolved, with a sharper band centred at 962 cm^{-1} related to the v_1 stretching mode of PO_4^{3-}, and a signal at 1090 cm^{-1} appearing as a shoulder in the spectrum of CaP-S and here appearing as a resolved although small band. Another difference respect to CaP-S can be observed in the region between 700 and 500 cm^{-1}, where a band centred at around 600 cm^{-1} occurs only in the spectrum of CaP-BM, and can be ascribed to the bending mode ($v_4(PO_4)^{3-}$) of HA [36]. The last difference among these two spectra is relative to the two carbonate bands centred at 875 and 1400 cm^{-1}, which are more intense in the case of CaP-S. All these differences are easily explained by the fact that differently from CaP-S, CaP-BM was obtained by thermal treatment of bones at 850°C. This treatment leads to the thermal annealing of the material, making it crystalline, and to the partial removal of carbonates inside HA structure, as carbonate losses start to occur at temperatures above 700°C [37].

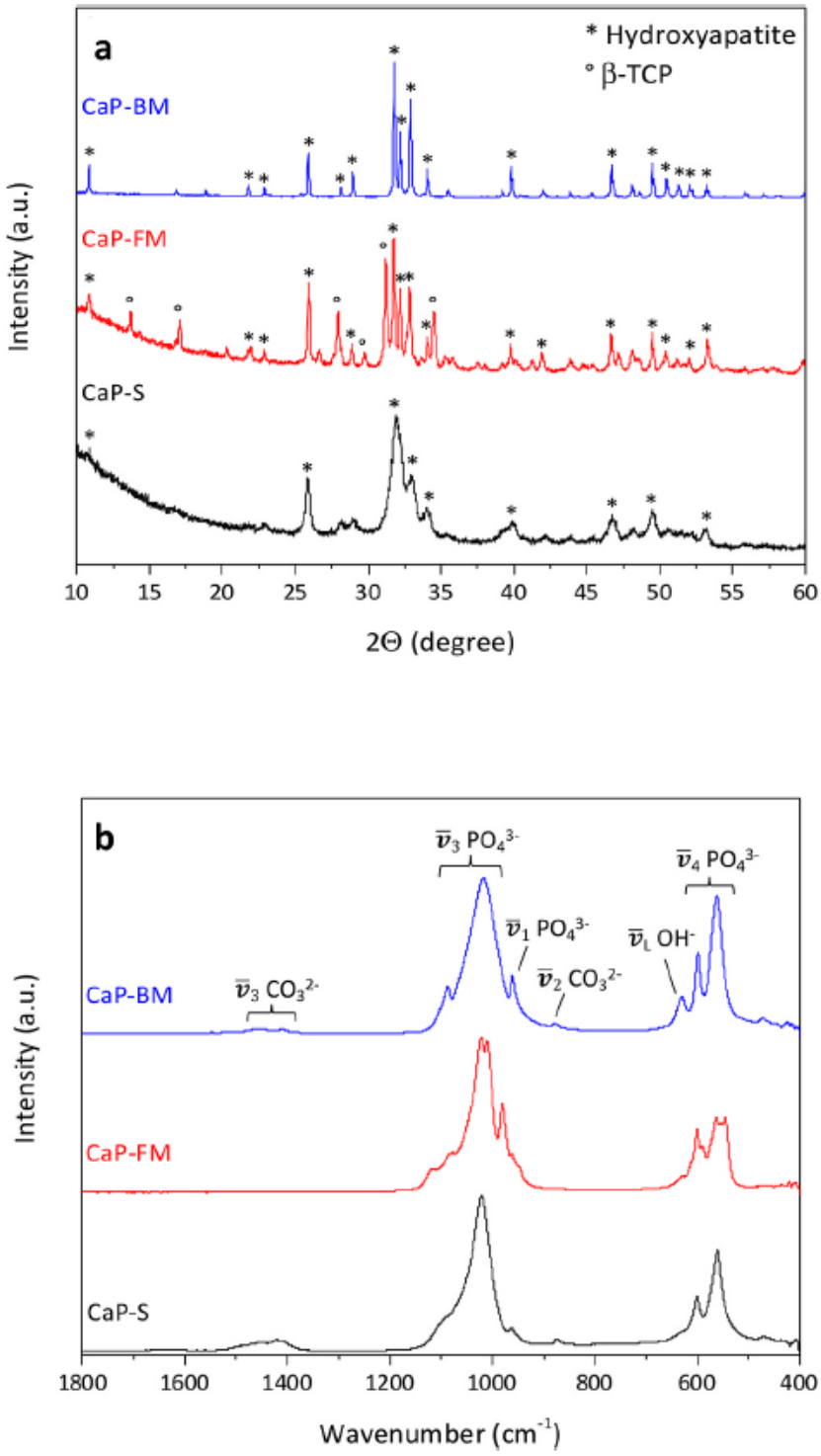

Figure 40. XRD patterns (A) and FT-IR analysis (B) of – from the top to the bottom – CaP-BM, CaP-FM and CaP-S.

The ATR spectrum of CaP-FM is typical of a biphasic mixture of HA and β-TCP, and is characterized by a main band in the region between 900 and 1200 cm^{-1} ascribable to the asymmetric and antisymmetric stretching mode of the phosphate tetrahedron of

both phases. In this region in fact, many signals not ascribable to pure HA can be observed, confirming the occurrence of more than one phase. More in details, the spectrum is characterized by a main peak in the same spectral region than CaP-S and CaP-BM, but here two additional bands attributed to the symmetric stretching v_1 (940–980 cm^{-1}) and the triple-degenerate asymmetric stretching v_3 (1000–1100 cm^{-1}) of β-TCP phosphate tetrahedron can be observed. Another difference consists in the band at 560 cm^{-1} that is typically attributed to the bending mode ($v_4(PO_4)^{3-}$) of β-TCP. Finally, it is worth noting the absence of bands ascribable to carbonate ions that instead can be observed in the spectra of CaP-S and CaP-BM. In this respect, the difference between CaP-FM and CaP-BM can be explained by the fact that during the thermal treatment, the mineral matrix in bone meal retains its HA structure, while in the case of fish bone half of the calcium deficient HA is converted into β-TCP which does not contain carbonate ions that are removed as CO_2 during the thermal treatment [38]. It can be concluded that the thermal treatment (850°C for 2h) was enough to induce the formation of β-TCP in fish bones, but not to completely remove carbonate ions from the HA of bone meal.

The chemical compositions of the samples are summarized in Table 26.

Table 26. Chemical composition of samples. Data are expressed as average wt.% of 3 replicates ± standard deviation

	CaP-BM	*CaP-FM*	*CaP-S*
Ca *(Average ± SD wt.%)*	33.92 ± 0.34	32.13 ± 0.77	32.49 ± 0.78
P *(Average ± SD wt.%)*	17.21 ± 0.26	17.63 ± 0.25	15.65 ± 0.38
Fe *(Average ± SD wt.%)*	0.02 ± 0.01	0.03 ± 0.01	0.04 ± 0.02
Mg *(Average ± SD wt.%)*	0.66 ± 0.02	0.65 ± 0.02	0.23 ± 0.01
Sr *(Average ± SD wt.%)*	0.02 ± 0.01	0.07 ± 0.01	/
Zn *(Average ± SD wt.%)*	0.02 ± 0.01	0.02 ± 0.01	/
Al *(Average ± SD wt.%)*	0.04 ± 0.01	0.08 ± 0.01	0.03 ± 0.01
Ca/P *(mol/mol)*	1.53	1.41	1.61

In addition to Ca and P, which are the two main elements of CaPs, materials content of Fe, Mg, Al, Sr and Zn is also reported as these elements are commonly present in biological HA [23]. The composition of CaP-S is typical of a carbonated and calcium deficient HA synthesized at room temperature, with a Ca/P molar ratio slightly smaller than stoichiometric HA (1.67) and a small portion of phosphate and/or hydroxide groups substituted by carbonates. On the other hand, CaP-S has the lowest contents of foreign elements - low Mg and Al amounts and no Sr and Zn. This is reasonable, as CaP-S was produced from a synthetic route using pure chemicals, which hence had a very low content of exogenous elements. The Ca/P ratios of the materials of natural

origin are much lower respect to CaP-S, with CaP-FM having the lowest Ca/P ratio. A simple explanation to this finding is that biological HAs are typically calcium deficient due to the occurrence of many bivalent cation in substitution to Ca^{2+} in their lattice [23]. Besides, CaP-FM has a much lower Ca/P ratio because it is a biphasic mixture of HA and β-TCP (Ca/P ratio of β-TCP is 1.5), differently from CaP-BM which consists of only HA.

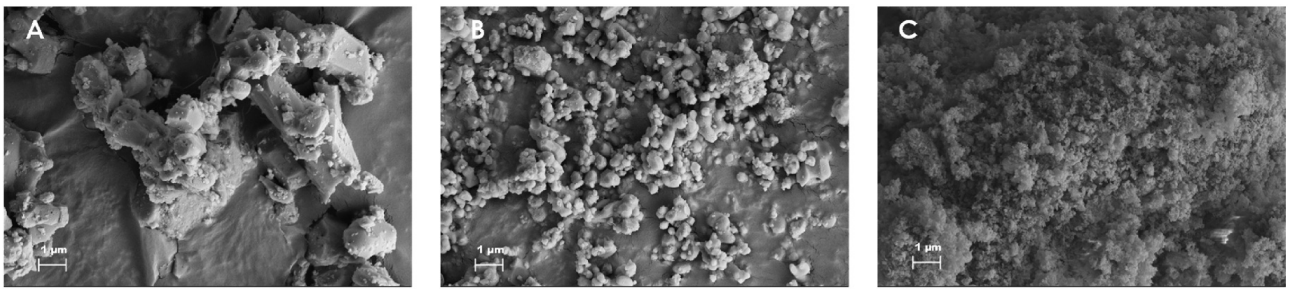

Figure 41. SEM micrographs of CaP-BM (A), CaP-FM (B) and CaP–S (C) at 25,000× of magnification

From the SEM pictures shown in Figure 41, it is possible to see that all the samples have peculiar characteristics. CaP-S consists of very small and nanometric particles, while CaP-FM and CaP-BM are made of much larger ones, the particles size order being CaP–S < CaP-FM < CaP-BM. CaP-S is made of needle-like nanoparticles with a major axis in the 90-150 nm range and a minor axis between 25 and 50 nm. CaP-FM particles are round shaped instead of needle-like and seems to have two populations of different size, the smaller being composed of particles with a diameter in the range between 100 and 200 nm, and the larger of particles with a diameter around 1 μm. This feature is typical for biphasic mixture of HA: β-TCP obtained from the thermal treatment of fish bones [14], made of both larger and multifaceted β-TCP particles and smaller and rounded HA particles [39]. Similarly to CaP-FM, also CaP-BM consisted of two populations of particles with different sizes, one made of round shaped particles around 100–200 nm (very similar to CaP-S), and the other made of more squared particles with defined facets and broad size distribution in the range between 1 and 5 μm. By combining the outputs from SEM and XRD analyses it can be said that for CaP-BM, larger particles consist of thermally annealed and crystalline HA, while

smaller ones consist of HA particles retaining their original features (e.g., nanometric dimensions and carbonation). This did not happen for the HA in fish bone, which could not endure the thermal treatment and was partially converted into β-TCP. This phenomenon can be ascribed to the different chemical composition of the two CaP sources, the mineral matrix of fish bone being more calcium deficient, i.e., with a Ca/P ratio much smaller with respect to that of bone meal.

The granulometry (Dv(0.9)), SSA, and the surface charge (ζ-potential) at pH 7.0 of the materials are reported in Table 27.

Table 27. Particles characteristics

	SSA (m^2/g)	**Dv(0.9) (µm)**	**ζ-potential (mV) at pH 7.0**
CaP-BM	3.9 ± 0.2	27.4	- 16.9 ± 0.4
CaP-FM	9.3 ± 0.5	8.7	- 4.0 ± 0.3
CaP-S	72.0 ± 3.6	4.9	- 20.0 ± 0.2

The Dv (0.9) of the three materials, i.e., the value of the size distribution below which the 90% of particles can be found, decreases in the order CaP-BM > CaP-FM > CaP-S, while the SSA follows exactly the opposite trend, with CaP-S > CaP-FM > CaP-BM. The Dv(0.9) and SSA values are in agreement between each other - as the specific surface area of a material is inversely proportional to the size of its particles - and with SEM pictures clearly showing that CaP-S is made of nanometric particles and CaP-FM and CaP-BM are made instead of micrometric ones. In fact, SSA values higher than 50 m^2/g are characteristic of nanometric HA, while values lower than 10 m^2/g are typical for thermal annealed CaPs. Finally, the surface charges of CaP-S and CaP-BM are similar, while that of CaP-FM is much lower. This difference is worthy to notice because electrostatic interaction has been largely recognized as one of the main mechanisms involved in the superficial adsorption of dyes on adsorbent phases [4].

5.3.2. Adsorption study of model textile dye

The adsorption kinetic curves of AB-185 on the three CaPs samples in water (pH 7.0) are shown in Figure 42. The amount of dye adsorbed increased rapidly over the first minutes of the experiment for all the materials, and reached the plateau after 5 min of contact. This means that for all the materials the adsorption was very fast.

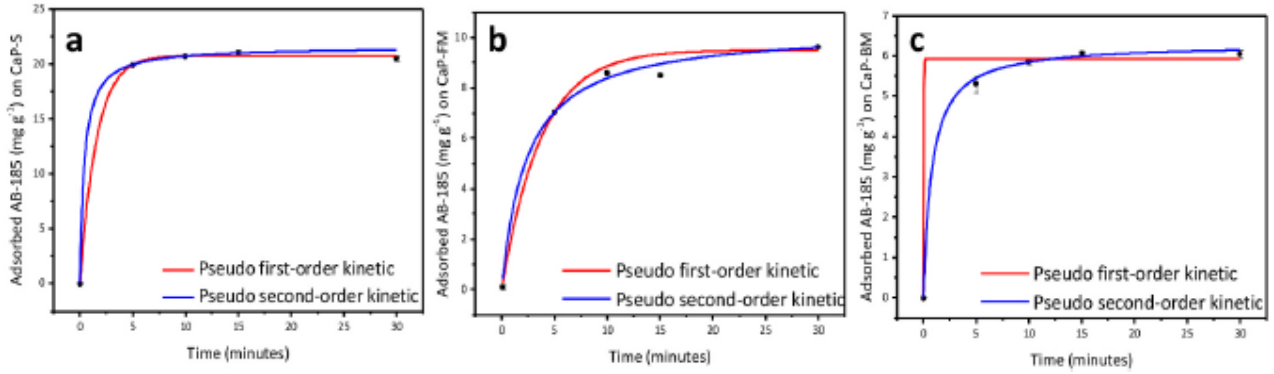

Figure 42. Adsorption kinetic data and fitting curves of AB-185 on (a) CaP–S, (b) CaP-FM and (c) CaP-BM. Black dots represent the experimental data (mean values and standard deviation for n = 3); lines represent the fitting curves of the pseudo first-order (red line) and of the pseudo second-order (blue line) fitting models

Kinetic data have been fitted with pseudo first-order and pseudo second-order fitting models, and the main fitting parameters are reported in Table 28.

Table 28. Fitting parameters of the kinetic adsorption curves

Kinetic model	Adjusted R^2	K_1/K_2 (min^{-1})	Q_e (mg/g)
CaP-BM			
Pseudo-first order	0.999	34.13 ± 0.01	5.93 ± 0.10
Pseudo-second order	0.999	1.27 ± 0.40	6.30 ± 0.12
CaP-FM			
Pseudo-first order	0.988	0.27 ± 0.01	9.50 ± 0.20
Pseudo-second order	0.995	0.42 ± 0.02	10.35 ± 0.16
CaP-S			
Pseudo-first order	1.000	44.43 ± 0.13	20.75 ± 0.011
Pseudo-second order	1.000	2.45 ± 0.34	21.56 ± 0.13

Generally speaking, all the kinetic data points are better fitted by the pseudo second-order curve, especially for data points in the range 0 - 10', as can be seen by the higher R^2 values. This would normally mean that chemisorption is the main rate-determining step and that the adsorption of dye molecules on CaP is mainly regulated by it [33]. However, the fitting parameters shows that both models can be used to describe AB-185/CaP systems. This is probably because dye adsorption is very quick and has already reached the plateau at the first time point, making difficult to discriminate if the main rate-determining step is controlled by chemisorption or physisorption [40]. The respective kinetic adsorption constant of CaP-S is higher respect to that of CaP-BM, which in turn is higher respect to that of CaP-FM, meaning that AB-185 adsorption speed on the three substrates followed the order CaP-S > CaP-BM > CaP-FM. However, the amounts of adsorbed dye at equilibrium were different, the Qe of CaP-S being the highest followed by CaP-FM and lastly by CaP-BM. These data are directly proportional to the SSA values of the three CaPs, as obviously adsorption is a surface process between the adsorbent phase and molecules in solution [41].

The adsorption kinetic curves were also measured in acidic and basic condition. These data points, together with the respective pseudo first and pseudo second order fitting

curves, are reported in the Supplementary Information (SI) in Figure S1 (a-c) and S2(a–c) for the experiments carried out namely at pH 5.5 and at pH 9.0, respectively. Data collected at acidic pH overlap with those recorded in neutral condition, while those collected at basic pH mainly differ in the amounts of dye adsorbed at equilibrium. More in details, these latter values are very similar among the three samples, and are much lower (i.e., around 2.0 mg/g) respect to those recorded in neutral and in acidic conditions. Changes in the adsorption capacities at different pH values are due to a combination of factors such as the characteristics of both the adsorbed molecule and the adsorbent phase. However, since here the adsorption capacity of CaPs samples shows the same decreasing trend at increasing pH values, and as anionic dyes like AB-185 have been proved to get poorly adsorbed at basic pH, it is reasonable to conclude that in this case the nature of the adsorbed molecule plays a primary role [42].

Isothermal adsorption curves at different pHs have been measured for all the samples. The isotherms recorded at neutral pH are reported in Figure 43, while those recorded in basic and acidic conditions are shown in Figure S3 (a-c) and S4 (a–c), respectively.

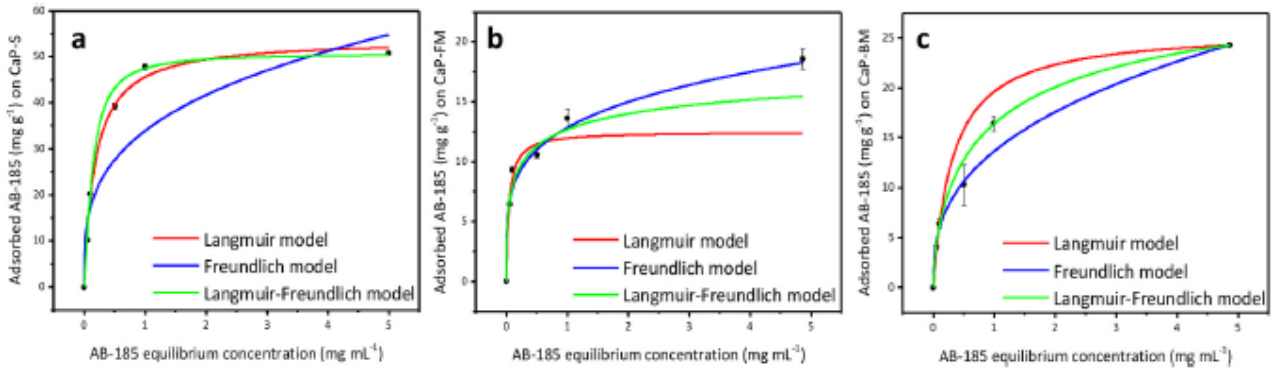

Figure 43. Isothermal adsorption data and relative fitting curves of AB-185 on (a) CaP–S, (b) CaP-FM and (c) CaP-BM. Black dots represent the experimental data (mean values and standard deviation for n = 3); lines represent the fitting curves obtained using Langmuir (red), Freundlich (blue) and hybrid (green) fitting models

Data points have been fitted with isothermal curves built using the Langmuir and Freundlich non-linear models, and using the Langmuir-Freundlich hybrid model. The main fitting parameters for all the CaPs studied are reported in Table 29.

Table 29. Main fitting parameters of isothermal adsorption curves following the Langmuir, Freundlich and the hybrid model for the three CaPs samples

Fitting model	Adjusted R^2	n	$K_{l,f,lf}$ (mL/mg)	Q_m (mg/g)
CaP-BM				
Langmuir	0.999	/	3.14 ± 0.57	25.85 ± 0.35
Freundlich	0.999	2.74 ± 0.17	13.63 ± 0.50	/
Langmuir-Freundlich	0.999	0.64 ± 0.66	0.94 ± 0.43	33.46 ± 3.61
CaP-FM				
Langmuir	0.991	/	21.59 ± 5.41	12.50 ± 1.22
Freundlich	0.995	4.48 ± 0.56	12.83 ± 0.89	/
Langmuir-Freundlich	0.994	0.43 ± 0.21	3.66 ± 1.54	20.00 ± 15.35
CaP-S				
Langmuir	0.996	/	5.48 ± 0.56	58.89 ± 2.77
Freundlich	0.959	3.35 ± 0.57	33.89 ± 3.74	/
Langmuir-Freundlich	0.999	1.35 ± 0.09	7.28 ± 0.43	50.74 ± 1.24

Although both Langmuir and Freundlich model gave good R^2 fitting values, CaP-S and CaP-FM data points were better fitted by the Langmuir-Freundlich hybrid model; this suggests a deviation from the standard Langmuir case, i.e., a situation where the interaction between adsorbed molecules is irrelevant. On the other hand, the three models used gave all good fits for CaP-BM, as denoted by the very high R^2 values.

The *n* exponent is one of the most important parameters in the hybrid model, as it carries information on the heterogeneity of the adsorbing phase surface, and on the cooperativity (positive or negative) between adsorbed molecules. In a few words, when the *n* value is lower than 1, the hybrid model suggests a negative cooperativity between adsorbed molecules, meaning that adsorbed molecules on the surface of the adsorbent phase prevent or hinder the adsorption of other molecules. On the other hand, *n* values

higher than 1 suggest the opposite (adsorbed molecules favors the adsorption of other molecules).

For CaP-S, the *n* value of the hybrid model is close to one, and points to a situation of no cooperativity – neither positive nor negative – between adsorbed molecules. The *n* parameter of the Freundlich model, on the other hand, indicates a heterogeneous surface ($n > 1$) and a high adsorption capacity of dye molecules ($Kf > 20$).

The situation for CaP-BM is similar, as the n value of the hybrid model is close to 1. However, in this case the adsorption capacity is lower with respect to CaP-S as indicated by the lower *qm* of both the Langmuir and the hybrid models, and by the lower *n* and *Kf* values of the Freundlich model. As mentioned above, the difference in SSA values between CaP-BM and CaP-S explains this difference in adsorption capability. Moreover, the lower *n* value of the Freundlich model suggests that CaP-BM surface is less heterogeneous than CaP-S.

For CaP-FM the situation is different and not so straightforward. Despite the low *qm* resulting from the Langmuir fitting, the *Kl* value was by far the highest among those measured, suggesting a very strong interaction between the adsorbent and the adsorbed molecules but a scarce availability of binding sites. On the other hand, the *Kf* value of the Freundlich model is the lowest among those measured (but still falling in a range favourable for adsorption [43]) while the *n* value is the highest, denoting a much higher heterogeneity of the material compared to the others. Overall, the isothermal adsorption data points of CaP-FM were better fitted by the hybrid model, with a very low *Klf*, a *n* value lower than 1 and the lowest *qm* value. This is probably due to the fact that, as showed by XRD and FT-IR analyses CaP-FM is a biphasic material with a much higher heterogeneity compared to CaP-S and CaP-BM which are composed only of HA. In fact, one of the main assumptions of the Langmuir model is that all the adsorption sites are identical, and hence that the materials surface is rather homogenous. Being a mixture of HA and β-TCP, the adsorption behaviour of CaP-FM is better fitted by the Langmuir-Freundlich hybrid empirical model which is more suited to describe

materials having a heterogenous surface with a non-uniform distribution of adsorption sites. However, the *qm* value obtained for CaP-FM by using this model is small and characterized by a very high standard deviation, denoting once again the varied nature of the material and the non-linearity of the adsorption. In this case the *qm* value lower than that of CaP-BM is not merely ascribable to the SSA being it larger, but rather to the lower net surface charge with respect to the other CaP samples. Finally, a sketch highlighting the relation between SSA and net surface charge with the adsorption capacities of the different materials is reported in Figure 44.

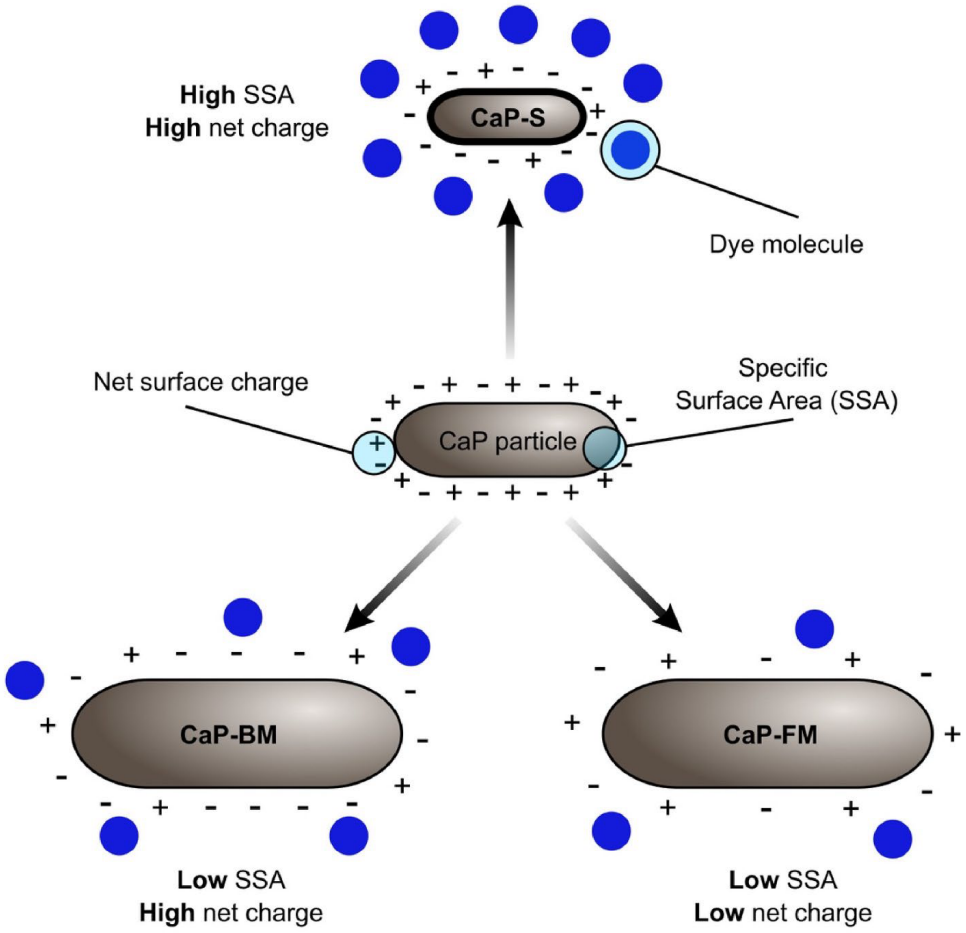

Figure 44. Interaction between CaPs and AB-185 molecules. Higher net surface charges and SSAs of the materials correspond to higher adsorption capacities

A comparative table reporting the maximum adsorption capacity of different types of acid blue dyes for different kinds of adsorbent phases is reported in Table S2 of the SI. Among inorganic materials, bentonite has indeed the highest adsorption capacity

(740.5 mg/g), but for a different dye molecule from that used in the present study. The adsorption capacity reported for alunite is also higher than CaPs (212.8 mg/g), even though its value is lower than zeolite gave by far the highest adsorption value (1176.3 mg/g), but as in the case of zeolite a different dye was employed. Generally speaking, a direct comparison between the results obtained in the present study and those reported in the literature cannot be made for two reasons. First, only one work on the removal of AB-185 from water solution employing synthetic zeolite as adsorbent has been reported so far, reporting a maximum adsorption value of 84.5 mg/g similar to that of CaP-S [44]. Second, the majority of the works reporting the removal of textile dyes by CaPs adsorption employ synthetic HA nanocomposites [45 - 47]. Unfortunately, many works report on the use of natural CaPs deriving from animal bones for the immobilization of heavy metals from wastewaters [19, 48] but not for textile dyes' adsorption.

AB-185 adsorption capacities reported in the present work for both natural and synthetic CaPs are lower than those reported for the adsorption of other acid dyes by CaPs in the literature. This discrepancy is due in the first place to the different experimental conditions employed, and especially to the various initial dye concentrations that are much higher than the one employed in this study (5.0 mg/L vs. 20.0 - 500.0 mg/L). This has been proved to play a major role in the adsorption, as higher dye concentrations mean higher interaction between molecules and adsorbent phase [49]; moreover, high concentrations of acid dyes determine changes in the pH values, and the adsorption capacity of CaPs can be seriously affected by the pH of the solution as can be seen in the SI in Table S1. Secondly, all these studies recognized that a major role in the adsorption of dyes is played by the binding capacity of the carbon-based fraction of CaPs composites, as also proved by a recent work employing alkaline treated tea waste as sorbent for the removal of toxic pollutants [50].

Finally, it can be concluded that all the materials investigated in this work can be employed for the removal of AB-185 dye from wastewaters of the textile industry, and

that their efficiency may vary depending on a series of factors, such as CaPs source (i.e., synthetic, from bone meal and from fish meal), dye concentration, and wastewater pH. In the case of materials extracted from bones by-products, the thermal treatment to which bones are subjected to extract the CaPs affected their performances in terms of dye removal due to the concomitant reduction of the SSA and – in the case of CaPs from fish bones – to the lower net surface charge respect to synthetic HA.

5.4. Conclusions

Synthetic CaPs and CaPs thermally extracted from fish bones and bone meal have been characterized from the physical-chemical point of view, and their application for textile wastewaters treatment as adsorbent phases of a model blue dye (AB-185) has been investigated.

The synthetic CaP (CaP-S) was composed of nanometric HA particles with relatively high specific surface area (SSA) and net surface charge. CaPs from bone meal (CaP-BM) consisted of single-phase HA, the main differences with CaP-S being the lower Ca/P ratio, the larger particle size and the much smaller SSA. On the other hand, the sample from fish bones (CaP-FM) was very different with respect to CaP-S and consisted of a biphasic mixture of HA and β-TCP with similar SSA values and particles size with respect to CaP-BM, but much lower Ca/P molar ratio and net surface charge. A relation between these physical-chemical parameters and the adsorption capacity of CaPs was found. The kinetic adsorption study showed that the adsorption of AB-185 was favoured and very fast for all the materials, making difficult to identify the nature of the main adsorption mechanism (chemisorption vs physisorption). The isothermal adsorption study showed that CaP-S had the highest adsorption capacity, followed by CaP-BM and lastly by CaP-FM. SSA was found to be the main parameter determining samples adsorption ability. However, the data suggested that an important role is played by the net surface charge of the particles, as CaP-FM had a higher SSA but a much smaller net surface charge compared to CaP-BM, limiting the electrostatic interaction between dyes molecules and the materials surface. Was also found that physico-chemical parameters determining the performances of CaPs as adsorbent phase for textile wastewaters remediation, especially SSA and net surface charge, are seriously affected by both production process (synthetic vs. thermal extraction from bones) and in the case of CaPs from food-industry by-products, from the source (i.e., bone meal and fish bones).

The three CaPs here reported can be employed for the removal of AB- 185 dye from wastewaters of the textile industry, with dyes removal efficiency differing between synthetic CaP and CaPs extracted from bones. In this respect, it is important to note that the thermal treatment of bones can impair the performance of the final materials as the high temperatures required by the process determine low SSA values and net surface charge posing serious limitations on bones incineration for the extraction of CaPs to be used as adsorbent phases in wastewater treatment. Thus, in view of their final application, variables of CaPs production process must be considered carefully, especially when recovering CaPs from circular economy sources for which other techniques than bones incineration (e.g., CaPs dissolution and reprecipitation) could be more appropriate.

Supplementary Information

Natural calcium phosphates from circular economy as adsorbent phases for the remediation of textile industry wastewaters

Giuseppe Falini[1]. Maria Luisa Basile[1]. Sara Gandolfi[2,3]. Francesca Carella[2]. Guia Guarini[2]. Lorenzo Degli Esposti[2]. Michele Iafisco[2] & Alessio Adamiano[2]*.*

[1] Dipartimento di Chimica Giacomo Ciamician Università di Bologna. Via Selmi. 2. 40126 Bologna. Italy.

[2] Institute of Science and Technology for Ceramics (ISTEC). National Research Council (CNR). Via Granarolo 64. 48018 Faenza. Italy.

[3] Dipartimento di Scienze Chimiche. della Vita e della Sostenibilità Ambientale. Parco Area delle Scienze 17/A. 43124 Parma. Italy.

*Corresponding authors: alessio.adamiano@istec.cnr.it. michele.iafisco@istec.cnr.it

Keywords

Calcium phosphate; Circular economy; Bone waste; Water remediation; Textile dyes; Adsorption

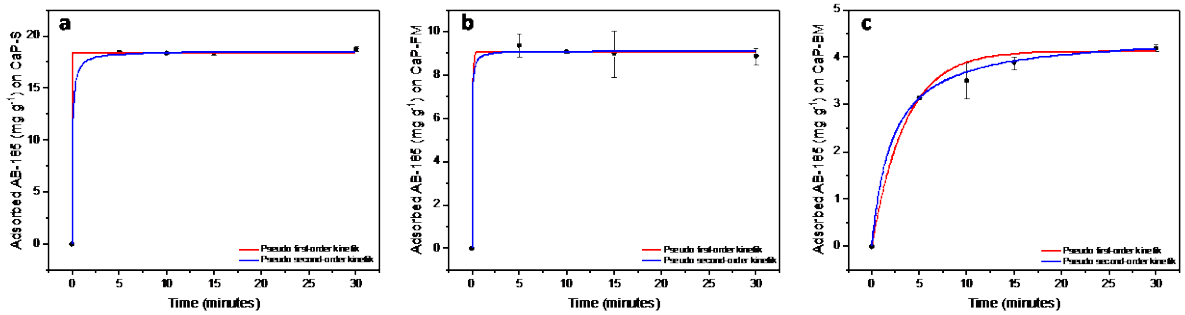

Figure S1. Adsorption kinetic data at pH 5.5 and fitting curves of AB-185 on (a) CaP-S. (b) CaP-FM and (c) CaP-BM. Black dots represent the experimental data (mean values and standard deviation for n=3); lines represent the fitting curves of the pseudo first-order (red line) and of the pseudo second-order (blue line) fitting models

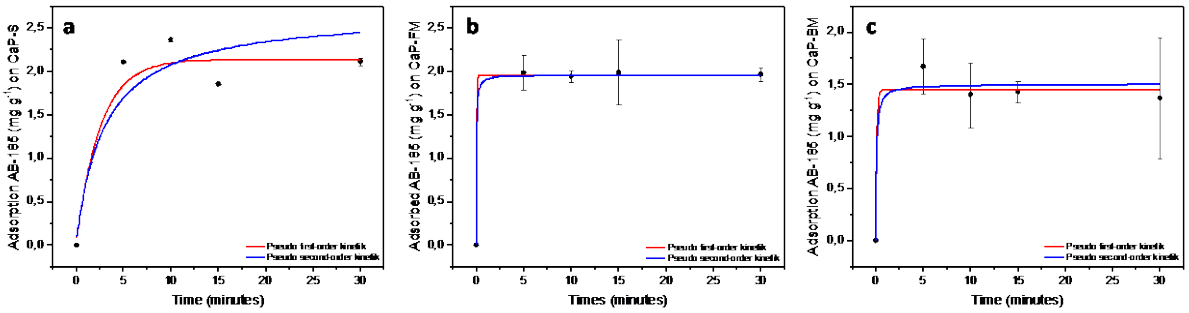

Figure S2. Adsorption kinetic data at pH 9.0 and fitting curves of AB-185 on (a) CaP-S. (b) CaP-FM and (c) CaP-BM. Black dots represent the experimental data (mean values and standard deviation for n=3); lines represent the fitting curves of the pseudo first-order (red line) and of the pseudo second-order (blue line) fitting models

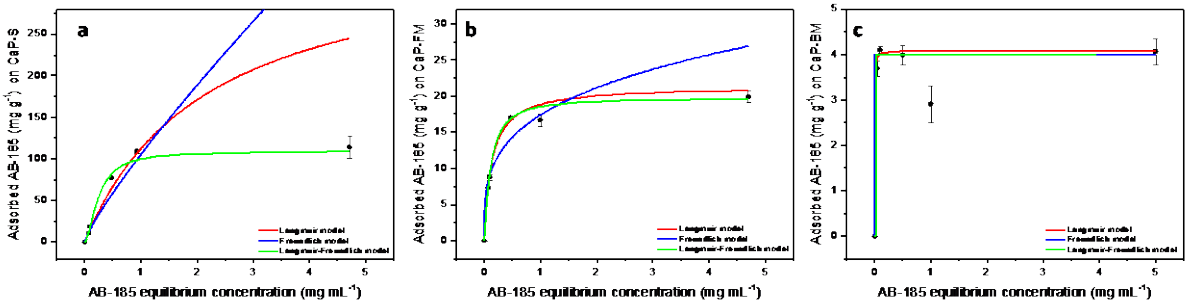

Figure S3. Isothermal adsorption data at pH 5.5 and relative fitting curves of AB-185 on (a) CaP-S. (b) CaP-FM and (c) CaP-BM. Black dots represent the experimental data (mean values and standard deviation for n=3); lines represent the fitting curves obtained using Langmuir (red). Freundlich (blue) and hybrid (green) fitting models

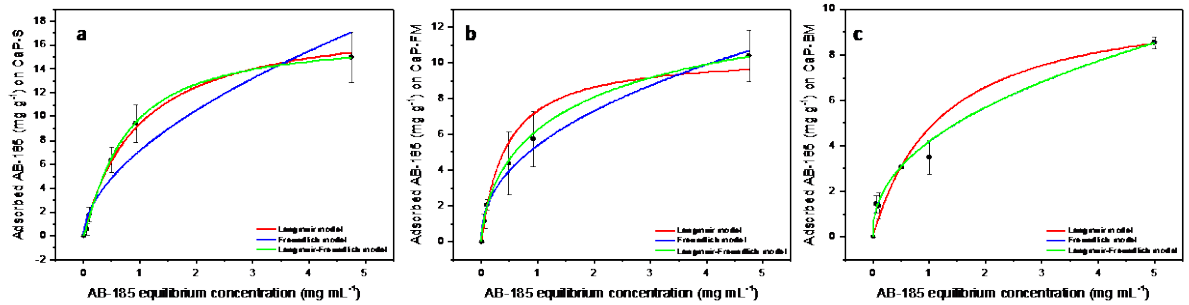

Figure S4. Isothermal adsorption data and relative fitting curves at pH 9.0 of AB-185 on (a) CaP-S. (b) CaP-FM and (c) CaP-BM. Black dots represent the experimental data (mean values and standard deviation for n=3); lines represent the fitting curves obtained using Langmuir (red). Freundlich (blue) and hybrid (green) fitting models

Table S1. Main fitting parameters of the isothermal adsorption curves following the Langmuir, Freundlich and the hybrid model for the three CaPs samples at acidic and basic pH

Fitting model	Adjusted R^2	n	$K_{(l,f,lf)}$ (mL/mg)	Q_m (mg/g)
CaP-S ***pH 5.5***				
Langmuir	0.989	/	0.45 ± 0.26	359.93 ± 215.18
Freundlich	0.975	1.18 ± 0.14	105.03 ± 25.59	/
Langmuir - Freundlich	0.999	1.73 ± 0.18	3.91 ± 0.77	109.26 ± 12.66
CaP-BM ***pH 5.5***				
Langmuir	0.997	/	481.70 ± 1333.76	4.09 ± 0.25
Freundlich	0.997	4.50 ± 0.11	4.00 ± 0.11	/
Langmuir - Freundlich	0.948	140.81 ± 0.01	38.27 ± 0.10	4.00 ± 0.54
CaP-FM ***pH 5.5***				
Langmuir	0.999	/	7.39 ± 0.58	21.38 ± 0.70
Freundlich	0.970	3.54 ± 0.78	17.37 ± 1.99	/
Langmuir - Freundlich	0.999	1.21 ± 0.20	8.97 ± 1.36	19.82 ± 1.25
CaP-S ***pH 9.0***				
Langmuir	0.986	/	1.03 ± 0.23	18.50 ± 2.19
Freundlich	0.923	1.79 ± 0.30	7.15 ± 1.04	/
Langmuir - Freundlich	0.990	1.16 ± 0.16	1.39 ± 0.42	16.62 ± 2.29
CaP-BM ***pH 9.0***				
Langmuir	0.996	/	0.82 ± 0.10	10.58 ± 0.73
Freundlich	0.999	2.27 ± 0.07	4.19 ± 0.06	/
Langmuir - Freundlich	0.999	0.44 ± 0.19	$3.4*10^{-6}$ ± $7.6*10^{-4}$	1115.59 ± 96613.26

CaP-FM ***pH 9.0***				
Langmuir	0.980	/	2.30 ± 0.50	10.51 ± 1.27
Freundlich	0.985	2.28 ± 0.17	5.39 ± 0.33	/
Langmuir - Freundlich	0.990	0.65 ± 0.19	0.47 ± 0.84	16.41 ± 8.57

Table S2. Maximum adsorption capacity of acid blue dyes for different classes of adsorbent phases

Adsorbent phase	**Dye**	**q_m (mg/g)**	**References**
Zeolite	Acid blue 185	84.5	[44]
Bentonite	Acid blue 193	740.5	[51]
Alunite	Acid blue 40	212.8	[52]
Clay	Acid blue 9	64.7	[53]
Silica	Acid blue 25	45.8	[54]
Commercial activated carbons	Acid blue 80	112.3	[55]
	Acid blue 40	133.3	[52]
Coal-based sorbents from solid wastes	Acid blue 264	1176.0	[56]
	Acid blue 25	673.0	[57]
	Acid blue 113	219.0	[58]
Peat	Acid blue 25	12.7	[59]
Cotton, chitosan and starch-based materials	Acid blue 25	589.0-77.4	[60]-[61]
Waste materials from agriculture and industry	Acid blue 256	280.3	[62]
	Acid blue 25	17.5	[63]

References

[1] M.T. Uddin, M.A. Islam, S. Mahmud, M. Rukanuzzaman, Adsorptive removal of methylene blue by tea waste, J. Hazard Mater. 164 (2009) 53–60. [2] C. O'Neill, F.R. Hawkes, D.L. Hawkes, N.D. Lourenço, H.M. Pinheiro, W. Del´ee, Colour in textile effluents–sources, measurement, discharge consents and simulation: a review, J. Chem. Technol. Biotechnol. 74 (1999) 1009–1018.

[2] C. O'Neill, F.R. Hawkes, D.L. Hawkes, N.D. Lourenço, H.M. Pinheiro, W. Del´ee, Colour in textile effluents–sources, measurement, discharge consents and simulation: a review, J. Chem. Technol. Biotechnol. 74 (1999) 1009–1018.

[3] I.M. Banat, P. Nigam, D. Singh, R. Marchant, Microbial decolorization of textile-dyecontaining effluents: a review, Bioresour. Technol. 58 (1996) 217–227.

[4] S. Pai, M.S. Kini, R. Selvaraj, A review on adsorptive removal of dyes from wastewater by hydroxyapatite nanocomposites, Environ. Sci. Pollut. Res. 28 (2021) 11835–11849.

[5] B. Lellis, C.Z. F´avaro-Polonio, J.A. Pamphile, J.C. Polonio, Effects of textile dyes on health and the environment and bioremediation potential of living organisms, Biotechnol. Res. Innov. 3 (2019) 275–290.

[6] J. Xu, F. Wang, W. Liu, W. Cao, Nanocrystalline N-doped powders: mild hydrothermal synthesis and photocatalytic degradation of phenol under visible light irradiation, Int. J. Photoenergy (2013) 2013.

[7] A. Jain, V. Gupta, A. Bhatnagar, Suhas, A comparative study of adsorbents prepared from industrial wastes for removal of dyes, Separ. Sci. Technol. 38 (2003) 463–481.

[8] K. Saltalı, A. Sarı, M. Aydın, Removal of ammonium ion from aqueous solution by natural Turkish (Yıldızeli) zeolite for environmental quality, J. Hazard Mater. 141 (2007) 258–263.

[9] J. Ye, D. Nyobe, B. Tang, L. Bin, P. Li, S. Huang, F. Fu, Y. Cai, G. Guan, X. Hao, Facilely synthesized recyclable mesoporous magnetic silica composite for highly efficient and fast adsorption of methylene blue from wastewater: thermodynamic mechanism and kinetics study, J. Mol. Liq. 303 (2020), 112656.

[10] T. Arfin, N. Varshney, B. Singh, Ionic Liquid Modified Activated Carbon for the Treatment of Textile Wastewater, Green Materials for Wastewater Treatment, Springer, 2020, pp. 257–275.

[11] W. Lemlikchi, N. Drouiche, N. Belaicha, N. Oubagha, B. Baaziz, M. Mecherri, Kinetic study of the adsorption of textile dyes on synthetic hydroxyapatite in aqueous solution, J. Ind. Eng. Chem. 32 (2015) 233–237.

[12] H.Y. Yoon, J.G. Lee, L.D. Esposti, M. Iafisco, P.J. Kim, S.G. Shin, J.-R. Jeon, A. Adamiano, Synergistic release of crop nutrients and stimulants from hydroxyapatite nanoparticles functionalized with humic substances: toward a multifunctional nanofertilizer, ACS Omega 5 (2020) 6598–6610.

[13] A. Nzihou, P. Sharrock, Role of phosphate in the remediation and reuse of heavy metal polluted wastes and sites, Waste Biomass Valori 1 (2010) 163–174.

[14] C. Piccirillo, C.W. Dunnill, R.C. Pullar, D.M. Tobaldi, J.A. Labrincha, I.P. Parkin, M. M. Pintado, P.M. Castro, Calcium phosphate-based materials of natural origin showing photocatalytic activity, J. Mater. Chem. A. 1 (2013) 6452–6461.

[15] A. Hu, M. Li, C. Chang, D. Mao, Preparation and characterization of a titanium-substituted hydroxyapatite photocatalyst, J. Mol. Catal. Chem. 267 (2007) 79–85.

[16] N. Hoda, E. Bayram, E. Ayranci, Kinetic and equilibrium studies on the removal of acid dyes from aqueous solutions by adsorption onto activated carbon cloth, J. Hazard Mater. 137 (2006) 344–351.

[17] M.R. Lee, G.W. Lee, J.E. Kim, W.B. Yun, J.Y. Choi, J.J. Park, H.R. Kim, B.R. Song, J. W. Park, M.J. Kang, Biocompatibility of a PLA-based composite

containing hydroxyapatite derived from waste bones of dolphin Neophocaena asiaeorientalis, J. Australas. Ceram. Soc. 55 (2019) 269–279.

[18] K. Varaprasad, D. Nunez, M.M. Yallapu, T. Jayaramudu, E. Elgueta, P. Oyarzun, Nano-hydroxyapatite polymeric hydrogels for dye removal, RSC Adv. 8 (2018) 18118–18127.

[19] E.A.B. da Silva, C.A. Costa, V.J. Vilar, C. Botelho, M.B. Larosi, J.M. Saracho, R. A. Boaventura, Water remediation using calcium phosphate derived from marine residues, Water, Air, Soil Pollut. 223 (2012) 989–1003.

[20] H. Hossini, R. Darvishi Cheshmeh Soltani, M. Safari, A. Maleki, R. Rezaee, R. Ghanbari, The application of a natural chitosan/bone char composite in adsorbing textile dyes from water, Chem. Eng. Commun. 204 (2017) 1082–1093.

[21] Y. Miyah, M. Benjelloun, R. Salim, L. Nahali, F. Mejbar, A. Lahrichi, S. Iaich, F. Zerrouq, Experimental and DFT theoretical study for understanding the adsorption mechanism of toxic dye onto innovative material Fb-HAp based on fishbone powder, J. Mol. Liq. (2022), 119739.

[22] Z. Kowalski, M. Banach, A. Makara, Optimisation of the co-combustion of meat–bone meal and sewage sludge in terms of the quality produced ashes used as substitute of phosphorites, Environ. Sci. Pollut. Res. 28 (2021) 8205–8214.

[23] V. Ferraro, A.P. Carvalho, C. Piccirillo, M.M. Santos, P.M. Castro, M.E. Pintado, Extraction of high added value biological compounds from sardine, sardine-type fish and mackerel canning residues—a review, Mater. Sci. Eng. C 33 (2013) 3111–3120.

[24] A. Saeid, M. Labuda, K. Chojnacka, H. G´orecki, Valorization of bones to liquid phosphorus fertilizer by microbial solubilization, Waste Biomass Valori 5 (2014) 265–272.

[25] M. Coutand, M. Cyr, E. Deydier, R. Guilet, P. Clastres, Characteristics of industrial and laboratory meat and bone meal ashes and their potential applications, J. Hazard Mater. 150 (2008) 522–532.

[26] M. Islam, M. Mostafa, Textile dyeing effluents and environment concerns-a review, J. Environ. Sci. Nat. Res. 11 (2018) 131–144.

[27] A.S. ¨Ozcan, B. Erdem, A. ¨Ozcan, Adsorption of acid blue 193 from aqueous solutions onto BTMA-bentonite, Colloid. Surface. 266 (2005) 73–81.

[28] A. ¨Ozcan, E.M. ¨Oncü, A.S. ¨Ozcan, Kinetics, isotherm and thermodynamic studies of adsorption of Acid Blue 193 from aqueous solutions onto natural sepiolite, Colloid. Surface. 277 (2006) 90–97.

[29] D. Uzuno˘glu, A. ¨Ozer, Adsorption of Acid Blue 121 dye on fish (Dicentrarchus labrax) scales, the extracted from fish scales and commercial hydroxyapatite: equilibrium, kinetic, thermodynamic, and characterization studies, Desalination Water Treat. 57 (2016) 14109–14131.

[30] F. Carella, M. Seck, L. Degli Esposti, H. Diadiou, A. Maienza, S. Baronti, P. Vignaroli, F.P. Vaccari, M. Iafisco, A. Adamiano, Thermal conversion of fish bones into fertilizers and biostimulants for plant growth–A low tech valorization process for the development of circular economy in least developed countries, J. Environ. Chem. Eng. 9 (2021), 104815.

[31] A. Adamiano, N. Sangiorgi, S. Sprio, A. Ruffini, M. Sandri, A. Sanson, P. Gras, D. Grossin, C. Franc`es, K. Chatzipanagis, Biomineralization of a titanium-modified hydroxyapatite semiconductor on conductive wool fibers, J. Mater. Chem. B 5 (2017) 7608–7621.

[32] A. Adamiano, D. Fabbri, G. Falini, M.G. Belcastro, A complementary approach using analytical pyrolysis to evaluate collagen degradation and mineral fossilisation in archaeological bones: the case study of Vicenne-Campochiaro necropolis (Italy), J. Anal. Appl. Pyrol. 100 (2013) 173–180.

[33] M. Iafisco, F. Carella, L. Degli Esposti, A. Adamiano, D. Catalucci, J. Modica, A. Bragonzi, A. Vitali, R. Torelli, M. Sanguinetti, Biocompatible antimicrobial colistin loaded calcium phosphate nanoparticles for the counteraction of biofilm formation in cystic fibrosis related infections, J. Inorg. Biochem. 230 (2022), 111751.

[34] J. Lin, L. Wang, Comparison between linear and non-linear forms of pseudo-first-order and pseudo-second-order adsorption kinetic models for the removal of methylene blue by activated carbon, Front. Environ. Sci. Eng. 3 (2009) 320–324.

[35] H.-K. Chung, W.-H. Kim, J. Park, J. Cho, T.-Y. Jeong, P.-K. Park, Application of Langmuir and Freundlich isotherms to predict adsorbate removal efficiency or required amount of adsorbent, J. Ind. Eng. Chem. 28 (2015) 241–246.

[36] B. Fowler, E. Moreno, W. Brown, Infra-red spectra of hydroxyapatite, octacalcium phosphate and pyrolysed octacalcium phosphate, Arch. Oral Biol. 11 (1966) 477–492.

[37] M. Iafisco, A. Ruffini, A. Adamiano, S. Sprio, A. Tampieri, Biomimetic magnesium–carbonate-apatite nanocrystals endowed with strontium ions as anti-osteoporotic trigger, Mater. Sci. Eng. C 35 (2014) 212–219.

[38] C. Piccirillo, A. Adamiano, D.M. Tobaldi, M. Montalti, J. Manzi, P.M.L. Castro, S. Panseri, M. Montesi, S. Sprio, A. Tampieri, Luminescent calcium phosphate bioceramics doped with europium derived from fish industry byproducts, J. Am. Ceram. Soc. 100 (2017) 3402–3414.

[39] A. Adamiano, G. Fellet, M. Vuerich, D. Scarpin, F. Carella, C. Piccirillo, J.-R. Jeon, A. Pizzutti, L. Marchiol, M. Iafisco, Calcium phosphate particles coated with humic substances: a potential plant biostimulant from circular economy, Molecules 26 (2021) 2810.

[40] K. Rasoulpoor, A.P. Marjani, E. Nozad, Competitive chemisorption and physisorption processes of a walnut shell based semi-IPN bio-composite

adsorbent for lead ion removal from water: equilibrium, Kinetic and Thermodynamic studies, Environ. Technol. Innovat. 20 (2020), 101133.

[41] A.I. Adeogun, E.A. Ofudje, M.A. Idowu, S.O. Kareem, S. Vahidhabanu, B.R. Babu, Biowaste-derived hydroxyapatite for effective removal of reactive yellow 4 dye: equilibrium, kinetic, and thermodynamic studies, ACS Omega 3 (2018) 1991–2000.

[42] M.A. Islam, I. Ali, S.A. Karim, M.S.H. Firoz, A.-N. Chowdhury, D.W. Morton, M. J. Angove, Removal of dye from polluted water using novel nano manganese oxide-based materials, J. Water Proc. Eng. 32 (2019), 100911.

[43] F. Batool, J. Akbar, S. Iqbal, S. Noreen, S.N.A. Bukhari, Study of isothermal, kinetic, and thermodynamic parameters for adsorption of cadmium: an overview of linear and nonlinear approach and error analysis, Bioinorgan. Chem. Appl. 2018 (2018).

[44] S. Kulawong, N. Chanlek, N. Osakoo, Facile synthesis of hierarchical structure of NaY zeolite using silica from cogon grass for acid blue 185 removal from water, J. Environ. Chem. Eng. 8 (2020), 104114.

[45] H. Hou, R. Zhou, P. Wu, L. Wu, Removal of Congo red dye from aqueous solution with hydroxyapatite/chitosan composite, Chem. Eng. J. 211 (2012) 336–342.

[46] D.C. Manatunga, R.M. de Silva, K.N. De Silva, R. Ratnaweera, Natural polysaccharides leading to super adsorbent hydroxyapatite nanoparticles for the removal of heavy metals and dyes from aqueous solutions, RSC Adv. 6 (2016) 105618–105630.

[47] S. Ghanavati Nasab, A. Semnani, A. Teimouri, H. Kahkesh, T. Momeni Isfahani, S. Habibollahi, Removal of Congo red from aqueous solution by hydroxyapatite nanoparticles loaded on zein as an efficient and green adsorbent: response surface methodology and artificial neural network-genetic algorithm, J. Polym. Environ. 26 (2018) 3677–3697.

[48] E. Deydier, R. Guilet, S. Cren, V. Pereas, F. Mouchet, L. Gauthier, Evaluation of meat and bone meal combustion residue as lead immobilizing material for in situ remediation of polluted aqueous solutions and soils: “Chemical and ecotoxicological studies”, J. Hazard Mater. 146 (2007) 227–236.

[49] S. Chaudhary, P. Sharma, R. Kumar, Hydroxyapatite doped CeO2 nanoparticles: impact on biocompatibility and dye adsorption properties, RSC Adv. 6 (2016) 62797–62809.

[50] M.M. Kabir, S.S.P. Mouna, S. Akter, S. Khandaker, M. Didar-ul-Alam, N. M. Bahadur, M. Mohinuzzaman, M.A. Islam, M. Shenashen, Tea waste based natural adsorbent for toxic pollutant removal from waste samples, J. Mol. Liq. 322 (2021), 115012.cc

CONCLUSIONS

The extraction of calcium phosphate (*CaP*) and collagen (*Col*) from salmon (*Salmo salar*) bones was conducted through three distinct extraction methods in a circular economy perspective: using an ionic liquid (BMIM) and a deep eutectic solvent (DES), by alkaline hydrolysis, and by enzymatic extraction.

Extraction using *BMIM/DES* was carried out at different times (2.5h, 5h, and 24h), but in all cases, it proved unsatisfactory in terms of extraction yields and product selectivity. One of the key advantages of these extraction solvents is their potential for reuse, as they can be recovered from the extraction process. However, in this case, their recovery was ineffective, preventing the reuse of the extractants and resulting in impure products. These findings limit the feasibility of applying these methods on an industrial scale, indicating the need for further research and optimization.

In contrast, *alkaline hydrolysis* produced more satisfactory results, particularly regarding CaP yield. Samples were extracted for 4 or 24h at 30 or 60°C, with some pretreated using ultrasound for 1h. Although it was not possible to identify a general trend regarding the influence of extraction parameters on the extraction yields, variations were observed, with pretreatment and 4h extraction at 60°C providing the best results compared to other operating conditions. On the other hand, the organic extracts were found to be very rich in native Col for all extracted samples, regardless of the extraction conditions.

A three-factorial Design of Experiment approach with two levels each (*DoE 3x2*) was employed to identify the best extraction parameters in terms of both organic and inorganic purity, as well as of Col estimated amount in the organic extract. The DOE indicated that these three outputs can be maximized by carrying out an extraction with the following parameters: fishbone sample pretreatment with ultrasound for 1h, followed by a 4h extraction at 45°C.

Characterisation of the CaP obtained by calcination of the extraction residues revealed the occurrence of a biphasic mixture composed of β-TCP and HA. The results showed that the physico-chemical properties of the CaP obtained were not influenced by variations in the extraction process parameters; moreover, the CaP from the simultaneous extractions of Col and CaP - that was obtained by calcination of the extraction residue - were never significantly different with respect to the CaP derived from the calcination of untreated fishbone.

To improve the organic yields, extractions were conducted using three different *enzymes*, trypsin, papain and pepsin, each exhibiting maximum enzyme activity at a distinct pH value of 5.6, 7.0 and 8.2, respectively. Among the three enzymes, trypsin was the one that gave the best results in terms of yields, in particular the organic yield was almost three times that of the control (i.e., using the same extraction conditions without the enzyme).

As the next step, this study explored the use of the CaP extracted from fish bones, in sun and oral care, and as an adsorbent phase for the removal of dye pollutants from wastewater generated by the textile industry.

In the context of *sun care* applications, CaP at different concentrations (4 wt.% and 9 wt.%) proved to be an effective booster in sunscreen formulations containing two different organic UV filters at different concentrations, octocrylene (OCR 10 wt.% and 20 wt.%) and avobenzone (BMDBM 5 wt.%), as well as in sunscreens containing an inorganic filter (ZnO 20 wt.%). In all cases, synergy was observed between CaP and the UV filters, increasing the sun protection factor (SPF) of the cream, showing that equally effective protection against UV-ray can be obtained for sunscreens having lower UV-filters concentrations.

In *oral care*, CaP has proven to be an effective remineralising agent for dental enamel. Due to its high solubility, β-TCP allowed for a faster release of phosphate and carbonate ions that, by depositing on the damaged surface, are able to induce the natural regeneration of enamel. In addition to this, it was also able to prevent dentinal

sensitivity. Thanks to its micrometric size, the CaP obtained from salmon bones was able to penetrate inside the dentinal tubules and plug them, creating a physical barrier that prevents hot/cold substances from reaching the nerves contained in the tooth root.

Last but not least, this study investigated the possibility of using synthetic calcium phosphate (CaP-S) and natural CaPs thermally extracted from salmon bones (CaP-FM) and bovine bones (CaP-BM) as adsorbent phases for the removal of a copper anionic dye, tri-sulphonic phthalocyanine acid - also known as acid blue 185 (AB-185), one of the most widely used dyes worldwide.

The three types of CaPs investigated in this study were found to be suitable for the removal of AB-185 dye from textile industry *wastewaters*, with variations in efficiency observed between synthetic CaP and bone-derived CaPs. It is noteworthy that thermal processing of bones can adversely affect the properties of the resulting materials. Specifically, the high temperatures involved lead to reduced SSA and net surface charge, which pose significant challenges for utilizing bone incineration as a method to extract CaPs for use as adsorbents in wastewater treatment. Consequently, the production process of CaPs must be optimized with the intended application in mind, particularly when sourcing CaPs from circular economy materials. Alternative methods, such as dissolution and reprecipitation, may offer more suitable approaches than incineration in these cases.

In conclusion, this study highlights the potential of extracting valuable materials such as CaP and Col from food by products – in this case salmon bones – aligning with the principles of the circular economy and sustainable development. The findings emphasize the importance of optimizing extraction methods to achieve natural materials with high yields and purities, thus promoting the valorisation of biogenic waste. Such advancements not only reduce environmental impact but also provide sustainable alternatives for industrial applications, including cosmetics, oral care, and wastewater treatment, contributing to a more resource-efficient and environmentally friendly future.

La borsa di dottorato è stata cofinanziata con risorse del
Programma Operativo Nazionale Ricerca e Innovazione 2014-2020, risorse FSE REACT-EU
Azione IV.4 “Dottorati e contratti di ricerca su tematiche dell’innovazione”
e Azione IV.5 “Dottorati su tematiche Green”